NUREG/CR-0442
ANL-CT-78-41

EFFECTS OF AIR BLAST ON POWER PLANT STRUCTURES AND COMPONENTS

by

C. A. Kot, R. A. Valentin, D. A. McLennan and P. Turula

Components Technology Division

ARGONNE NATIONAL LABORATORY
U of C-AUA-USDOE

October 1978

Prepared for

U.S. Nuclear Regulatory Commission

DISCLAIMER

Available from
National Technical Information Service
Springfield, Virginia 22161

NUREG/CR-0442
ANL-CT-78-41
R5

EFFECTS OF AIR BLAST ON POWER PLANT STRUCTURES AND COMPONENTS

by

C. A. Kot, R. A. Valentin, D. A. McLennan and P. Turula

Components Technology Division

Argonne National Laboratory
9700 South Cass Avenue
Argonne, Illinois 60439

Manuscript Completed: August 1978

Date Published: October 1978

Prepared for

Division of Engineering Standards
Office of Standards Development
U.S. Nuclear Regulatory Commission
Under Interagency Agreement DOE 40-550-75
NRC FIN No. A2005

ABSTRACT

The effects of air blast from high explosives detonation on selected power plant structures and components are investigated analytically. Relying on a synthesis of state of the art methods estimates of structural response are obtained. Similarly blast loadings are determined from compilations of experimental data reported in the literature.

Plastic-yield line analysis is employed to determine the response of both concrete and steel flat walls (plates) under impulsive loading. Linear elastic theory is used to investigate the spalling of concrete walls and mode analysis methods predict the deflection of piping.

The specific problems considered are: the gross deformation of reinforced concrete shield and containment structures due to blast impulse, the spalling of concrete walls, the interaction or impact of concrete debris with steel containments and liners, and the response of exposed piping to blast impulse. It is found that for sufficiently close-in detonations and/or large explosive charge weights severe damage or destruction will result. This is particularly true for structures or components directly exposed to blast impulse.

TABLE OF CONTENTS

LIST OF FIGURES

LIST OF FIGURES (Contd.)

PREFACE

This report summarizes the results of an investigation conducted by Argonne National Laboratory (ANL) for the U.S. Nuclear Regulatory Commission (NRC) Office of Standards Development. The work was performed under a Standard Order for DOE Work (FIN No. A20057) with Dr. J. F. Costello, NRC serving as project monitor. His helpful suggestions and reviews are gratefully acknowledged. In addition to the report authors, personnel who contributed materially to the project effort are: Dr. B. J. Hsieh, ANL and Professor P. S. Symonds, Brown University. The latter was responsible for the development of the pipe response analysis presented in the Appendix.

C. A. Kot, Mechanical Engineer
Components Technology Division
Argonne National Laboratory
October 1978

EFFECTS OF AIR BLAST ON POWER PLANT STRUCTURES AND COMPONENTS

1. INTRODUCTION AND PROBLEM DESCRIPTION

The purpose of the effort, described in this report, is to investigate the effects of high explosive detonations on structures and components found typically in nuclear power plants. The specific interest lies in close-in detonations (1 to 100 feet from the structure) of explosive quantities which can reasonably be transported on site by motor vehicle (50 to 20,000 lb). The phenomena associated with such explosions are very complex and in general involve multiple loading effects, i.e. air blast, ground shock and direct shock in the case of near contact placement of the explosive. The current effort is limited to obtaining "first cut" estimates of the response to explosions and represents a synthesis of existing data, methods and procedures rather than an attempt at new research. Also attention is restricted exclusively to the effects of air blast on structures, this being the primary loading mechanism from explosive detonation.

Past efforts concerned with the effects of air blast on structures focus their attention primarily on the low and moderate overpressure range. It is usually assumed that the dimensions of the blast wave are large relative to those of the structure and that the shock wave is plane [1]. While such treatments are appropriate for very large explosions, such as those resulting from nuclear events, they are not suitable in the current application where the dimensions of the blast wave field and structure are of the same order of magnitude. The blast loading in this case is often very local and the variation of blast wave strength in its interaction with the structure must be accounted for. Also, blast wave durations may be shorter than the structure's clearing times, thus limiting the loads to one side of the structure. Past work for such blast loading has been limited to developing design procedures for explosive storage and manufacturing facilities [2]. The major

emphasis in these procedures is to determine the overall response of heavily reinforced concrete walls to the impulse load generated by the explosion. Loading on the wall face is assumed to be uniform. While these procedures are applicable to the problem under consideration, modifications must be introduced to account for the nonuniformity of loading which is important for the case of large structures and/or close-in explosions.

In addition to the containment or shield structures much of the nuclear power plant equipment is susceptible to air blast damage. The inherent redundancies and safety features, which help to minimize the hazards posed by air blast damage, as well as the physical plant layout may vary from installation to installation. It is not the objective of this study to investigate the vulnerability of specific power plants. Therefore, all analysis effort is concentrated on a few items which are not plant specific and whose failure or severe damage may by itself constitute a significant hazard. Specifically the study is limited to estimating the response of containment and shield structures as well as of piping runs outside of containment, such as main feedwater and steam lines. Both reinforced concrete and steel containment structures are considered.

A major simplification in the structural response analysis arises from the fact, that the loadings in most cases can be considered as impulsive, and that the details of pressure-time histories are of little consequence. The reason for this is that in general the structural response times are significantly larger than the blast wave durations, the latter being of the order of one millisecond. Thus primary emphasis is placed on gross structural response produced by the total impulse over the loaded area.

One exception are explosions close-in to concrete structures, where a direct strong shock wave is also transmitted into the wall due to the

reflection of the air shock at the surface. Wall damage may result in the form of spallation on the inner wall surface, when the shock wave reflects as a strong tension wave. This early time effect, produced by shock reflection, is strongly dependent on the blast wave pressure-time history and may lead to the formation of high velocity debris. Due to their high tensile strength steel structures loaded by air blast are not susceptible to spalling. The motion and deflection of concrete walls produced by the total blast impulse will continue long after the blast load ceases and can lead to a secondary spallation called scabbing [2], which is caused by shear and bending. This tends to separate the layer of concrete which covers the back face reinforcement. Again, this type of damage does not occur in steel structures, which will most likely fail due to the formation of plastic hinges. The same failure mechanism is expected for reinforced concrete walls. In fact the most severe damage of concrete walls occurs when the wall deflections are sufficiently large to cause substantial plastic deformation of the reinforcement. Ultimately complete wall destruction by shear plug separation or fragmentation of the loaded area may occur.

Steel containments are always surrounded by concrete shield structures. Therefore, they do not experience direct air blast loading, but they may suffer damage due to impact of concrete debris formed by spalling or disintegration of the concrete shield walls. Again the loading in such cases is primarily impulsive. For piping outside of containment the shock diffraction phase is of the same order of magnitude as the total duration of the blast wave. Thus no significant drag loading phase exists and the approximation of an impulsive load is again in general applicable.

Contact placement of the explosive and the use of special shaped charges is not considered in the current study. While the employment of these

techniques may result in the severest local structural damage, it is not possible to calculate damage estimates for these cases by means of simple analytical procedures. On the other hand, fairly reliable damage estimates may be obtained from experimental data contained in the demolition literature [3,4]. Since a precise definition of contact placement cannot be made, the closest charge placement here is arbitrarily limited to a scaled distance of 0.2 $ft/lbm^{1/3}$ or approximately 1.5 charge radii. While this distance is well within the fireball (6 charge radii) of the explosion, the peak reflected pressure at a wall ($\sim$68,000 psi) is still sufficiently moderate so that direct interaction and impedance matching of explosive to wall material may be neglected. Attention is restricted to the effects of bulk explosives and the analysis is simplified by assuming that the explosive charge is of spherical shape. The pressure loading of the wall is assumed to be that of a rigid surface. Thus structural motion or deformation does not alter the loading. In light of the impedance mismatch, between air and structural materials, and the shortness of a typical pressure loading this is a reasonable assumption.

In the current study response data are obtained for reinforced concrete walls and pipes subjected to air blast from close-in explosive detonations. Further the behavior of steel walls impacted by concrete debris is analyzed and the deformation of steel liners, attached to the inner side of concrete structures, under the action of loose concrete debris is estimated. Methods for calculating the spalling of concrete walls as well as for their deformation under impulsive blast loading have been presented earlier [5]. These techniques are summarized here (Sections 3 and 4) and representative results are given. Section 5 contains an outline of methods and typical results for the deformation of steel walls and liners under the action of concrete debris. Pipe

response under air blast loading is discussed in Section 6 and the details of the analysis method are presented in Appendix A. The estimation of air blast parameters and loads is discussed in Section 2.

Where possible, the results are scaled as a function of the explosive charge weight (energy). Even where scaling is not applicable all data is presented in terms of the scaled charge standoff distance. The response estimates are based on simplified engineering analysis and in general reduce to a few simple algebraic expressions. It is not practical in the limited space of a report, to present sufficient response information to cover all situations of interest to nuclear power plant applications. Therefore, an attempt is made to provide sufficient blast loading information, which is usually more scalable or can be presented in a more compact form, so that any case of interest is readily computable by using the simple response formulas.

2. AIR BLAST LOADING

The spherical air blast wave generated by an explosion undergoes a complex reflection and defraction process upon encountering a structure. The resulting local structural loading is time varying and depends on the blast wave peak pressure, its decay history, duration, and the angle of shock wave incidence. The blast wave structure interaction is best illustrated by the example of a flat wall. As shown in Fig. 1 when the spherical blast sweeps across the structure an ever increasing circular section of the wall becomes loaded. For a given explosive charge the local loading at any given circle of radius x is a function of the standoff y and the angle of incidence α. The detailed local interaction between the blast wave and the wall is illustrated in Fig. 2 at two different instances of time. In the first instant, blast wave reflection is still regular having a small angle of incidence while at the later time Mach reflection is indicated forming the familiar three shock configuration. This occurs at large angles of incidence (approximately angles larger than 40°). Also indicated in the figure are the shock waves induced in the wall by blast wave reflection and the stress waves resulting from their reflection at the back face of the wall.

Due to the complexity of the blast wave interaction with the wall, no analytical description of the blast loading is possible. Therefore, loading definition is obtained from experimental data systematized in the form of graphs and charts and collected over many years, primarily for defense applications. In the current work, Army Technical Manual TM5-1300 [2] is primarily used. Some inconsistencies exist in the data of this document; however, the information presented is reasonably complete. Where necessary, the data has been supplemented with information from other sources [6].

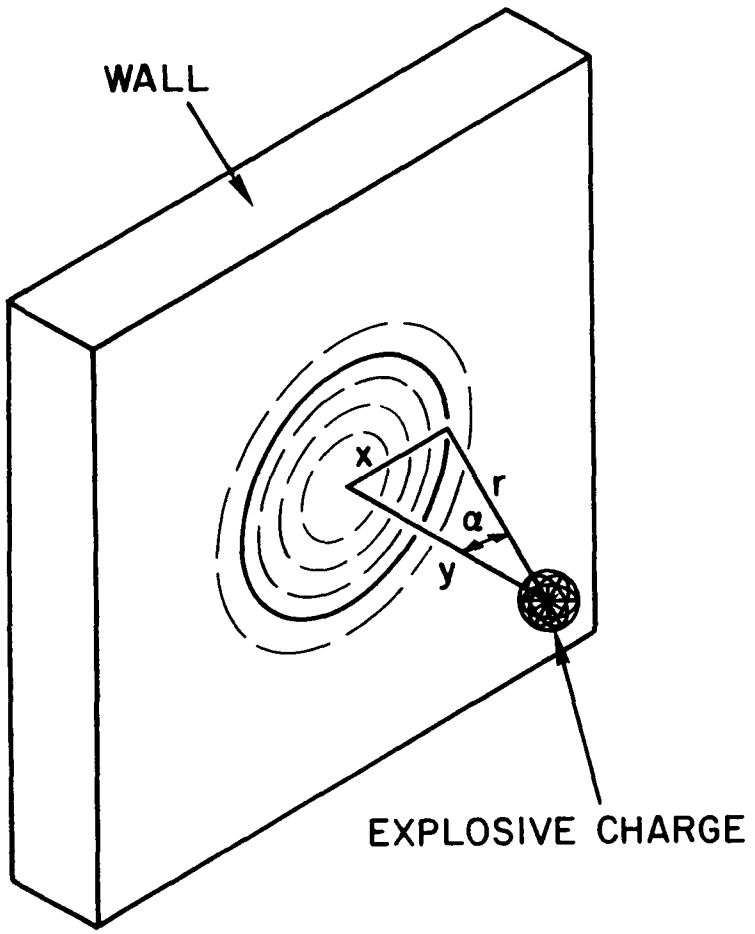

Fig. 1. Schematic of Explosive Charge and Wall

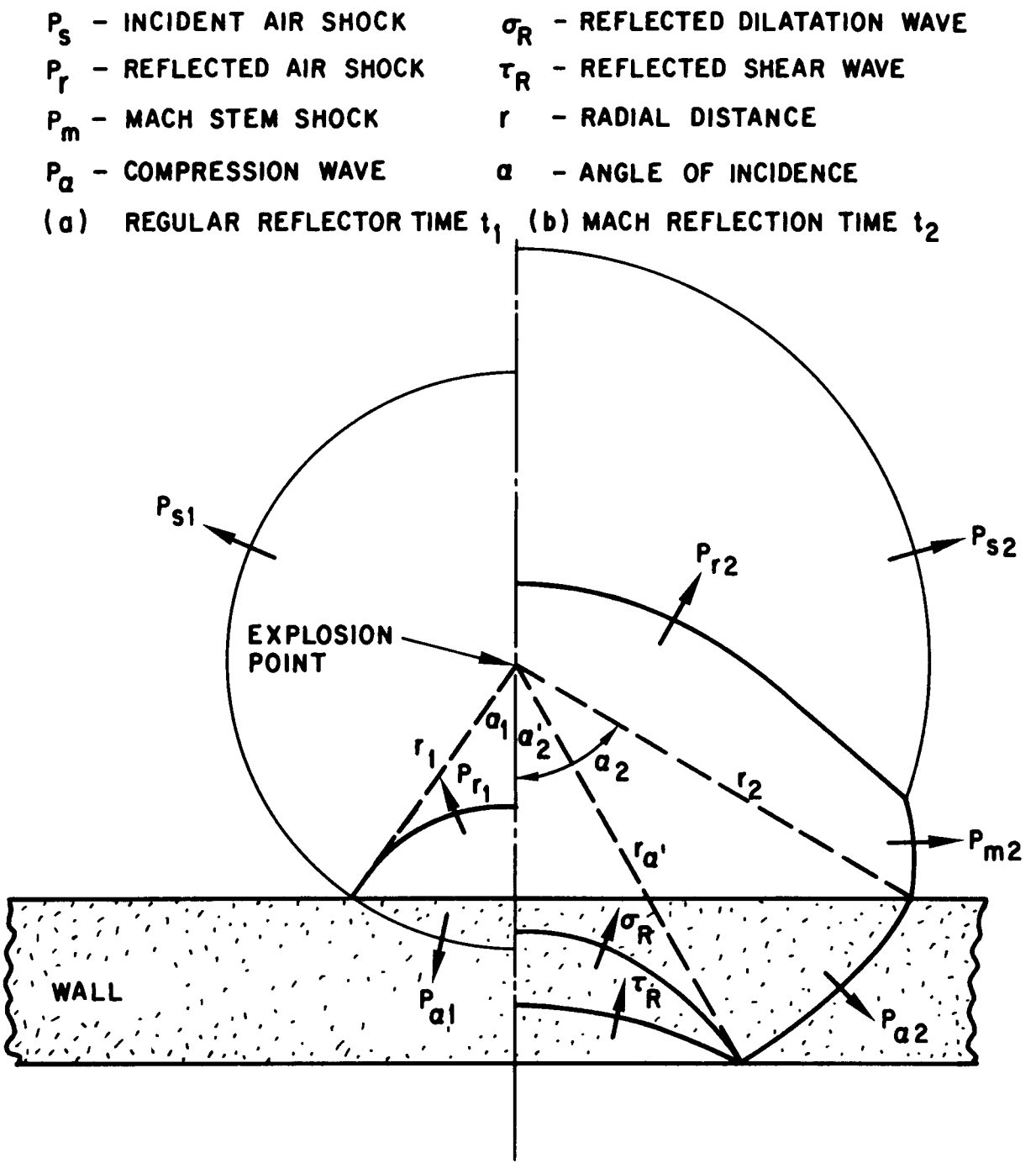

Fig. 2. Air Blast Interaction with a Wall

The basic variables of interest to blast loading of structures are shown in Fig. 3. These are taken from Figure 4-5 of TM5-1300 [2] and are given as a function of scaled distance $z = r/W^{1/3}$, where r is the distance from the center of the explosive charge to the point of interest on the structure and W is the TNT equivalent charge weight. The curve labeled p_s is the peak incident shock pressure and i_s represents the scaled positive impulse of the incident blast wave. The p_r and i_r curves are respectively the peak reflected pressure and the scaled positive reflected impulse for a normal blast wave incidence on the structure, i.e. $\alpha = 0$ (see Fig. 1). It should be noted that quantities referred to here are scaled but not nondimensionalized, hence the following units must be used: lb for charge weight, $ft/lb^{1/3}$ for scaled distance, psi for pressures and $psi\text{-}s/lb^{1/3}$ for impulses.

The maximum pressure experienced by a rigid surface that is in the path of the blast wave is the peak reflected pressure denoted by $p_{r\alpha}$. This is dependent on the angle of incidence, α, which is the angle between the direction toward the center of the explosion and the direction of the normal to the surface of the wall, and on the value of the incident pressure p_s at the point under consideration. The reflected pressure $p_{r\alpha}$ is given by the relationship

$$p_{r\alpha} = C_{r\alpha} p_s \tag{1}$$

where $C_{r\alpha}(\alpha, p_s)$ is the experimentally determined reflection or amplification factor which is presented graphically in Fig. 4. The values shown are a synthesis of data given in TM5-1300 [2] and more recent data obtained by Carpenter and Brode [6]. The latter information is primarily used for values of α over 40°. At large distances and nearly glancing incidence, i.e. α close to 90°, the explosion in the vicinity of a large structure takes on the

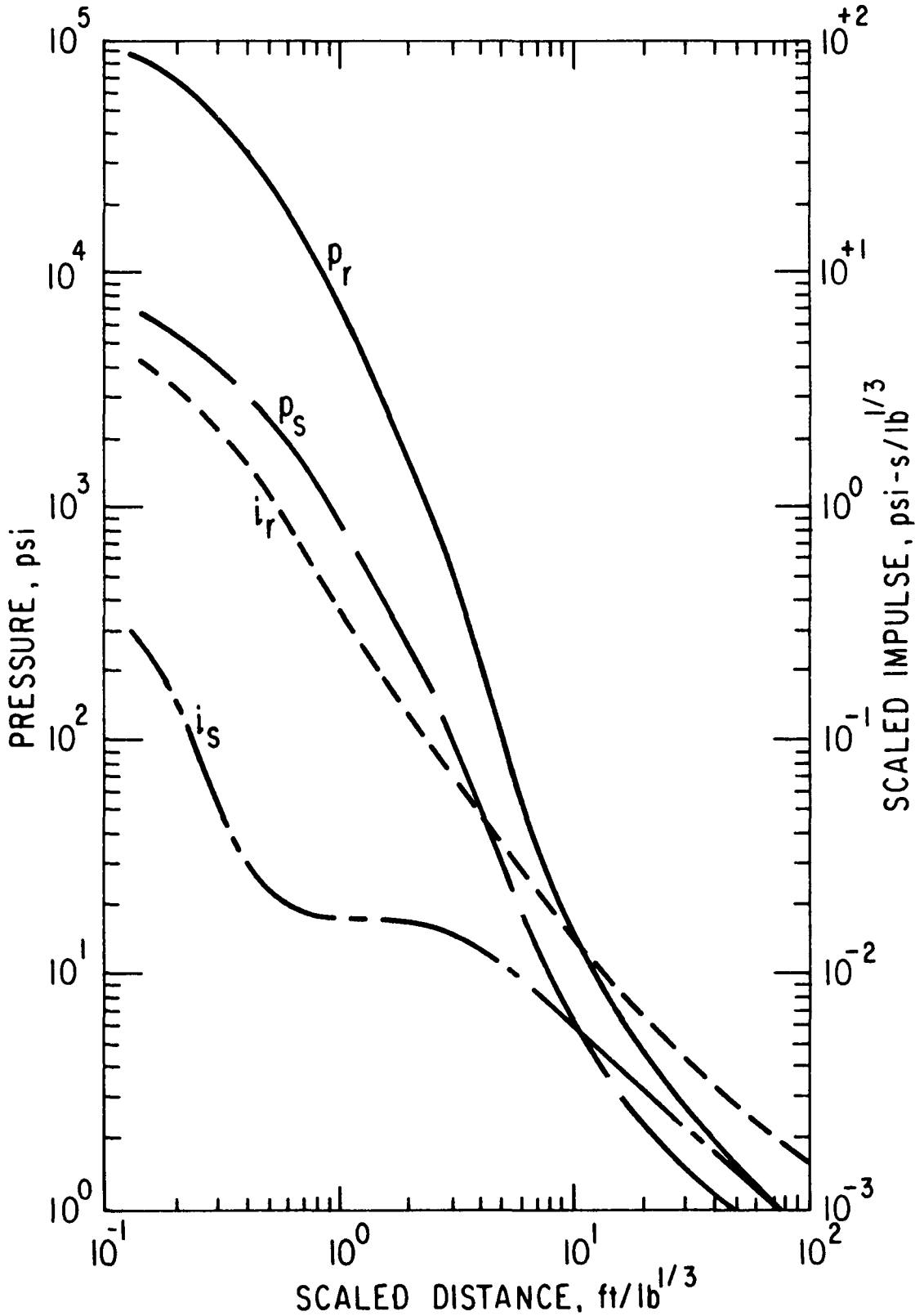

Fig. 3. Air Blast Variables

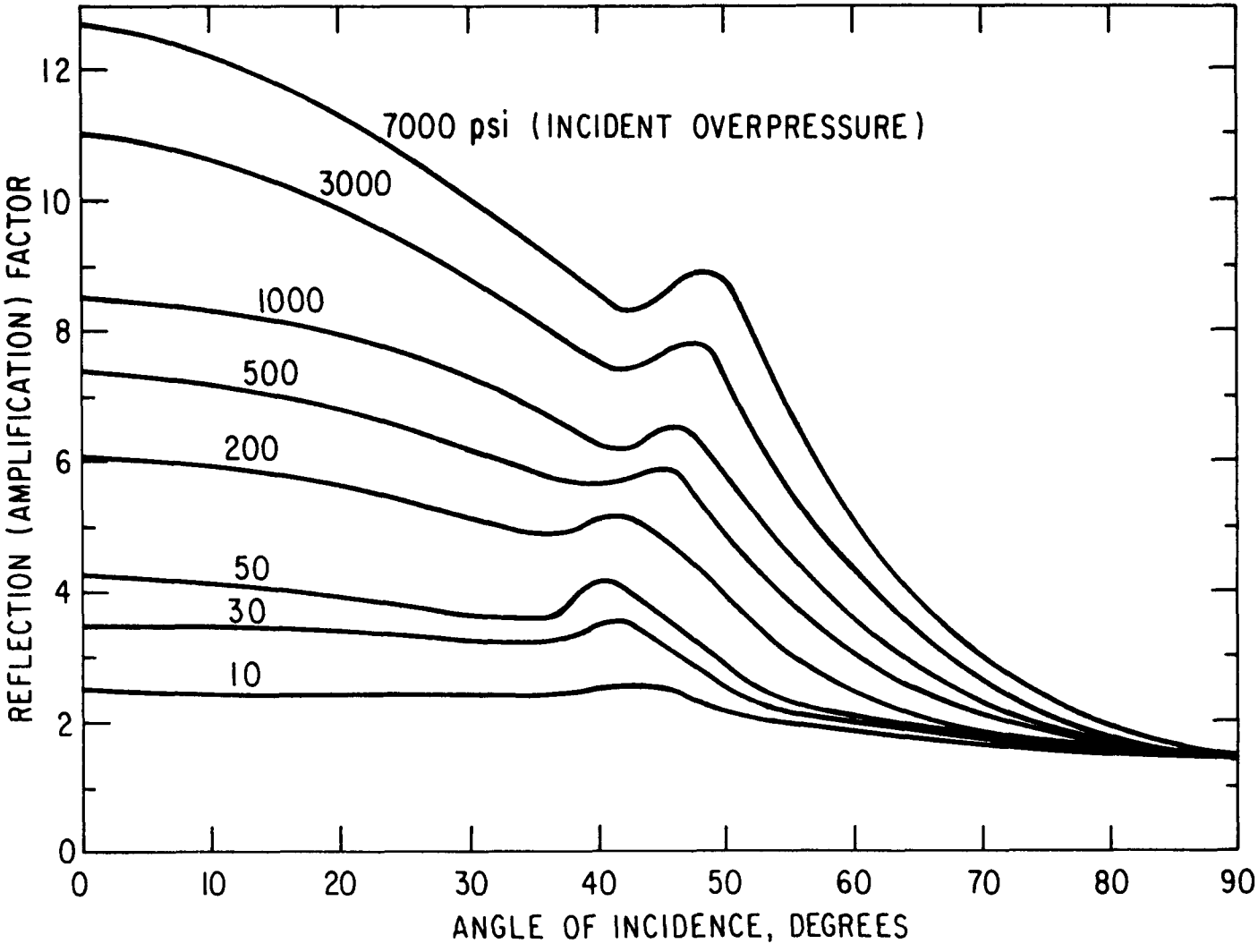

Fig. 4. Blast Wave Reflection (Amplification) Factors

characteristics of a surface burst. This fact was employed to construct the curves of Fig. 4 at large angles of incidence. While the ratio of pressures (surface burst to free air burst at the same scaled distance) appears to be variable [2] the selected value of an amplification factor of 1.5 at 90° represents a reasonable average. The variation of $p_{r\alpha}$ across the surface of a structure can thus be obtained from Eq. (1) using the information of Figs. 3 and 4.

With $p_{r\alpha}$ determined, Fig. 3 is reentered to find a fictitious value of the scaled distance z from the reflected pressure (p_r) curve. Using this z value the corresponding scaled positive reflected impulse $i_{r\alpha}$ is found from the i_r curve. This one to one correspondence between $p_{r\alpha}$ and $i_{r\alpha}$ postulated in TM5-1300 [2] is accepted for the purposes of this study even though it leads to some inconsistencies, eg. impulses which are not compatible with the peak pressure and the positive phase duration. The assumption appears to be sufficiently good for scaled distances below z = 1, where the most severe loading occurs.

The total positive reflected impulse I_T, delivered to any section of a structure, is computed by integrating the local values of impulse $i_{r\alpha}$ over the area of interest. For flat walls this is a simple procedure however when structural surfaces are curved then a complex numerical procedure is required to obtain the total impulse. Results of the total impulse loading for specific configurations are presented in the following sections dealing with the structural response. In all of these computations the differences in timing of the impulsive load at various positions on the structure are ignored. This is justified since both arrival time differences and blast wave durations are substantially shorter, of the order of one millisecond, than the structural response times. Thus for all structural calculations it is assumed that the impulse is applied instantaneously over the entire section of interest. This should in general give conservative results.

As pointed out elsewhere [5] the spalling of concrete walls is strongly dependent on the wave form (pressure-time history) of the reflected blast wave. Of interest are reflections in the high pressure region, where little information is available concerning the wave form shape. In general the pressure decay is exponential, however recent experiments [6] indicate that the wave forms are more complex, particularly in the Mach-stem reflection region where two pressure peaks have been observed. To obtain computational estimates of spalling a simple analytical description of the wave forms, which was originally derived to describe nuclear explosions in air [7], is employed. The expression was found to be in reasonably good agreement with wave forms predicted by detailed numerical computations for a TNT explosion [8]. The equation takes the form of a triple exponential, which relates the time dependent pressure p to the peak blast wave pressure p_s and the dimensionless positive phase duration $\tau = t/t_+$, where t is time measured from shock arrival and t_+ is the positive phase duration of the pressure.

$$p(\tau) = p_s (1 - \tau) (ae^{-\alpha\tau} + be^{-\beta\tau} + ce^{-\gamma\tau}) \qquad (2)$$

The coefficients (a,b,c) and the exponents (α,β,γ) are functions of p_s. Values of these parameters were obtained from Fig. 24 of Reference [7]. Of interest to spall calculations is the wave form of the reflected pressure. Consistent with the assumptions for impulse loading made earlier, it is assumed that the duration of the reflected wave is equal to that of the incident wave and that the decay of both waves is similar. Hence, the parameters corresponding to the incident peak overpressure also describe the reflected wave.

While equation (2) is simple and could be used when numerical spalling calculations are carried out, it is not possible to obtain analytical spall

solutions with this wave form. To generate such analytical estimates the decaying pressure wave is locally approximated by a simple power law

$$p(\tau) = p_s \ (1 - \tau^{\gamma}). \qquad (3)$$

The exponent γ is a function of peak pressure p_s and varies also along the pressure decay, i.e. it depends on the ratio p/p_s. Values of γ are calculated by matching, for each peak pressure p_s, the pressures p obtained from equation (3) with those from equation (2). Fig. 5 is a graphical presentation of the values of γ thus obtained.

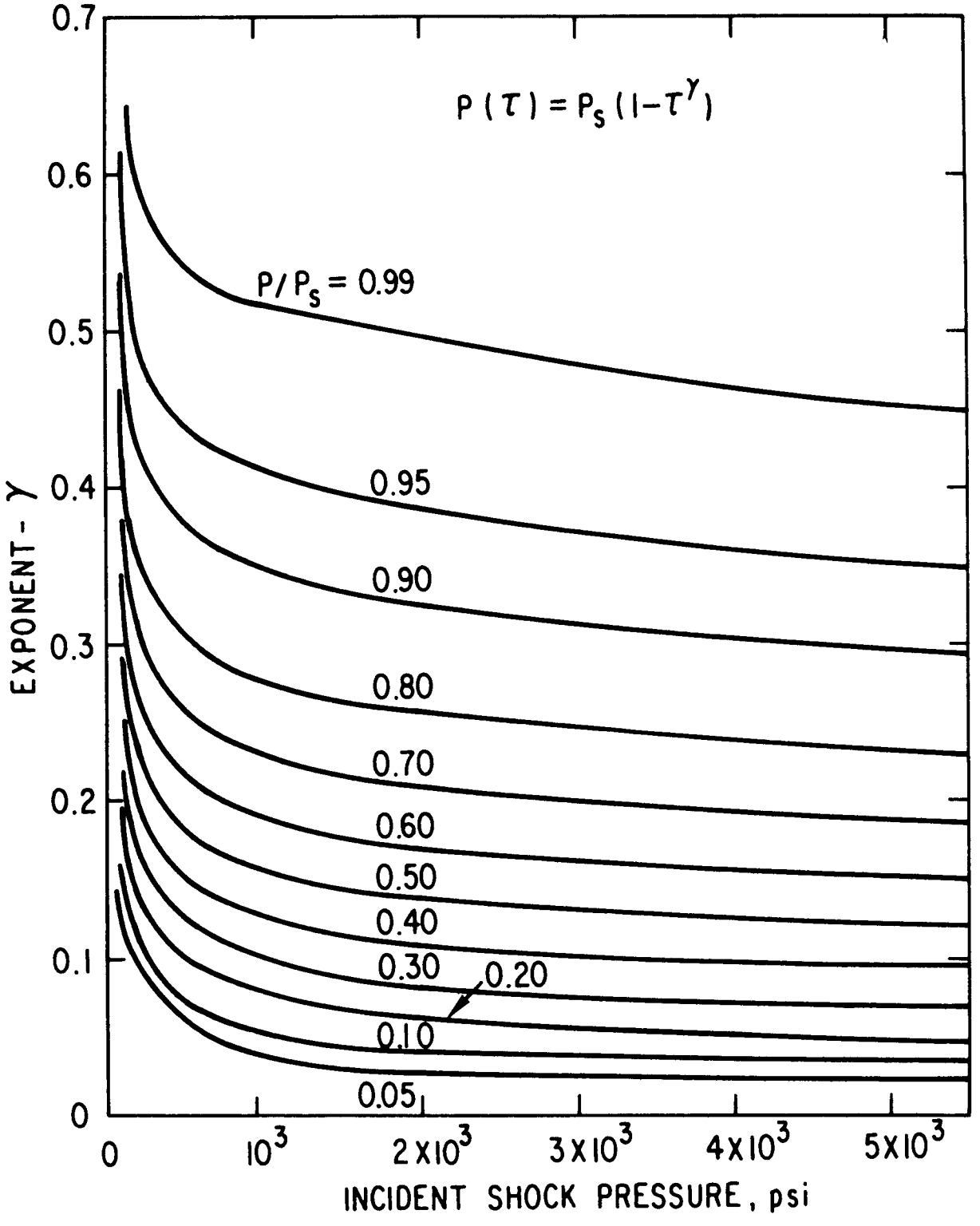

Fig. 5. Variation of Pressure Wave Form Exponent

3. CONCRETE WALL RESPONSE TO AIR BLAST IMPULSE

Both flat and curved concrete walls are encountered in shield and containment structures of nuclear power plants. Their dimensions are of the order of 50 to 100 ft with radii of curvature having similar magnitudes. Therefore blast loadings for all charge weights considered here will be localized. In a "first cut" response analysis it is then conservative to assume that the walls are flat and uniform extending sufficiently far in all directions so that boundaries may be neglected. Since the reflected pressures experienced by the structures are in general very high (>1000 psi) both the elastic part of the response and the shear resistance of the loaded wall sections are not significant [5]. It is also assumed that enough structural ductility exists to sustain large displacements under a constant ultimate load. Both prestressed or conventionally reinforced concrete walls are considered.

The structural analysis of the effects of the explosion consists of two phases: first, computation of the blast loading, according to the procedures outlined in Section 2, and second, evaluation of the wall resistance. In the first phase it is assumed that the wall provides no material strength to resist the impulse associated with the applied blast load. The only resistance available is provided by the inertia of the mass of the wall. In the present approach, given the total impulse and the total mass, a single velocity imparted to the entire wall segment under consideration is computed. During the resistance phase the ultimate load carrying capacity of the reinforced concrete structure is developed to provide a decelerating force which brings the wall back to rest. The total wall deflection or its rotation can then be compared with damage criteria. The latter may be either some maximum permissible material deformation or an emperical limit, which if exceeded is known to result in severe structural damage.

3.1 LOADING PHASE

The procedure for obtaining the local scaled impulse per unit area $i_{r\alpha}$ at any point of the wall was outlined in Section 2. Given a charge weight W these values may be converted to actual impulses per unit area, i.e.

$$I_{r\alpha} = W^{1/3} i_{r\alpha} \tag{4}$$

Integration of the local impulses over the loaded area results in the total impulse. In the case of a flat wall the total impulse I_T is easily computable.

$$I_T = \int_0^x I(x,y)\ 2\pi x\ dx \tag{5}$$

Here the notation of Fig. 1 has been used. The local impulse values I(x,y) are given as functions of the standoff distance y and the radial coordinate x. Each I(x,y) is obviously equivalent to the corresponding $I_{r\alpha}$. Since no analytical expressions exist for the local impulse the integration is carried out numerically. It should be noted that all the variables on the right hand side of Eq. (5) are scalable, hence the total impulse can also be scaled. Introducing $z_x = x/W^{1/3}$ and $z_o = y/W^{1/3}$ one can write

$$i_T = I_T/W = 2\pi \int_0^{z_x} i(z,z_o)\ z\ dz \tag{6}$$

where i_T is the scaled total impulse over the circle with scaled radius z_x at a scaled standoff distance of z_o and z is the integration variable (scaled radius) along the wall. A graphical presentation of the relationship between i_T and z_x for various values of z_o is given in Fig. 6. This data is universal and can be used to evaluate the impulse over any circular area on a flat wall.

During the loading phase it is assumed that the only resistance offered to motion is by the inertia of the loaded wall segment. The velocity attained

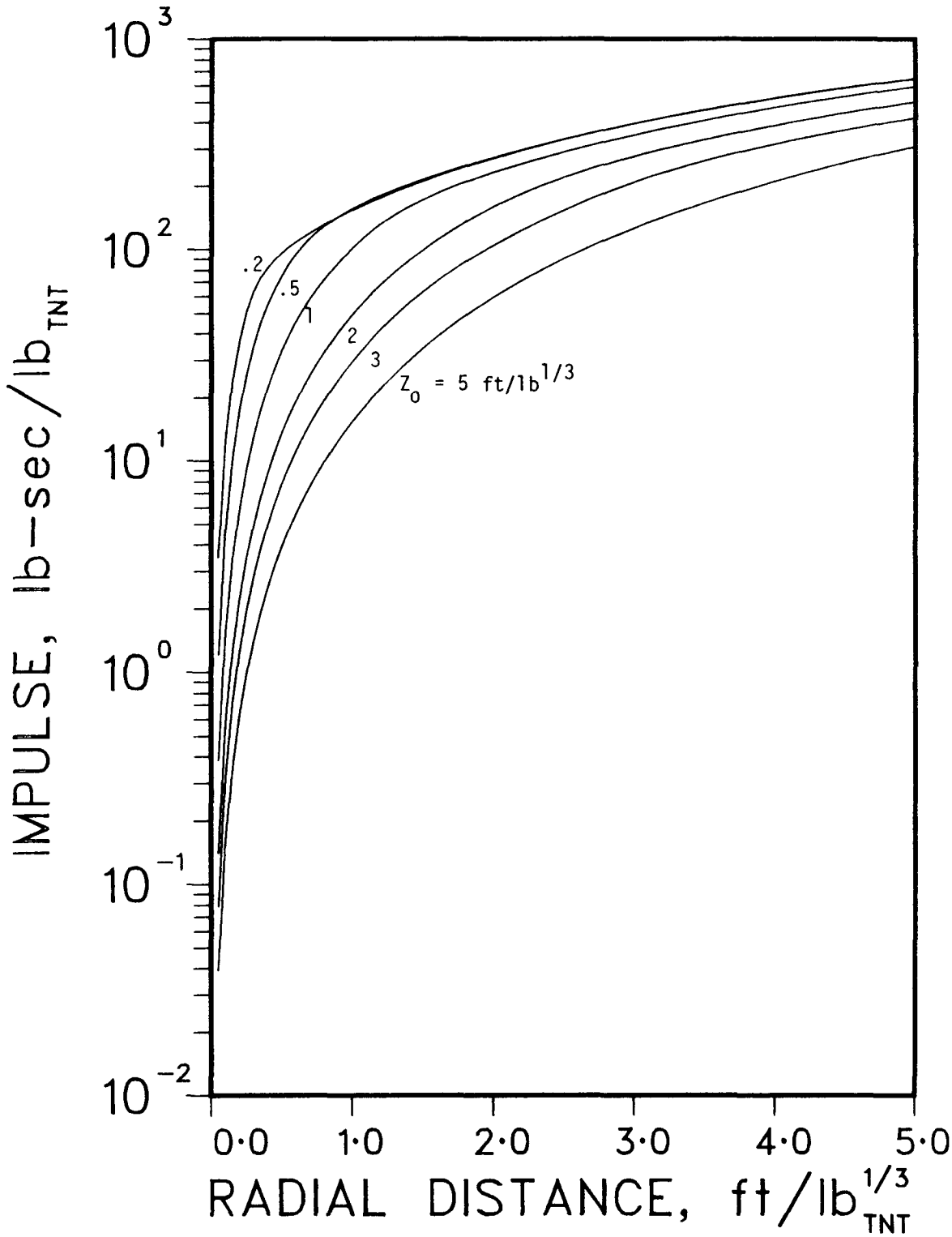

Fig. 6. Scaled Total Blast Impulse on a Flat Wall

by the wall segment is then simply

$$v = \frac{I_T}{M} \tag{7}$$

Here M is the mass of the circular wall segment given as

$$M = m \pi x^2 = m \pi W^{2/3} z_x^2 \tag{8}$$

where m is the mass per unit area of the wall. Since the mass, for a given wall, is proportional to the square of the radius x it will scale with $W^{2/3}$. This is indicated by the second equality in Eq. (8). The total impulse scales directly with the charge weight W (see Eq. (6)), hence based on Eq. (7) the velocity of an impulsively loaded wall segment will scale with the cube root of the charge weight. This scaled velocity is wall specific because of its dependence on m the mass per unit area. However, it is possible to construct a general velocity variable, u, which includes the parameter m, as follows:

$$u = \frac{vm}{W^{1/3}} = \frac{2}{z_x^2} \int_o^{z_x} i(z,z_o)\, z\, dz \tag{9}$$

Again this variable is only a function of the scaled standoff z_o and the scaled radius of the wall segment z_x. Fig. 7 represents the velocity variable as a function of the scaled standoff z_o for various wall response limits. As will be seen in later sections of this report these curves do not correspond to any fixed values of scaled radial distance z_x. Rather z_x varies with the standoff distance, e.g. for the velocity at the spall limit curve $z_x = z_o$ (α = 45 deg.).

3.2 WALL RESPONSE AND RESISTANCE

An implied assumption in separating the wall response from the loading phase is that the motion of the wall does not affect the magnitude

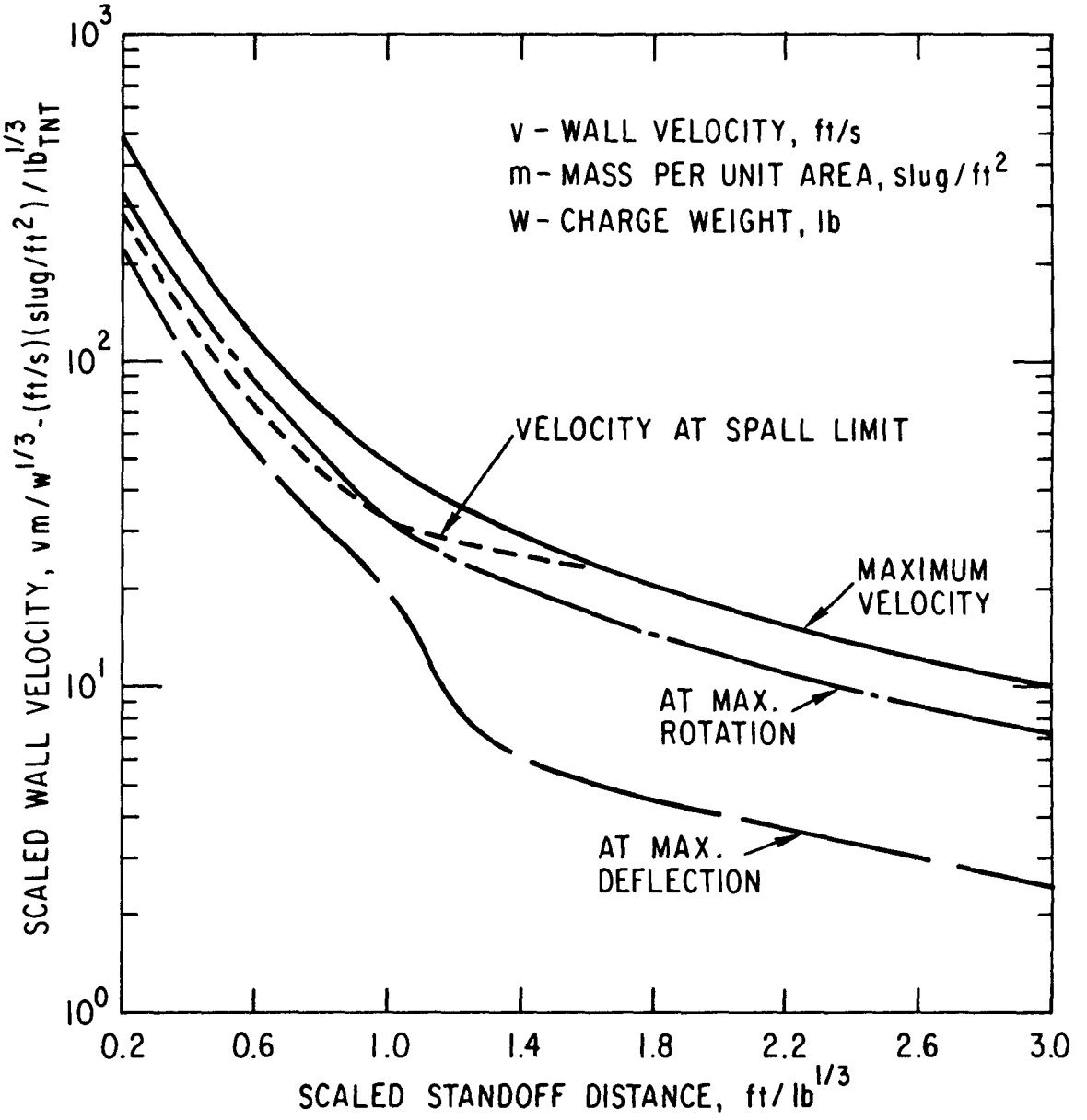

Fig. 7. Scaled Concrete Wall Velocities due to Impulsive Air Blast Loading

of the blast loading. This assumption is justified because the duration of the impulse is short relative to the response time of the structure. Any motion of the structure during the blast loading period is therefore minimal. Similarily the assumption of no structural resistance during loading is acceptable because for most cases the shear stresses resulting from the application of the pressure forces substantially exceed the shear strength of the concrete [5].

Several mechanisms can be postulated to compute deflections of wall segments due to the impulse of the blast. Ultimate strength analysis, which is commonly used for the design of reinforced concrete structures, was found to be most appropriate for the current application [5]. This analysis assumes plastic yielding under a constant resistance force F_R and completely neglects the elastic strength of the material. The deflection of the wall δ can be computed from the kinetic energy of the loaded wall segment, of mass M, and initial velocity v imparted by the blast impulse.

$$\delta = \frac{Mv^2}{2F_R} \tag{10}$$

Due to the restraining effect of the inertia of the entire wall surrounding the loaded wall segment a circular yield line pattern, similar to that of a clamped circular plate, is expected to form. The uncertainties in the circumferential support conditions of the loaded wall segment, which is neither clamped or simply supported, and in the load distribution make an estimate of the ultimate load capacity F_R difficult. Consideration of all the factors [5] lead to the following simple compromise expression

$$F_R = 10\ M_o. \tag{11}$$

Here M_o is the ultimate moment assuming that the wall is equally reinforced on both faces, or the average ultimate moment if the reinforcements, are different.

For conventionally reinforced concrete walls the ultimate moment is [9]

$$M_o = A_s f_s (d - \tfrac{1}{2}a) \tag{12}$$

where A_s is the reinforcement steel cross-sectional area per unit width (height) of wall, f_s is the steel yield strength, d is the effective depth of reinforcement from the loaded face of the wall, and a is the concrete compression block depth. The latter can be evaluated by equating the compression force in the concrete to the tension force of the reinforcement at yielding. The compression is assumed to act over an equivalent block of uniform stress [9], of intensity $0.85 f_c$, where f_c is the concrete compression strength. Hence one obtains

$$a = \frac{A_s f_s}{0.85 f_c} \tag{13}$$

When spalling or scabbing of the concrete covering the reinforcement is expected, the expression for the ultimate moment is modified [2]

$$M_o = A_s f_s d_c \tag{14}$$

where d_c is the distance between the centerlines of the front and backface reinforcement. For prestressed concrete walls the computation of the ultimate moment M_o is considerably more complicated. It must be based on the full plastic strength of the prestressing tendons and their location in the wall cross-section. An average value of M_o for horizontal and vertical directions as well as different bending directions is determined and used to compute the ultimate load capacity F_R.

Eq. (10) can be rewritten in terms of the total impulse I_T and the ultimate moment M_o.

$$\delta = \frac{I_T^2}{20 M M_o} \tag{15}$$

The rate of increase of total impulse with radial distance along the wall varies significantly, being very high for very small radii and diminishing as the radius increases (see Fig. 6). On the other hand the mass of the circular wall segment increases as the square of the radius. Therefore based on Eq. (15) one may expect a maximum displacement δ to exist. Since no analytical expression for δ in terms of radius exists the maximum is found numerically by evaluating the expression over circles with ever increasing radii until the critical value is located. To be conservative in the wall deflection estimates it is this maximum value of δ which is used.

It is readily noted from either Eq. (10) or (15) that the deflection δ is a scalable quantity. Since the impulse is proportional to the charge weight W and the mass scales as $W^{2/3}$ one finds that δ scales as $W^{4/3}$. Again to eliminate the dependence on specific wall parameters a universal wall deflection variable may be constructed which represents the maximum deflection as a function of the scaled standoff distance only, i.e.

$$\Delta = \frac{\delta \; m \; M_o}{W^{4/3}} \tag{16}$$

The resulting curve is shown in Fig. 8. It can be used to estimate the maximum deflection for any specific wall (parameters m and M_o) under the action of an impulsive blast loading resulting from an explosion of charge weight W, detonated at any arbitrary standoff distance y. The velocity of the wall segment corresponding to this maximum deflection is shown in Fig. 7. The particular shape of this curve results from the fact that for close-in explosions the maximum deflection occurs when the plastic hinge radius x (radius of loaded segment) is approximately one and one half times the standoff distance y, i.e. $x/y \simeq 1.5$, while for larger standoff distances the ratio is $x/y \simeq 3.7$. A sharp transition occurs between these two regimes around a

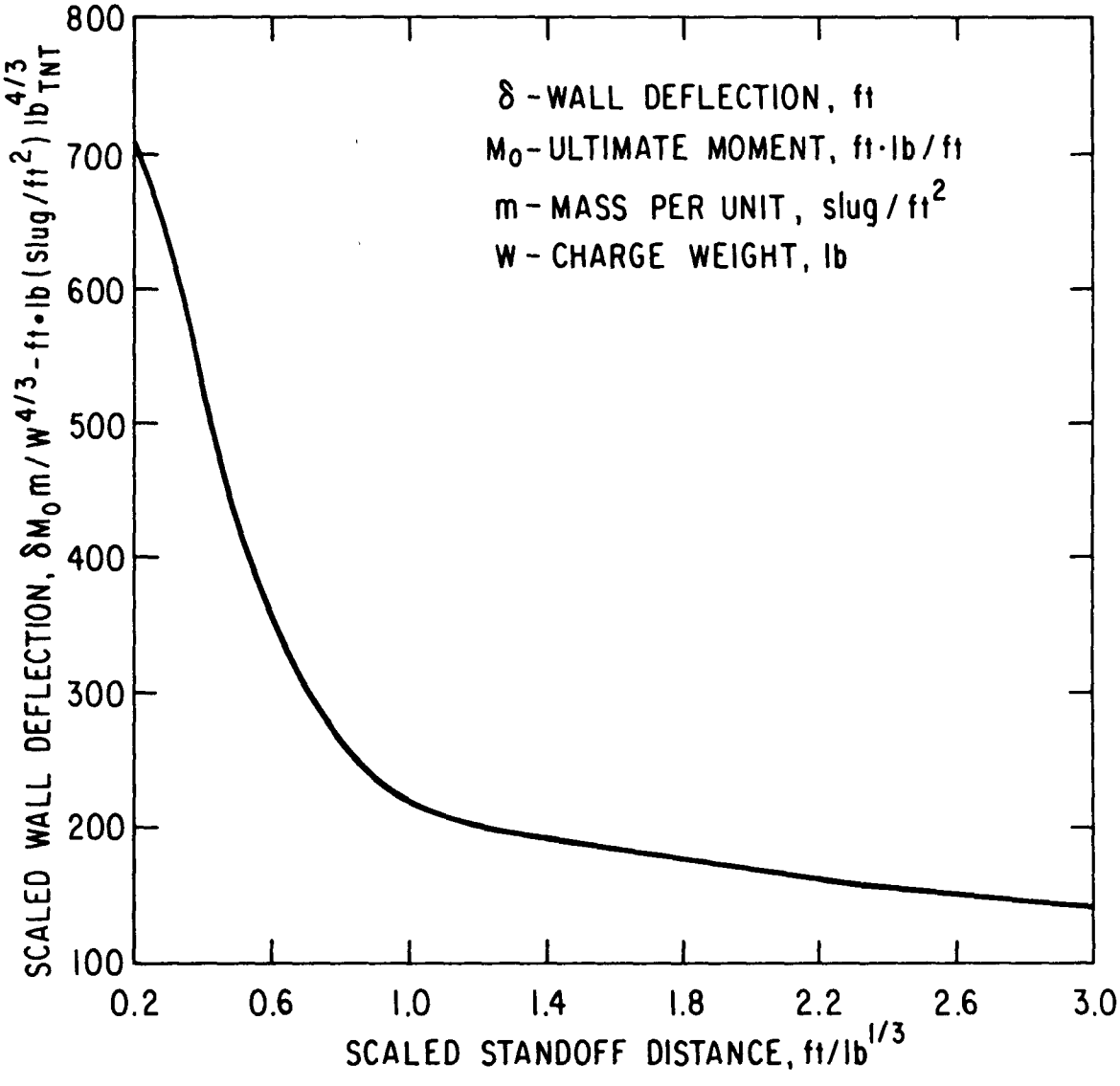

Fig. 8. Scaled Deflection of Concrete Wall due to Impulsive Air Blast Loading

scaled standoff distance z_o = 1 ft/lb$^{1/3}$.

Another measure of wall damage is the rotation or angular deflection the wall experiences at the plastic hinge radius. For the circular yield pattern assumed here the tangent of this rotation angle θ is simply the ratio of wall deflection to the radius of the plastic hinge circle, i.e.

$$\tan\theta = \frac{\delta}{x} \tag{17}$$

Again a maximum rotation exists for each charge standoff distance which must be found by numerical means, i.e. by integrating over increasing circles. The maximum rotation angle θ does not coincide with the maximum of the deflection δ. In general it has been found that the maximum θ occurs before (at smaller hinge radii than) the maximum δ. For the range of scaled standoff distances from 0.2 to 3.0 the ratio of hinge radius to standoff x/y, at maximum θ, varies from 0.75 to 1.10. To be on the conservative side the maximum value of θ will be used to indicate wall damage rather than the value corresponding to the maximum deflection.

From Eq. (17) it is obvious that $\tan\theta$ is a scalable quantity. The deflection δ scales as $W^{4/3}$ and the radius x scales as $W^{1/3}$, therefore $\tan\theta$ is directly proportional to the charge weight W. Again a universal wall rotation variable, which contains the wall specific parameters, can be constructed.

$$\theta = \frac{M_o \; m \; \tan\theta}{W} = \frac{\Delta}{z_x} \tag{18}$$

The relationship between the scaled wall rotation variable of Eq. (18) and the scaled standoff distance is shown in Fig. 9 while the wall velocity corresponding to the same loading is given in Fig. 7. It should be noted that the scaling pertains only to the function $\tan\theta$ and not to the angle θ

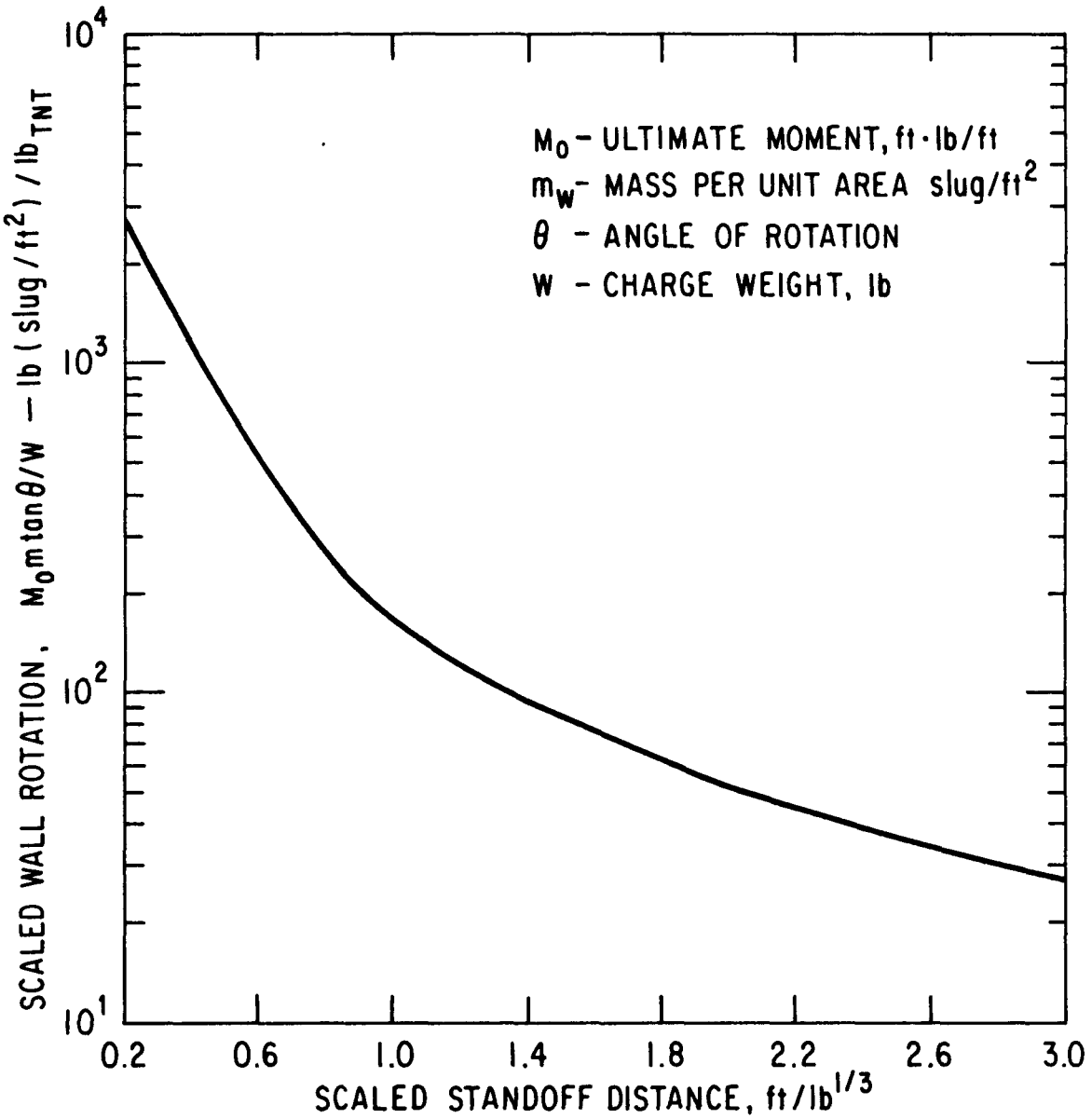

Fig. 9. Scaled Hinge Rotation for Concrete Wall under Impulse Loading

itself. The reason for this is, that only $\tan\theta$ can be directly expressed in terms of scaled quantities and that the relationship between θ and the trigonometric function is neither linear nor a simple power law depedence. Nevertheless the information of Fig. 9 can be readily employed to estimate the maximum rotation at the hinge line for any reinforced concrete wall under impulsive blast loading.

By virtue of the assumption that the elastic response can be neglected, the application of the procedure outlined above must be restricted to loadings which indeed produce large plastic deformations. The upper limit of applicability will be dictated by the failure or rupture strains of the reinforcement steel. For the circular yield patterns assumed here the relationship between strain ε and the hinge rotation θ can be approximately stated as

$$\cos\theta = \frac{1}{1+\varepsilon} \tag{19}$$

Thus for example if the rupture strain of the reinforcement is $\varepsilon = 0.10$ then the computational results may be applied to rotation angles up to 25°.

Both very small charges as well as extremely large charge weights should not be treated by the analysis. For small charges there will be no gross plastic deformation of the wall. For very large charges, particularly at large standoff distances, the assumption of local loading and deformation of a single wall becomes invalid. While no precise limits on charge weight can be established, it appears that applicability of the wall response calculations should be approximately restricted to the range of 50 - 20,000 lb of TNT.

3.3 EXAMPLES OF WALL RESPONSE COMPUTATIONS

The methods and procedures outlined above are applied to two typical walls in order to estimate their maximum deflections and rotations under the action of explosive charge detonation. The examples also illustrate

the procedures which may be employed to establish acceptable limits on either charge weight or standoff distance, based on selected damage criteria. Since the computations for the two example walls have been detailed elsewhere [5], only a summary of their physical and geometrical descriptions is presented below:

a - Conventional Reinforced Concrete Wall

Wall thickness	$h = 30$ in.
Concrete Compression strength	$f_c = 4{,}500$ psi
Steel yield strength	$f_s = 60{,}000$ psi
Reinforcement in each face and in each direction	$A_s = 1.5$ in^2/ft
Effective depth of reinforcement	$d = 27$ in.
Ultimate moment (Eq. (12) and (13))	$M_o = 0.195 \times 10^6$ ft-lb/ft
Ultimate load capacity (Eq. (11))	$F_R = 1.95 \times 10^6$ lb

b - Prestressed Concrete Wall

Wall thickness	$h = 42$ in.
Concrete compression strength	$f_c = 4500$ psi
Conventional steel yield strength	$f_s = 60{,}000$ psi
Tendon yield strength	$f_t = 240{,}000$ psi
Plastic strength of each tendon, 170-1/4" diameter strands	$T_p = 2.0 \times 10^6$ lb
Tendon spacing - horizontal	$s_H = 27$ in.
vertical	$s_V = 48$ in.
Tendon location - horizontal	$l_H = 6$ in., from outside face
vertical	$l_V = 21$ in., at centerline
Horizontal reinforcement-inside face	$A_s = 1.27$ in^2/ft

Effective depth		$d = 39$ in.
Ultimate moment -	vertical tendons	$M_{oV} = 0.7 \times 10^6$ ft-lb/ft
	horizontal tendons	$M_{oH} = 2.0 \times 10^6$ ft-lb/ft
	horizontal reinforcement	$M_o = 0.24 \times 10^6$ ft-lb/ft
Average ultimate moment		$\bar{M}_o = 0.9 \times 10^6$ ft-lb/ft
Ultimate load capacity		$F_R = 9.0 \times 10^6$ ft-lb/ft

The results for Wall Type-a and Wall Type-b are summarized in Fig. 10 and Fig. 11 respectively. Shown are iso-deflection curves and iso-rotation curves as they depend on charge weight and standoff distance. The results are for close-in deformations in the range of scaled standoff from 0.2 to 1.0 ft/lb$^{1/3}$. If displacement of the wall is to be limited to a specific value, say 1 ft, then the charge weights that can be tolerated at any specific standoff distance can be determined from the figures. Alternately given a maximum charge weight the required standoff distance may be obtained again for a specific deflection limit. The limits on displacement may be considered as "functional" limits. The severity of the effects caused by a particular deflection depends not only on wall type and thickness but also on the structural dimensions. Thus, for the same deflection, a wall with a small span may suffer considerably more damage than a larger wall. On the other hand rotation limits can be easier related to local structural damage since they are based on maximum reinforced concrete ductility. Thus TM5-1300 [2] recommends that rotation at a yield line, as defined by conventional ultimate load analysis, be limited to 5° where structural integrity is to be maintained. If large deformations and scabbing are to be allowed then TM5-1300 [2] recommends a 12° limit on yield line rotation. The curves corresponding to these two limits are shown in Figs. 10 and 11. It can be seen that the critical

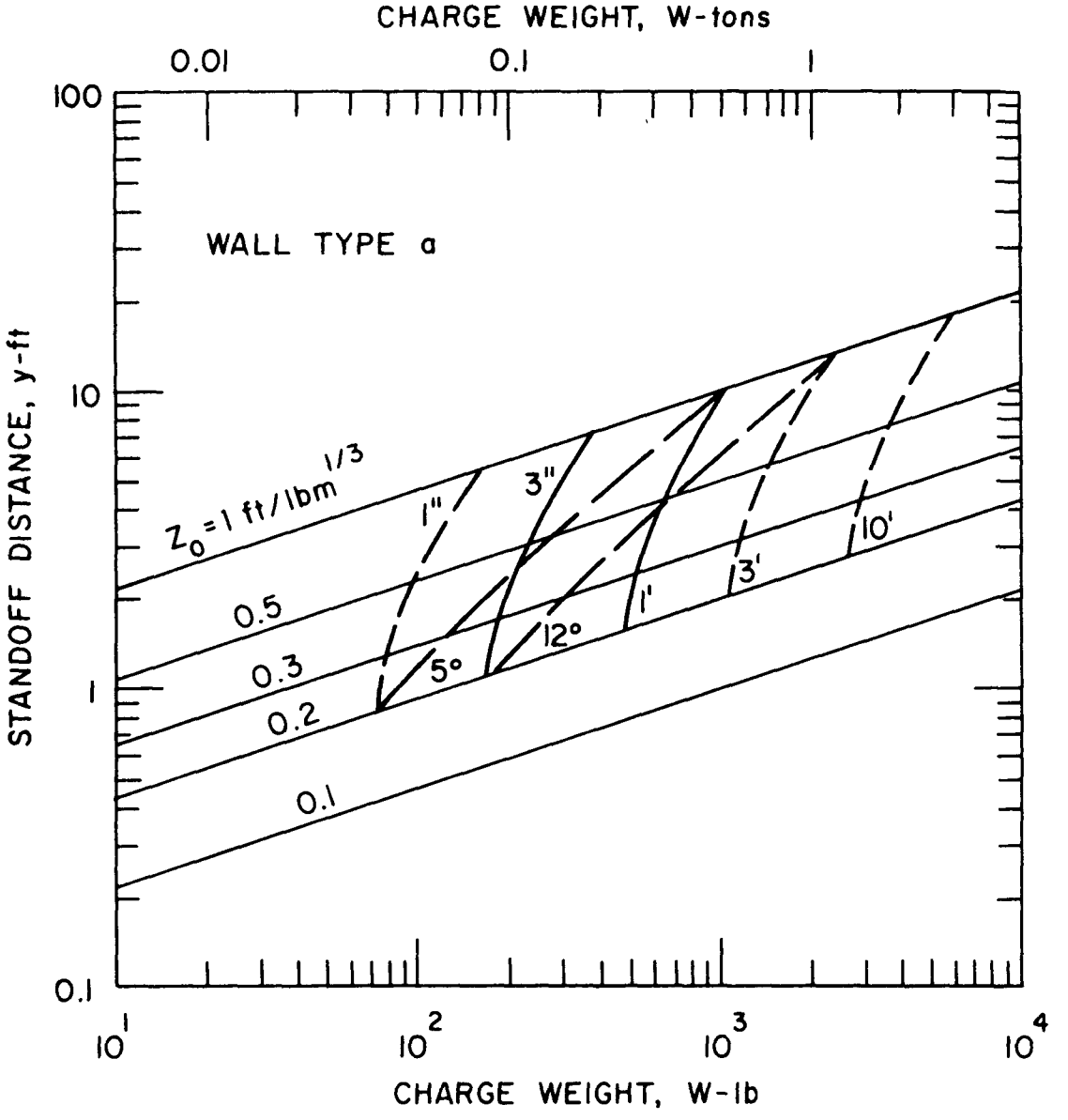

Fig. 10. Deflections and Deformation Criteria as a Function of Charge Parameters for Wall Type a

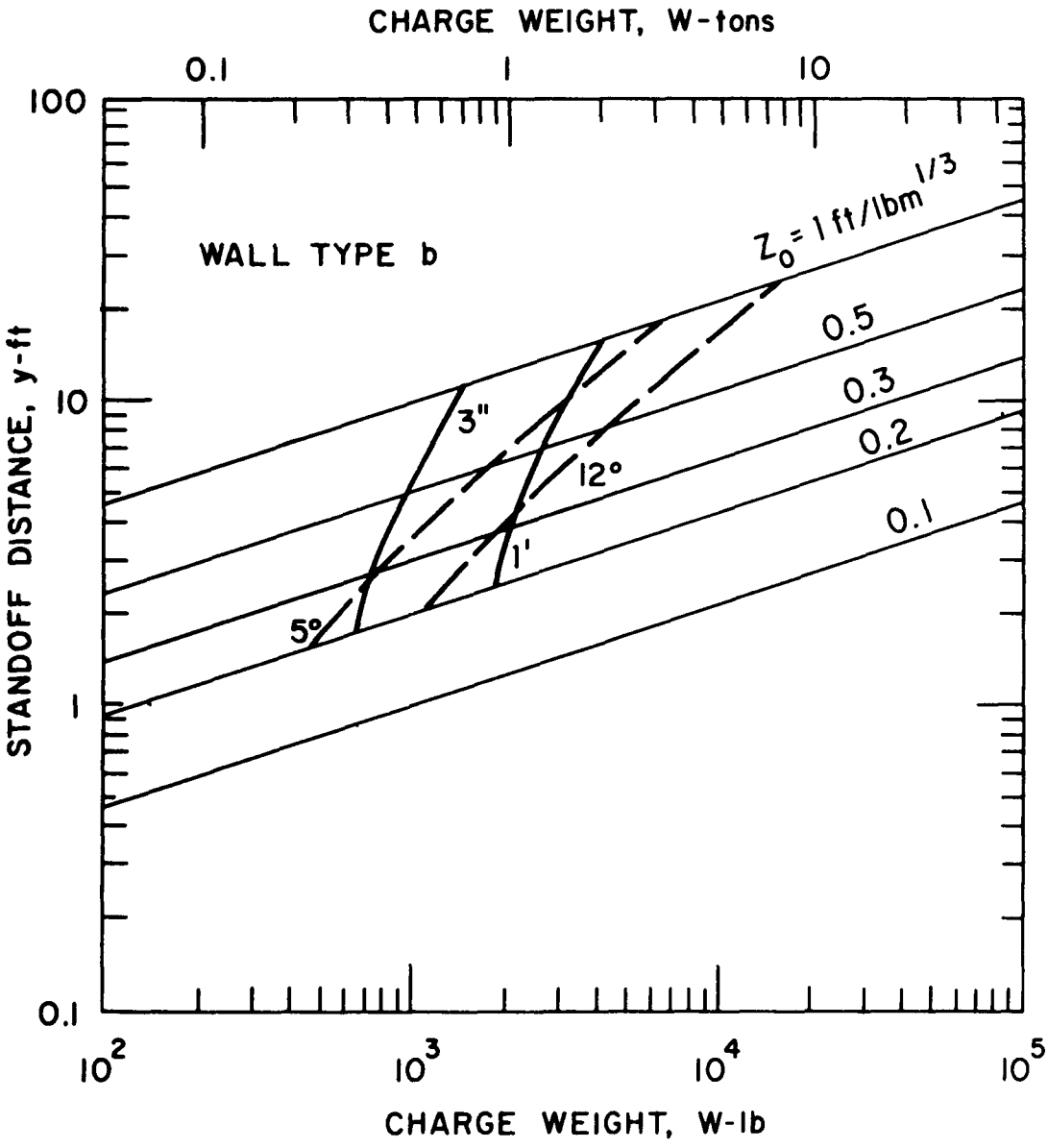

Fig. 11. Deflections and Deformation Criteria as a Function of Charge Parameters for Wall Type b

explosive charge weight, at any particular standoff distance, can easily vary over an order of magnitude depending which limits or allowable damage criteria are chosen. While fairly precise bounds exist for ultimate strength design of concrete structures [9] under ordinary conditions and static loadings no such criteria are available for the dynamic response of air blast loaded structures. At best one can arrive at some criteria based on the physical appearance of the structure at the end of the response phase. This is the basis for the above mentioned rotation limits. Similarly experimental evidence exist [2], that very severe wall damage, in the form of scabbing and disintegration of the concrete, is to be expected when the maximum deflections are as large as the wall thickness. In the absence of more precise information the above criteria may serve as guides for the setting of charge weight and standoff limits.

3.4 EFFECTS OF WALL CURVATURE

No simple techniques are available to estimate the structural response of curved concrete walls subjected to explosive air blast loading. For curved walls loaded on the convex side, as would be the case for nuclear power plant containments, the flat wall estimates should provide conservative answers. Here only the effect of wall curvature and of finite structural size (finite radius) on the blast loading and impulse will be examined. Subsequent response calculations are again carried out with the flat wall approximations using however the impulses for the curved structure.

The interaction of a spherical blast wave with a cylindrical structure results in a three-dimensional geometry and flow field. As the blast sweeps across the structure their line of intersection is distorted from the circular ring shape of the flat plate to a complex three-dimensional elliptic shape. An approximate numerical technique was developed to obtain

the impulse on the structure acting in a direction normal to the axis of the cylinder. The integration of impulse was performed in a grid network consisting of circles and longitudinal strips parallel to the cylinder axis. Again at each point the reflected impulse per unit area was determined by the procedure outlined in Section 2. Since the blast wave spreads beyond the width (diameter) of the cylinder appropriate cutoffs are introduced in the integration procedure for the total impulse. Fig. 12 shows the total impulse variation with scaled standoff distance over cylindrical structures with five different radii. Also shown is the total impulse on a flat wall. The length or height of the cylinder (wall) in all cases was the same 100 ft and the charge weight was 1000 lb. It can be seen that for large diameter structures the impulse differs little from the flat wall case. Due to the sharp reduction of projected area the total impulse is significantly reduced when the cylinder radius is small (5 ft).

Using the flat wall response analysis of section 3.2 but the impulses as properly computed for a curved structure one obtains the deflections and hinge line rotations shown respectively in Fig. 13 and Fig. 14. Again for large radii there is little deviation from the flat wall results, however for small cylinder radii the difference is substantial.

Based on these results it may be concluded, that the flat wall analysis while somewhat conservative will give reasonable estimates of wall response for typical nuclear power plant containment structures which in general have cylinder radii on the order of ten's of feet. On the other hand for structures with diameters of the order of a few feet, such as pipes, the flat wall computation of impulses is a gross overestimate and the proper numerical impulse evaluation should be used. An added benefit of using flat wall calculations for large diameter structures is that the results are scalable.

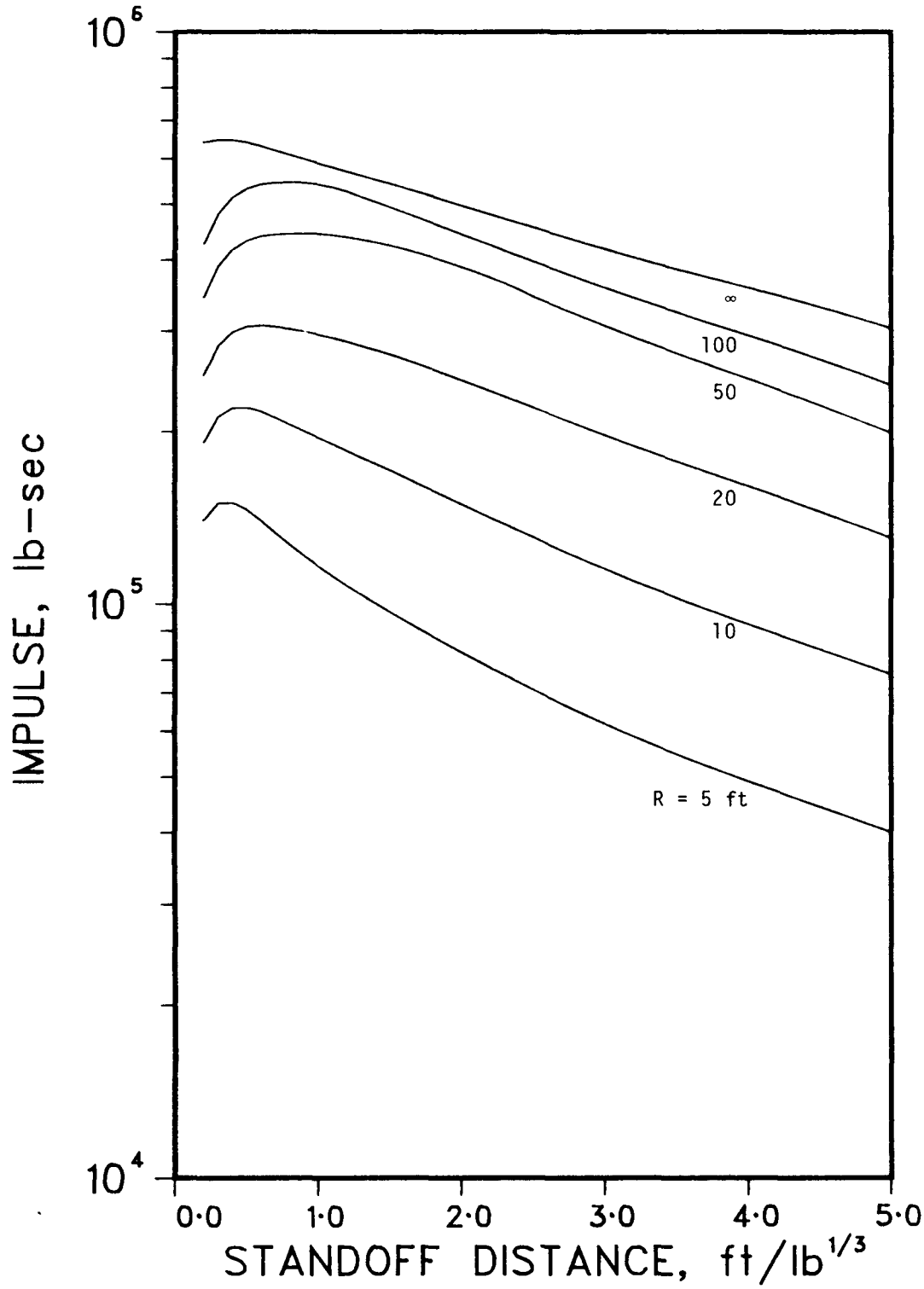

Fig. 12. Variation of Blast Impulse with Standoff for Different Cylinder Radii. (Cylinder Length L=100 ft, Charge Weight W = 10^3 lb)

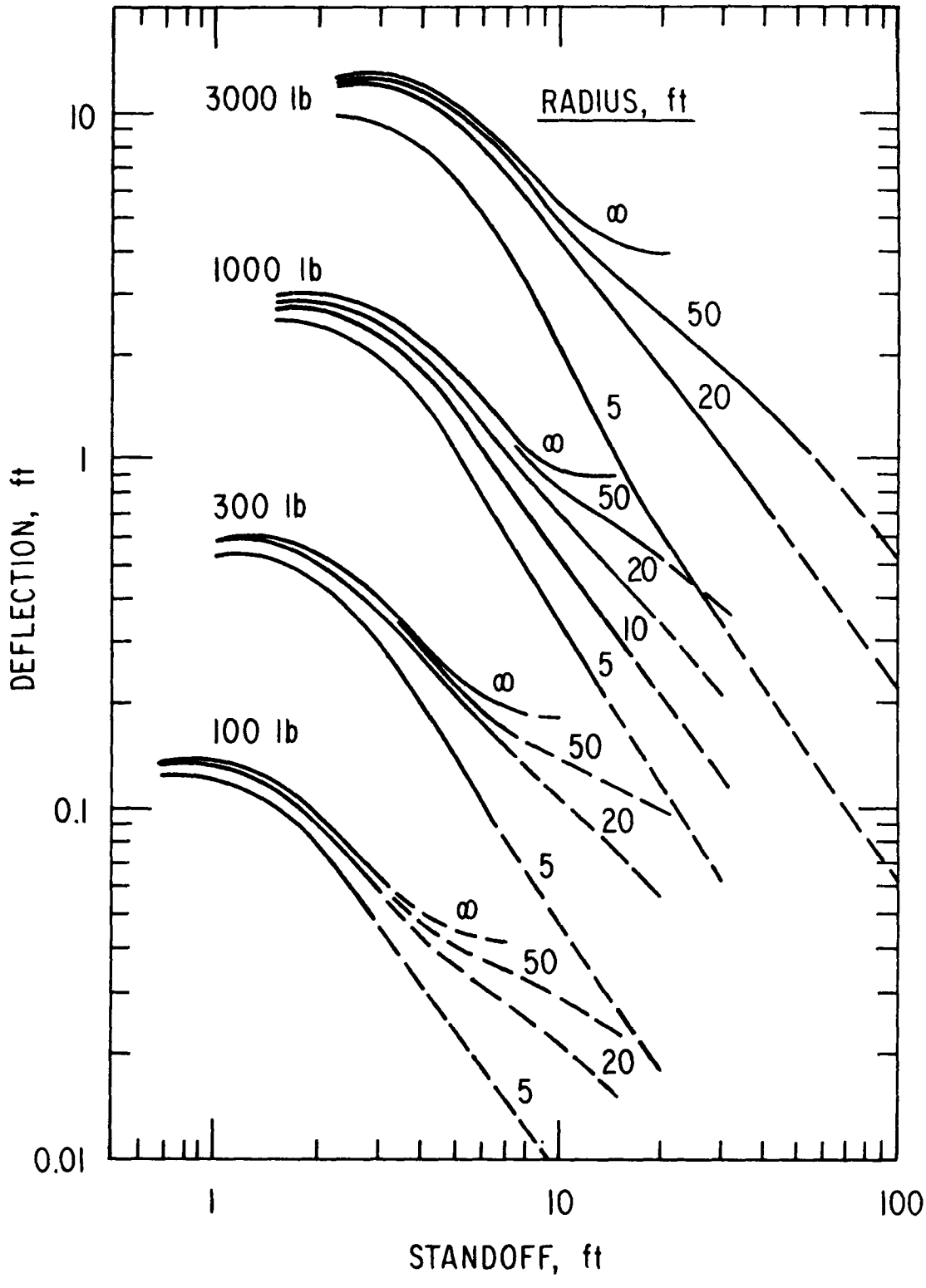

Fig. 13. Effect of Cylinder Radius on Wall Deflection for Various Charge Weights (Wall Type a)

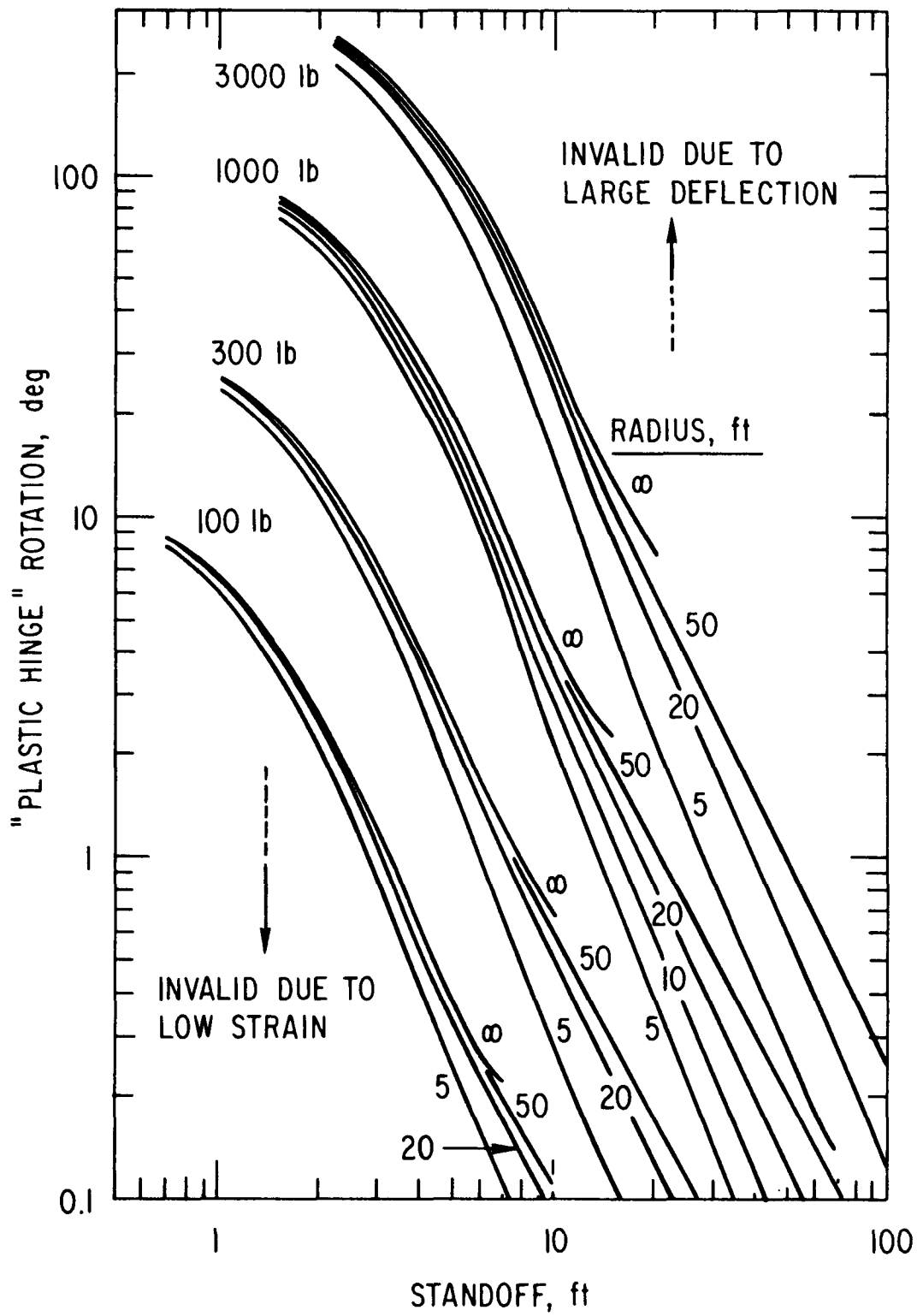

Fig. 14. Effect of Wall Curvature on Plastic Hinge Rotation for Various Charge Weights (Wall Type a)

The introduction of an additional length scale, i.e. the diameter of the structure, makes scaling of the impulse load on a cylinder impossible. Therefore loads on small diameter structures must be computed individually, i.e. for each charge weight and standoff.

4. SPALLING OF CONCRETE WALLS

It was indicated earlier that spalling may occur on the back face of a concrete wall which is subjected to air blast on its front phase. The phenomenon of spall in brittle materials occurs when strong tension waves are reflected into the wall from the free surface at the back face and interact with the decaying compression wave in such a way as to produce locally tension stresses which exceed the dynamic tensile rupture strength of the material. Since the process has been discussed at length elsewhere [5,10,11,12] only a brief outline of the assumptions and calculation procedures will be given here.

It is assumed that the wall material is linear-elastic and the spalling occurs instantaneously whenever the dynamic tensile ruptures strength is reached. The actual spherical wave interaction with the back face shown in Fig. 2 is approximated by plane wave theory, using both normal and oblique reflections, for which analytical solutions are possible.

To obtain the time history of the compression wave incident on the back face of the wall, it is assumed that the wave form remains similar to that of the air blast and that the peak pressure in the wall decays linearly with distance through the wall. This is consistent with a linear-elastic material behavior and constant wave speed as well as with the spherical divergence of the pressure wave. Hence for any angular position α (angle of incidence) the value of the peak compression arriving at the back face of the wall p_α is given in terms of the peak reflected pressure $p_{r\alpha}$ at the front face as:

$$p_\alpha = p_{r\alpha} \frac{r}{r + h/\cos\alpha} = p_{r\alpha} \frac{y}{y + h} \quad . \tag{20}$$

Here r is the radial distance from the point of burst to the wall at angle α, h is the wall thickness and y is the normal distance from the explosion point

to the wall ($y = r\cos\alpha$). Once p_α is determined the decay of the compression wave at the back face of the wall and angular position α is obtained by the assumption of wave similarity. For analytical estimates of wall spallation this pressure decay must be represented by a simple mathematical expression. We assume that the power law of Eq. (3) locally approximates the pressure decay with the variation of the exponent given in Fig. 5.

4.1 SPALL AT NORMAL INCIDENCE

The reflection of a plane compression wave from a free surface at normal incidence is a one-dimensional problem as shown in Fig. 15. Assuming that the material is linearly elastic with constant wave speed, the condition of a stress free boundary implies that a tension wave, equal in strength and wave shape to that of the compression wave, is reflected back into the wall as illustrated in Fig. 15 (a). The actual state of stress of any location is then the algebraic sum of the two stress waves (compression and tension). Whenever this net stress σ_N at the head of the reflected tensile wave equals the dynamic tensile rupture strength σ_T of the material, spallation will occur as illustrated in Fig. 15 (b). Designating all stress values as positive quantities, p for compression and σ for tension, one can write for the first spall

$$\sigma_T = \sigma_{N1} = \sigma_o - p_1(t_1) = p_o - p_1(t_1). \tag{21}$$

Here the subscripts o refer to the peak initial value of stress in the wave and p_1 is the stress in the compression wave at the location of the first spall. Considering the symmetry of the waves and the constant wave speed it can be easily demonstrated that time t_1, which corresponds to pressure p_1 in the compression wave, is given by

$$t_1 = \frac{2\delta_1}{c} \quad , \tag{22}$$

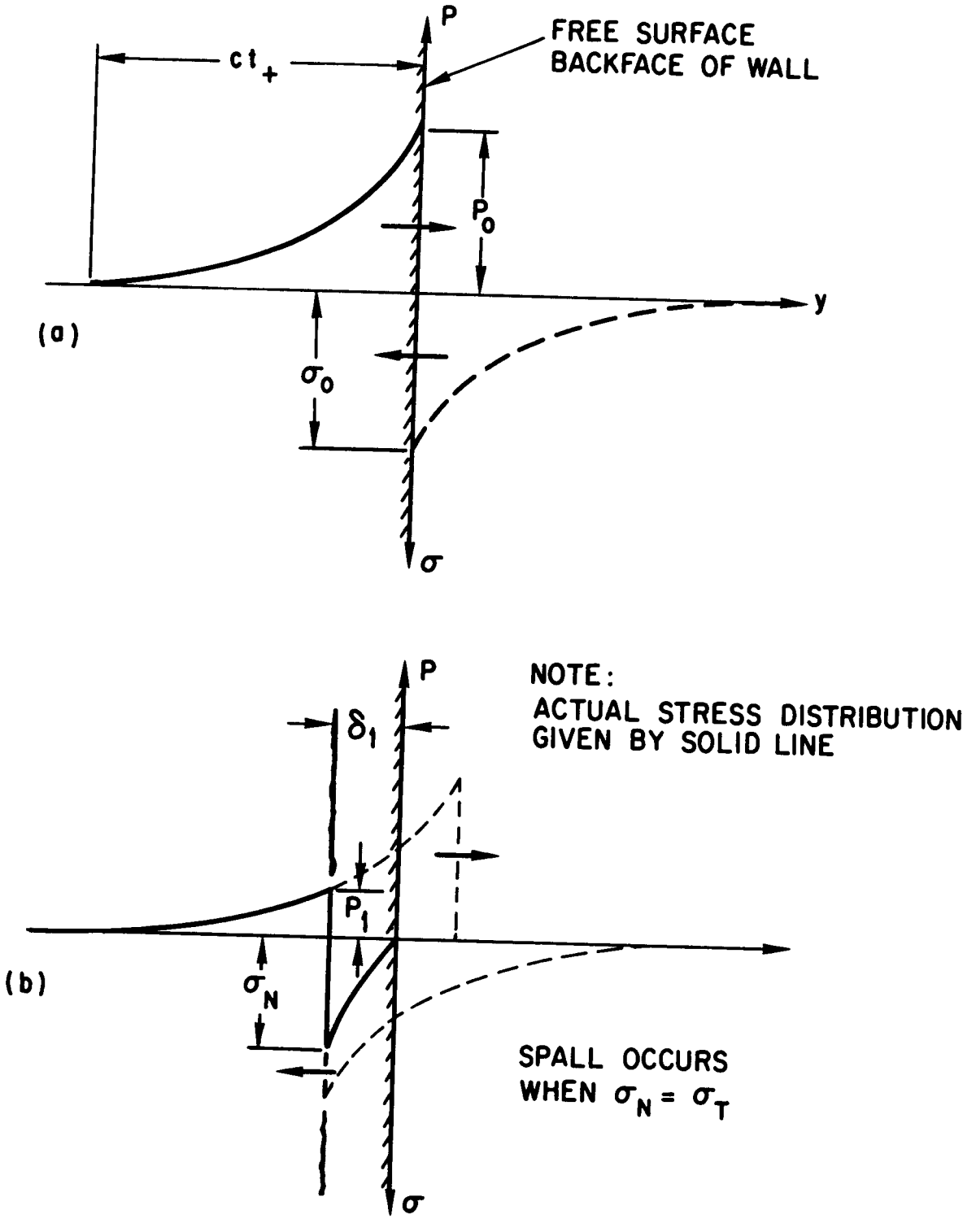

Fig. 15. Spalling at Normal Incidence

where δ_1 is the thickness or depth of the first spall and c is the wave speed.

If the initial peak compression is much larger than the tensile rupture strength σ_T and the wave form is decaying with time then it is possible to obtain multiple spalls. In fact, the theoretical number of spalls n is given as

$$n \leq \frac{p_o}{\sigma_T} \quad . \tag{23}$$

Since a new free surface is generated every time a spall appears, the reasoning applied to the first spall can be extended to all spalls. Thus, Eq. (21) can be generalized for an arbitrary spall k as follows:

$$\sigma_T = \sigma_{Nk} = p_{k-1}(t_{k-1}) - p_k(t_k) \quad . \tag{24}$$

Here p_k is the value of the compression wave when the k's spall occurs and p_{k-1} is the value corresponding to that for the preceding spall. Again considering wave symmetry and constant wave speed the time t_k along the wave form corresponding to stress p_k can be simply obtained.

$$t_k = \frac{2(\delta_1 + \delta_2 + \ldots + \delta_{k-1} + \delta_k)}{c} \tag{25}$$

From the above it can be seen that the thickness of the spalls depend strongly on the wave form of the compression wave.

The velocity of the spall layers for this simple one-dimensional case is obtained by equating the momentum of the spall layer to the portion of the impulse imparted to it by the compression wave and still trapped in it at the time of spall. Expressing all quantities per unit area one can write for the first spall

$$i_1 = \int_o^{t_1} p(t)dt = \rho_w \delta_1 u_1 \tag{26}$$

where i_1 is the trapped impulse, ρ_w the density of the wall material and u_1 the velocity of the first spall layer. By simple analogy, the velocity u_k for any arbitrary spall k can be obtained from:

$$i_k = \int_{t_{k-1}}^{t_k} p(t)dt = \rho_w \delta_k u_k \quad . \tag{27}$$

Again, the strong dependence of spall velocity on the form of the compression wave can be readily discerned.

To derive specific expressions for spall thickness and velocity, the wave form approximation given by Eq. (3) must now be employed. Substituting into Eq. (21) and using Eq. (22) yields the following relationship for the first spall depth

$$\delta_1 = \frac{ct_+}{2}\left(\frac{\sigma_T}{p_o}\right)^{1/\gamma} \quad . \tag{28}$$

A general relationship is derived for the k-th spall by using Eqs. (24) and (25) together with expression (3). After simplification one obtains

$$\delta_k = \frac{ct_+}{2}\left\{\left(\frac{k\sigma_T}{p_o}\right)^{1/\gamma} - \left[\frac{(k-1)\sigma_T}{p_o}\right]^{1/\gamma}\right\} = \frac{ct_+}{2}\left(\frac{\sigma_T}{p_o}\right)^{1/\gamma}\left[k^{1/\gamma} - (k-1)^{1/\gamma}\right] . \tag{29}$$

The spall velocities obtain from the impulse expressions. Eq. (8) can be integrated using (3). Substitution of Eqs. (22) and (28) and subsequent simplification yields the velocity of the first spall

$$u_1 = \frac{2p_o}{c\rho_w}\left[1 - \frac{1}{\gamma+1}\,\frac{\sigma_T}{p_o}\right] \quad . \tag{30}$$

The same procedure can be applied to any spall and after much simplification one obtains for the velocity of the k-th spall

$$u_k = \frac{2p_o}{c\rho_w}\left\{1 - \frac{1}{\gamma+1}\,\frac{\sigma_T}{p_o}\left[k + \frac{1}{\left(\frac{k}{k-1}\right)^{1/\gamma} - 1}\right]\right\} . \tag{31}$$

It is interesting to note that the spall velocities do not depend explicitly on the blast wave duration t_+ and thus the explosive weight.

4.2 SPALL AT OBLIQUE INCIDENCE

When a plane compression wave in an elastic medium strikes a free surface obliquely the reflection process becomes considerably more complex than in the case of normal incidence. To maintain a stress free boundary at the surface two waves must be reflected back into the material, namely a dilatational wave and a shear wave [13]. A typical reflection process of this type is illustrated in Fig. 16. For linear-elastic media the reflection angle for the dilatational wave must be equal to α the angle of incidence because its wave speed is equal to that of the incident wave. However, the shear wave having a different wave speed c', reflects at a different angle β in order to stay in contact with the point of wave incidence as it moves across the surface. The relationship between these angles, wave speeds, and the Poisson's ratio ν of the material can be obtained from Snell's law [13] and is written as

$$\frac{\sin \alpha}{\sin \beta} = \frac{c}{c'} = \left[\frac{2(1 - \nu)}{1 - 2\nu}\right]^{1/2} \tag{32}$$

Concerning the strengths of the reflected waves, these are obtained from the condition that the sum of the resultant stresses normal to the surface must be zero. Using a reflection coefficient η_R it can be shown [5,12] that the following relationships hold.

$$\sigma_R = \eta_R \sigma_I \tag{33}$$

$$\tau_R = [(\eta_R + 1)\cot 2\beta] \frac{c}{c'} \sigma_I \tag{34}$$

$$\eta_R = \frac{\tan \beta \tan^2 2\beta - \tan \alpha}{\tan \beta \tan^2 2\beta + \tan \alpha} \tag{35}$$

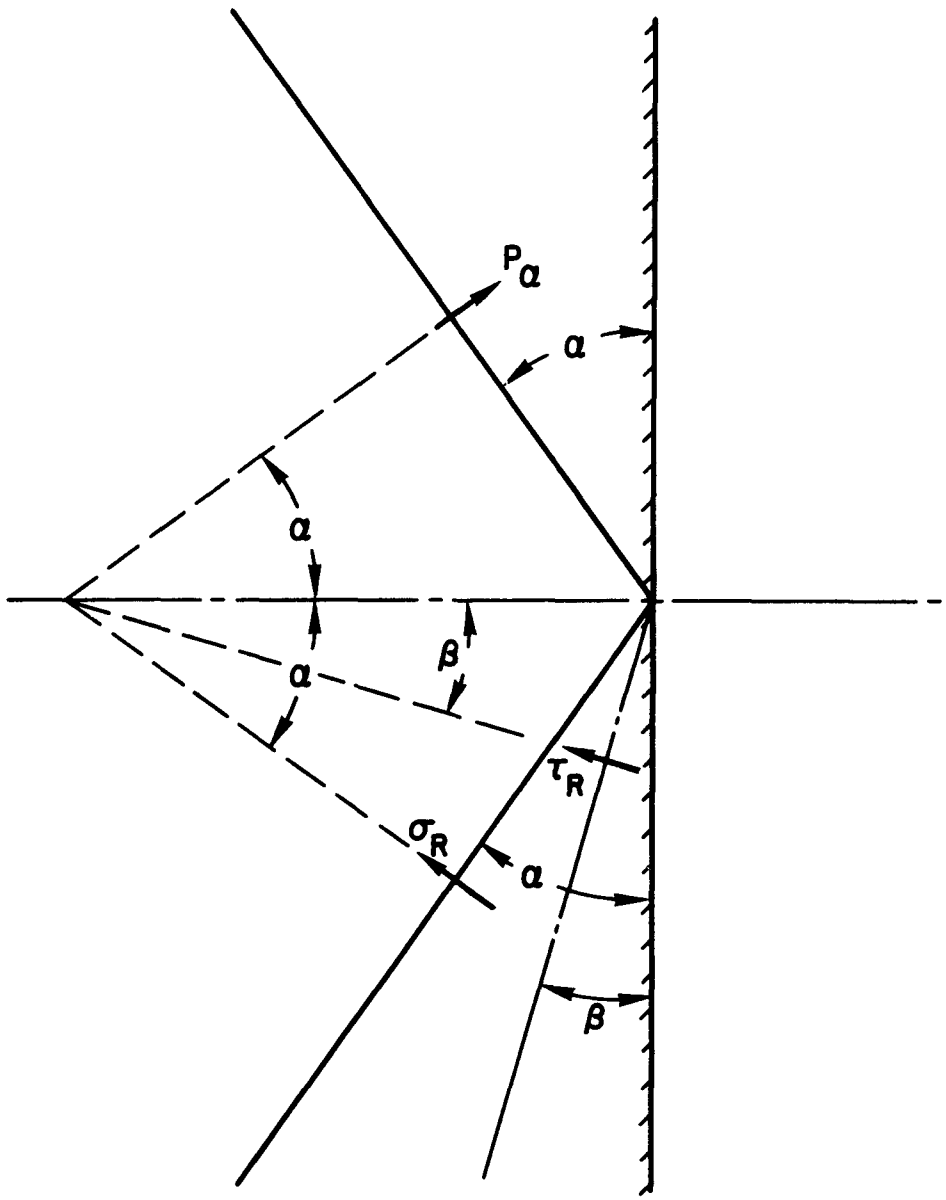

P_α - INCIDENT COMPRESSION WAVE

σ_R - REFLECTED DILATATIONAL WAVE

τ_R - REFLECTED SHEAR WAVE

Fig. 16. Interaction of an Oblique Compression Wave with a Free Surface

Here σ_I is the amplitude of the incident dilatation wave and σ_R and τ_R are the amplitudes of the reflected dilatational and shear wave respectively.

For physically acceptable values of ν the dilatational wave speed is always larger than the shear wave speed and thus angle β is smaller than angle α. The above equations also indicate that the reflection process is independent of the amplitude of the incident wave and is only a function of material properties and the angle of incidence. Using typical material properties for concrete, i.e., $\nu = 0.15$ and $c = 10^4$ fps values of the angle β, and the reflection coefficient η_R waves are obtained (Fig. 17). It is interesting to note that the reflection factor η_R (Fig. 17b) changes sign twice as the angle of incidence varies from zero to 90 degrees. Since such a sign change implies a phase reversal of the reflected dilatational wave, no spalling should be expected in concrete for angles of incidence larger than 45°.

The geometry of a typical oblique spall is shown in Fig. 18. Also shown are the profiles of the compression and reflected tension wave. Introducing again the pressure notation p (positive quantities) for the stress in the incident compression wave and letting η be the absolute value of the reflection coefficient η_R one can write for the first spall

$$\sigma_T = \sigma_R - p_1(t_1) = \eta p_\alpha - p_1(t_1) \tag{36}$$

where the second expression obtains from (33) together with the identity $\eta_R \sigma_I = \eta p_\alpha$. The thickness of the spall δ_1 is now related to the t_1 (when the pressure is p_1) by the following modified equation:

$$t_1 = \frac{2\delta_1 \cos \alpha}{c} \quad . \tag{37}$$

For strong compression waves multiple spalls are again possible. Their theoretical total number n can be estimated from the following expression [5]

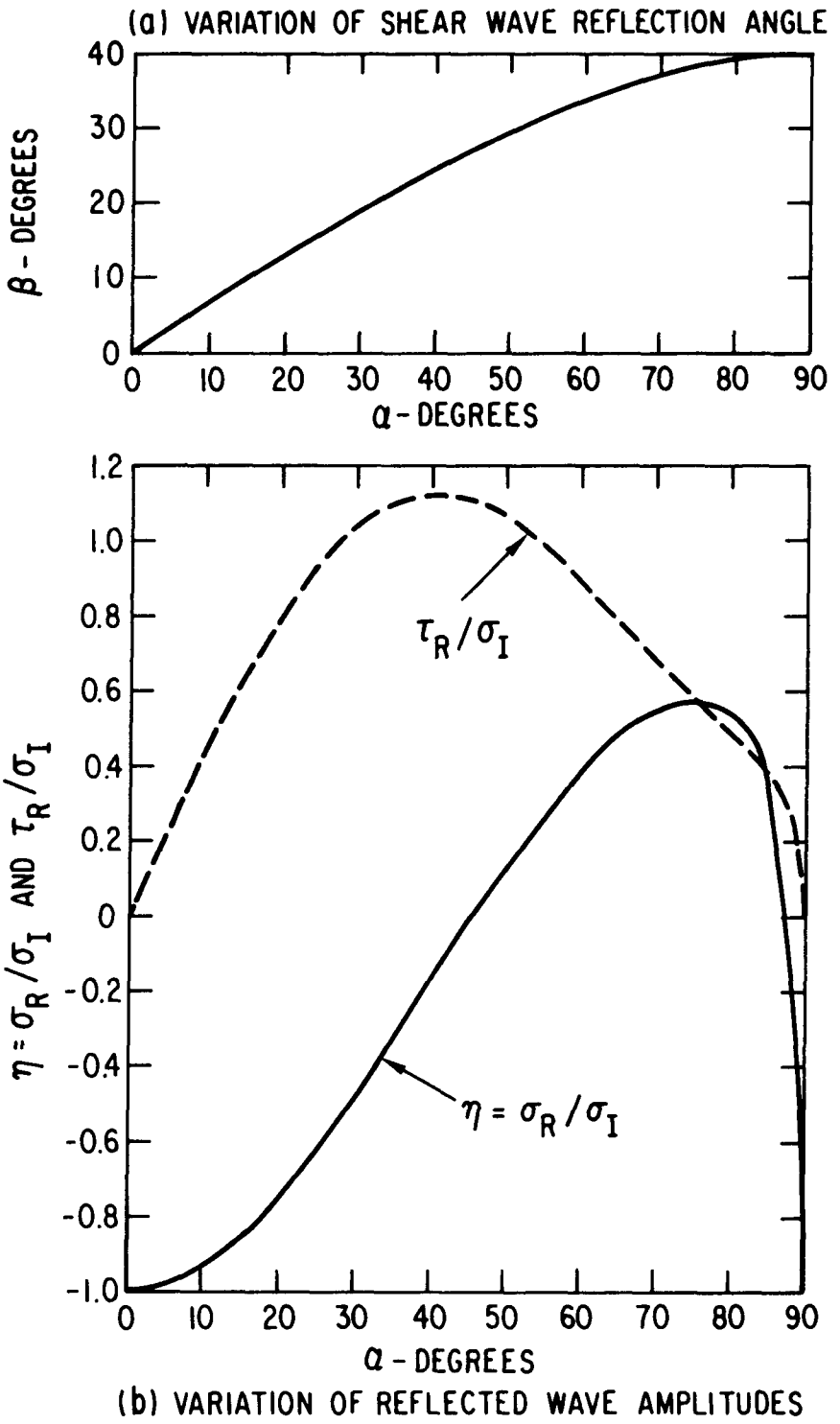

Fig. 17. Free Surface Reflection Parameters for Oblique Dilational Wave (Poisson's Ratio = 0.15)

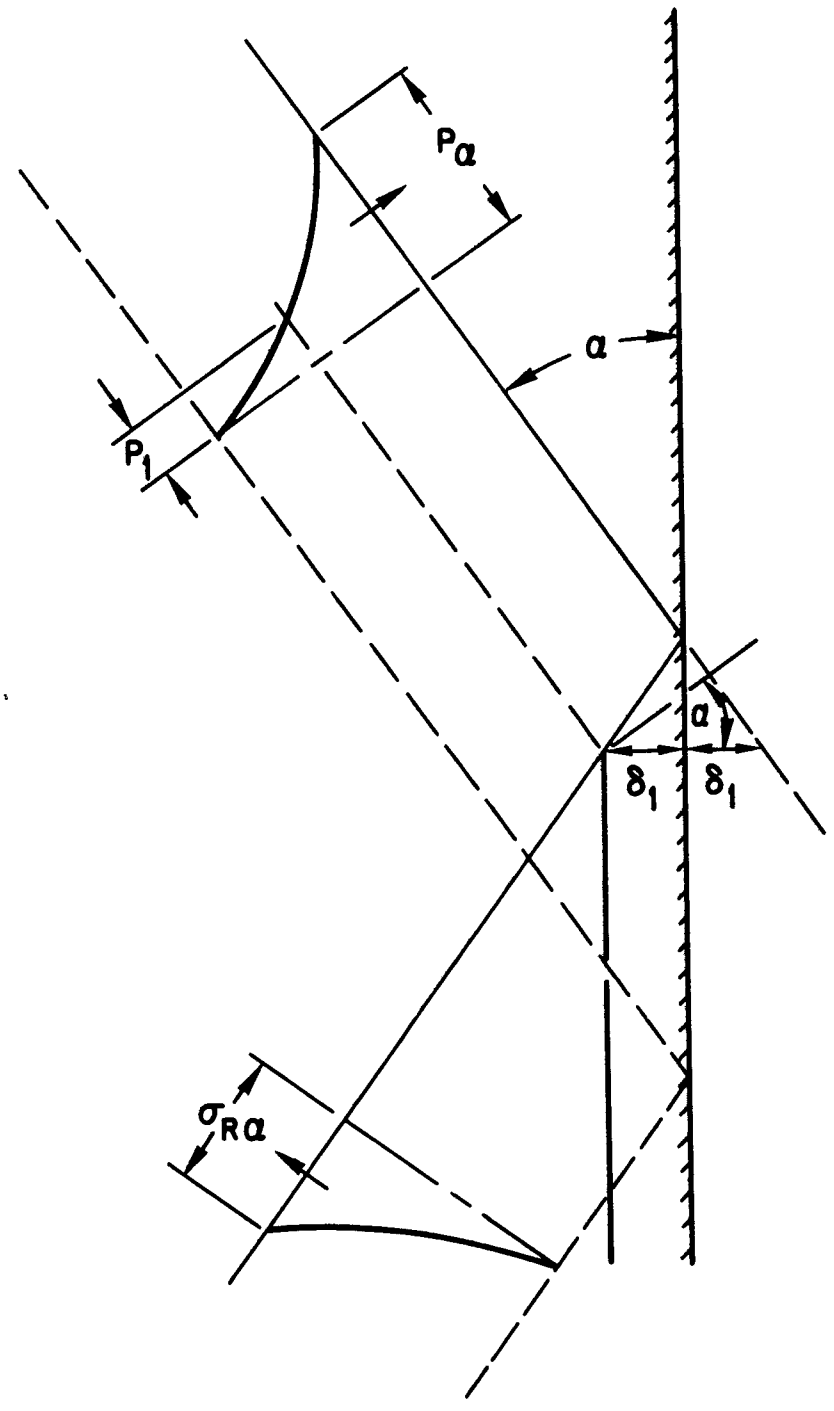

Fig. 18. Spalling at Oblique Incidence

$$n \leq - \frac{\ell n \left[(1 - \eta) \frac{p_\alpha}{\alpha_T} + 1 \right]}{\ell n \eta} \quad . \tag{38}$$

For an arbitrary spall k the relations giving spall depth are:

$$\sigma_T = \eta p_{k-1}(t_{k-1}) - p_k(t_k) = \eta^k p_\alpha - \sigma_T \eta \left(\frac{1 - \eta^k}{1 - \eta} \right) - p_k(t_k) \tag{39}$$

and

$$t_k = \frac{2(\delta_1 + \delta_2 + ... + \delta_{k-1} + \delta_k)\cos \alpha}{c} \quad . \tag{40}$$

Spall velocities are again obtainable from the impulse integral. However, since that impulse is acting in the direction of the incident wave, the velocity will also be in this direction and the impulse is trapped in a length given by $\delta/\cos\alpha$. Thus for the first spall the relationship is

$$\rho_w u_1 \frac{\delta_1}{\cos \alpha} = \int_o^{t_1} p(t)dt \quad . \tag{41}$$

For an arbitrary spall k one obtains

$$\rho_w u_k \frac{\delta_k}{\cos \alpha} = \int_{t_{k-1}}^{t_k} p(t)dt \quad . \tag{42}$$

Applying the approximate wave form, given by Eq. (3), to the above relationships one obtains specific expressions for spall thicknesses and velocities.

Thickness of 1st spall

$$\delta_1 = \frac{ct_+}{2 \cos \alpha} \left(1 - \eta + \frac{\sigma_T}{p_\alpha} \right)^{1/\gamma} \tag{43}$$

Thickness of k-th spall

$$\delta_k = \frac{ct_+}{2 \cos \alpha} \left\{ \left[(1 - \eta^k)^{1/\gamma} - (1 - \eta^{k-1})^{1/\gamma} \right] \left[1 + \frac{1}{1 - \eta} \frac{\sigma_T}{p_\alpha} \right]^{1/\gamma} \right\} \tag{44}$$

Velocity of 1st spall

$$u_1 = \frac{2p_\alpha}{(\gamma + 1)c\rho_w} \cos^2\alpha \left[(\gamma + \eta) - \frac{\sigma_T}{p_\alpha}\right] \tag{46}$$

Velocity of k^{th} spall

$$u_k = \frac{2p_\alpha \cos^2\alpha}{(\gamma + 1)c\rho_w} \left\{(\gamma + \eta^k) - \left(\frac{1 - \eta^k}{1 - \eta}\right)\frac{\sigma_T}{p_\alpha} - \frac{\left(1 - \eta + \frac{\sigma_T}{p_\alpha}\right)\eta^{k-1}}{\left(\frac{1 - \eta^k}{1 - \eta^{k-1}}\right)^{1/\gamma} - 1}\right\} \tag{47}$$

4.3 SPALL CALCULATIONS AND RESULTS

With the relationships derived above it is possible to calculate the spall variables in any given situation. The required inputs are the charge weight, wall thickness, and charge standoff distance. The spall parameters at any arbitrary incidence angle may then be readily obtained. Since the detailed procedure has been outlined before [5] only representative results which concern the most salient features of spalling will be given here. These results will be used to indicate trends rather than provide detailed information for all possible ranges of spalling.

Evidence exists [10] that the dynamic tensile rupture strength of brittle materials is substantially higher than the static value. In recent experiments with concrete [14], values in excess of 2000 psi were measured. This information was used to generate the computational results presented here. The other required physical parameters are typical for the quality of concrete used in nuclear power plant structures. In summary the values used in the computations are:

Compressive Strength	$f_c = 4000$ psi
Dilatational Wave Speed	$c = 10^4$ ft/s
Poisson's Ratio	$\nu = 0.15$
Dynamic Tensile Rupture Strength	$\sigma_T = 2000$ psi

Since all of the blast wave parameters including the positive overpressure phase duration t_+ can be scaled [2], the spall results would also be scalable except for the finite wall thickness h which affects the compression wave attenuation (see Eq. (20)). However, by using the expedient of a scaled wall thickness [5] it is possible to present the results in a more compact form. Thus all length dimensions will be scaled with the cube root of the explosive charge weight ($W^{1/3}$).

Fig. 19 presents spall thickness (depth) and velocity at normal shock incidence ($\alpha = 0$), as a function of charge standoff distance with spall number as a parameter as indicated in the figure. The results are for a wall of zero thickness, i.e. no attenuation of shock wave in the wall is assumed to take place. The spall depth increases with spall number but the spall velocity shows an opposite trend. Thus the first spall has the highest velocity while its thickness is a minimum. Spall thickness also increases with standoff distance but again the spall velocity decreases. These trends reflect the dependence of spall thickness on the profile of the compression wave which is steepest at the shock front and flattens out as the pressure decays. Similarly, the wave forms become less steep as the peak pressure decays, i.e., the standoff distance increases.

The most notable aspect of the results is that high spall velocities (100-500 ft/s) are associated only with very thin spall layers. Even for charges of 10^4 lb the corresponding spalls are less than one quarter inch thick. On the other hand for substantial spall layers ($\geq$ 1 in.) the velocities are quite low (about 15 ft/s). Because of this in the case of normal incidence, the kinetic energy per unit area of spall does not vary appreciably over the entire range of blast parameters considered. Similarly the total depth of spall, i.e., the sum of all spall layer thicknesses, is nearly

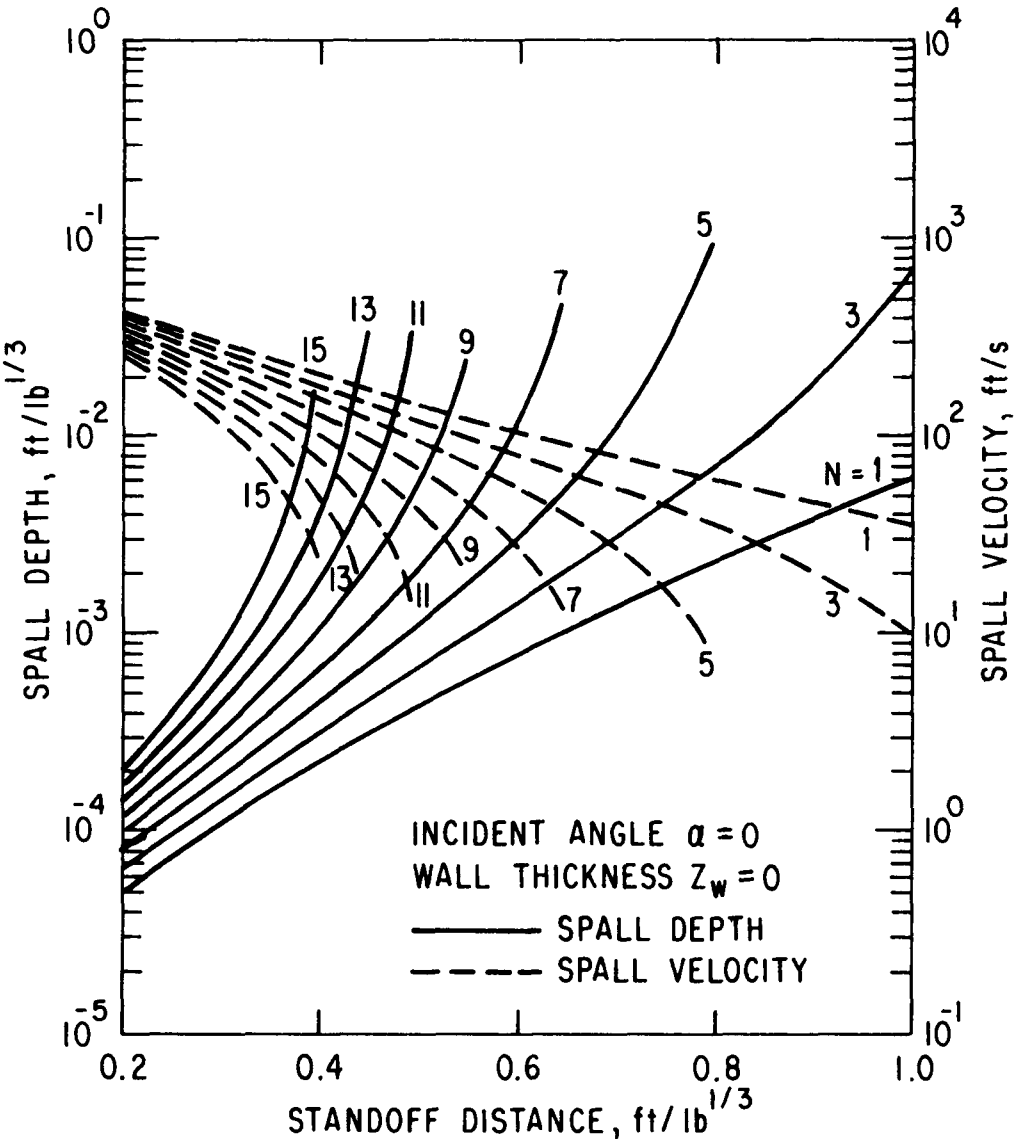

Fig. 19. Variation of Spall Depth and Velocity with Standoff Distance and Spall Number

constant, being on the order of 0.25 ft/lb$^{1/3}$. This is not an unexpected result. It can be shown [5] that the total depth of spall D is approximately equal to one half the wave length of the compression wave, i.e., $D \triangleq ct_+/2$, and this quantity is remarkably constant in the pressure range of interest. For reinforced concrete walls spalling is expected to be limited to the concrete layer covering the reinforcement, since this layer is thinner than the predicted total spalling depth.

Fig. 20 again gives spall depth and velocity information but as a function of spall number with scaled standoff distance as a parameter. This is a clearer illustration of the spall number cut-off at various standoff distances, e.g., for the assumed dynamic tensile rupture strength of 2000 psi, 33 spalls may occur at a standoff of 0.2 ft/lb$^{1/3}$ while only 3 spalls will be possible at a standoff of 1.0 ft/lb$^{1/3}$. It should be obvious, that due to the discrete nature of spalling, the spall number cut-off is not a continuous function of standoff but proceeds in steps.

The effect of wall thickness on spall velocity and depth is illustrated in Fig. 21, where results are given for the first spall variables at normal incidence as a function of scaled charge standoff distance with scaled wall thickness as parameter. For fixed charge weight and distance the spall thickness increases with increasing wall thickness while the spall velocity decreases. Similar results are obtained for subsequent spalls. Typically for a 10^3 lb charge at 3 ft standoff a wall thickness of 3 ft will result in a threefold increase in spall thickness relative to zero wall thickness and a twofold decrease in spall velocity. For larger standoff distances the effect becomes less pronounced.

A very strong effect on spall thickness and velocity is produced by variations in angle of shock incidence α. This is illustrated in Fig. 22

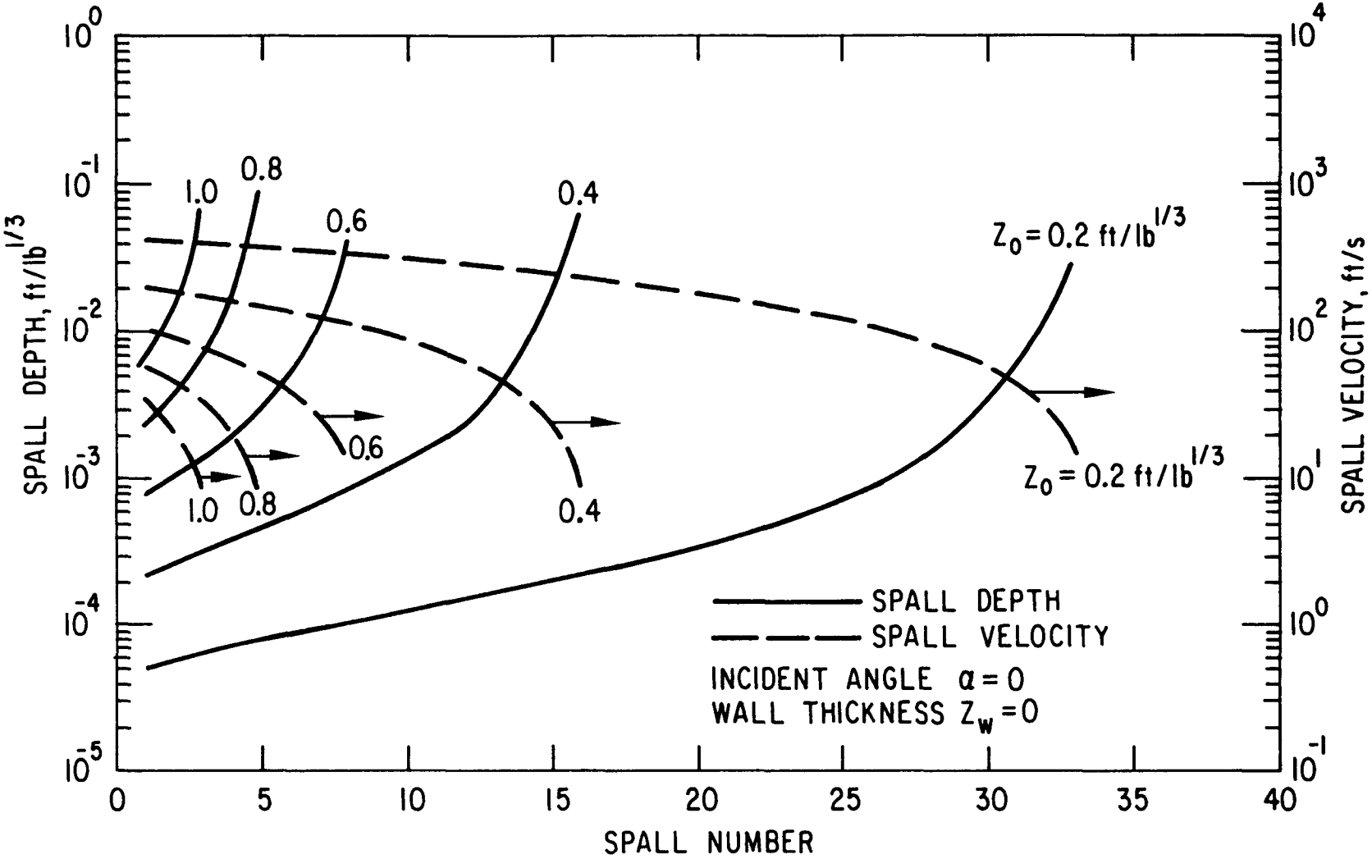

Fig. 20. Variation of Spall Depth and Velocity with Spall Number at Various Standoff Distances

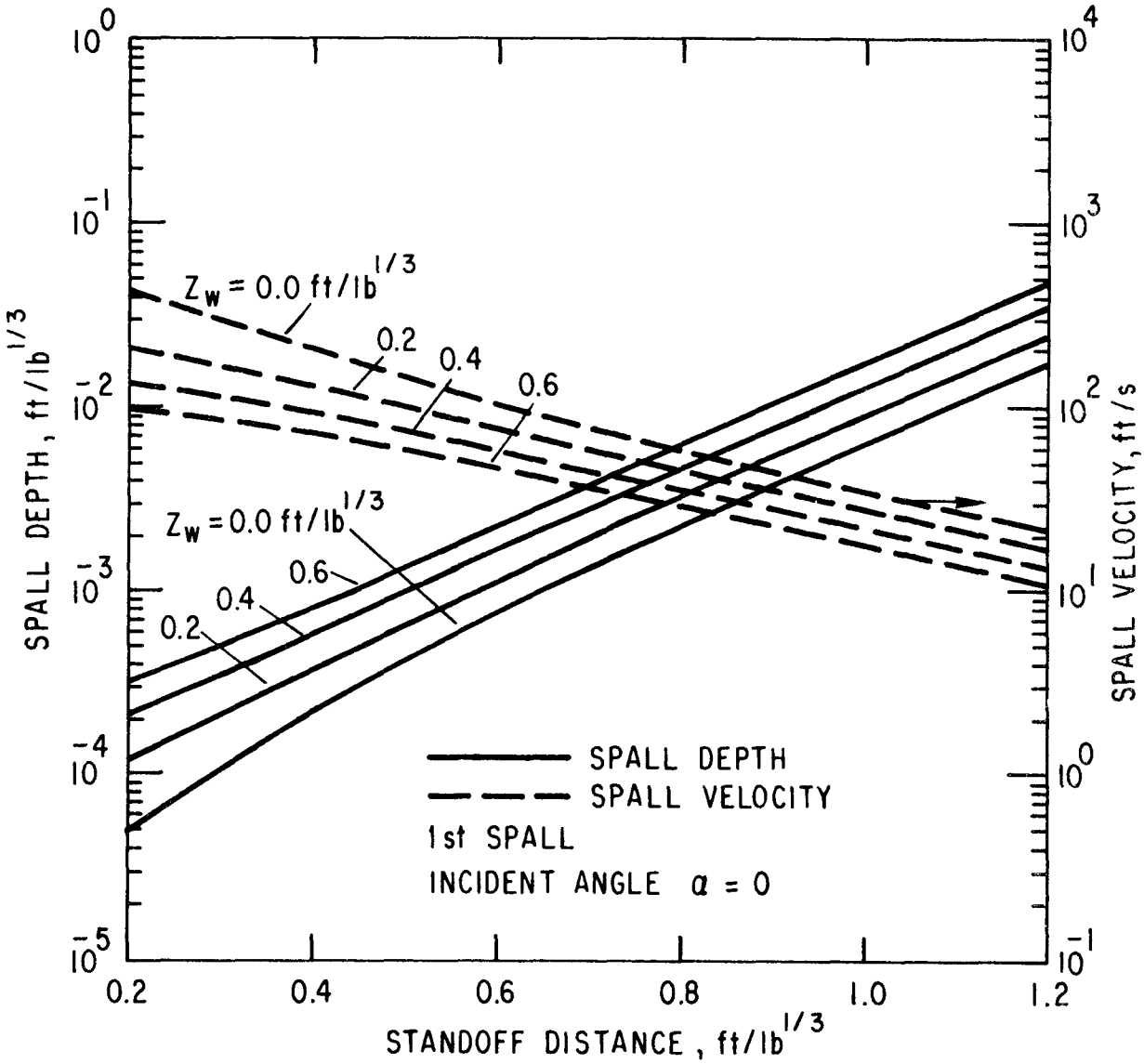

Fig. 21. Effect of Concrete Wall Thickness on Spall Depth and Velocity

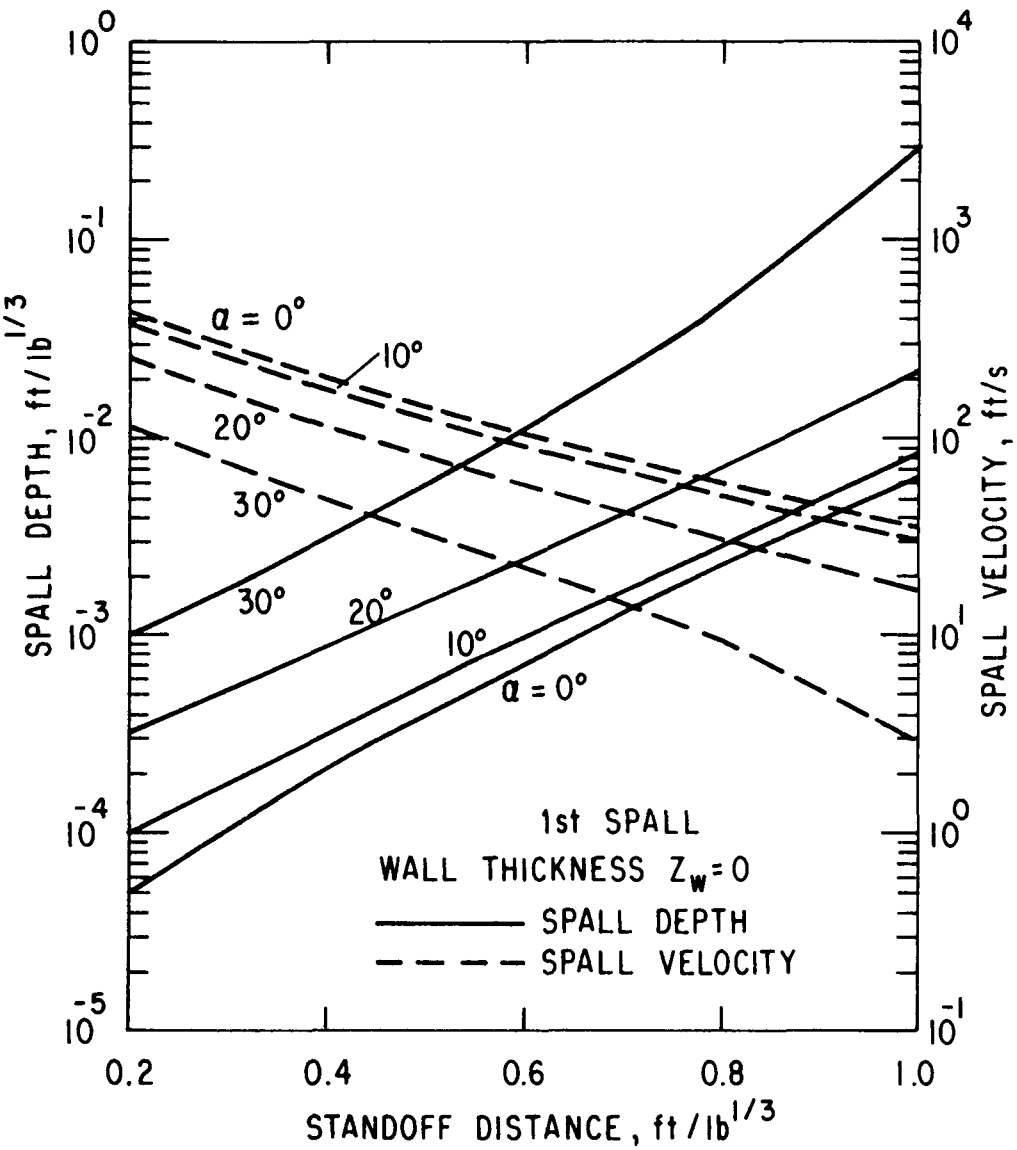

Fig. 22. Effect of Angle of Incidence on Spall Depth and Velocity

which gives the spall variables for the first spall as a function of scaled standoff distance for various values of the angle of incidence α. Again the case of zero wall thickness or no shock attenuation by the wall is presented. As indicated earlier no spalls occur beyond $\alpha = 45°$ because the reflection factor changes phase at this point (see Fig. 17). For a given standoff distance the spall thickness increases with angle of incidence while the velocity decreases. Relative to normal incidence the spall thickness for the oblique case is increased by the factor $1/\cos\alpha$ as well as by the effect of the reflection coefficient. The velocity is decreased by $\cos^2\alpha$ and again by a reflection coefficient effect. In computing the kinetic energy per unit area for oblique incidence, values substantially higher than those for normal incidence are encountered. The maximum in kinetic energy, for all standoff distances considered, occurs at an angle of incidence of about 20°.

The formation of a typical spall crater as calculated by the plane wave theory is shown in Fig. 23. Scaled variables are used in the illustration with both the charge standoff and wall thickness being 0.2 $ft/lb^{1/3}$. The jaggedness of the crater profile is due primarily to the fact that spall depth is computed discretely at a finite number of incidence angles α neglecting all interactions in angular direction between adjacent layers. This is a severe limitation of the plane wave theory. However, the results appear to give a reasonable qualitative picture of crater formation.

A comparison of the maximum spall velocities (first spall, normal incidence) with the maximum wall velocities induced by the total impulse of the blast is shown in Fig. 24. The latter velocities are obtained by considering the gross motion of the entire loaded portion of the wall and are calculated by the yield line analysis procedures outlined in Section 3. The results are given in scaled form as a function of charge standoff distance for a number of wall thicknesses. It is seen that except for the thickest wall (Z_w = 0.6 $ft/lbm^{1/3}$)

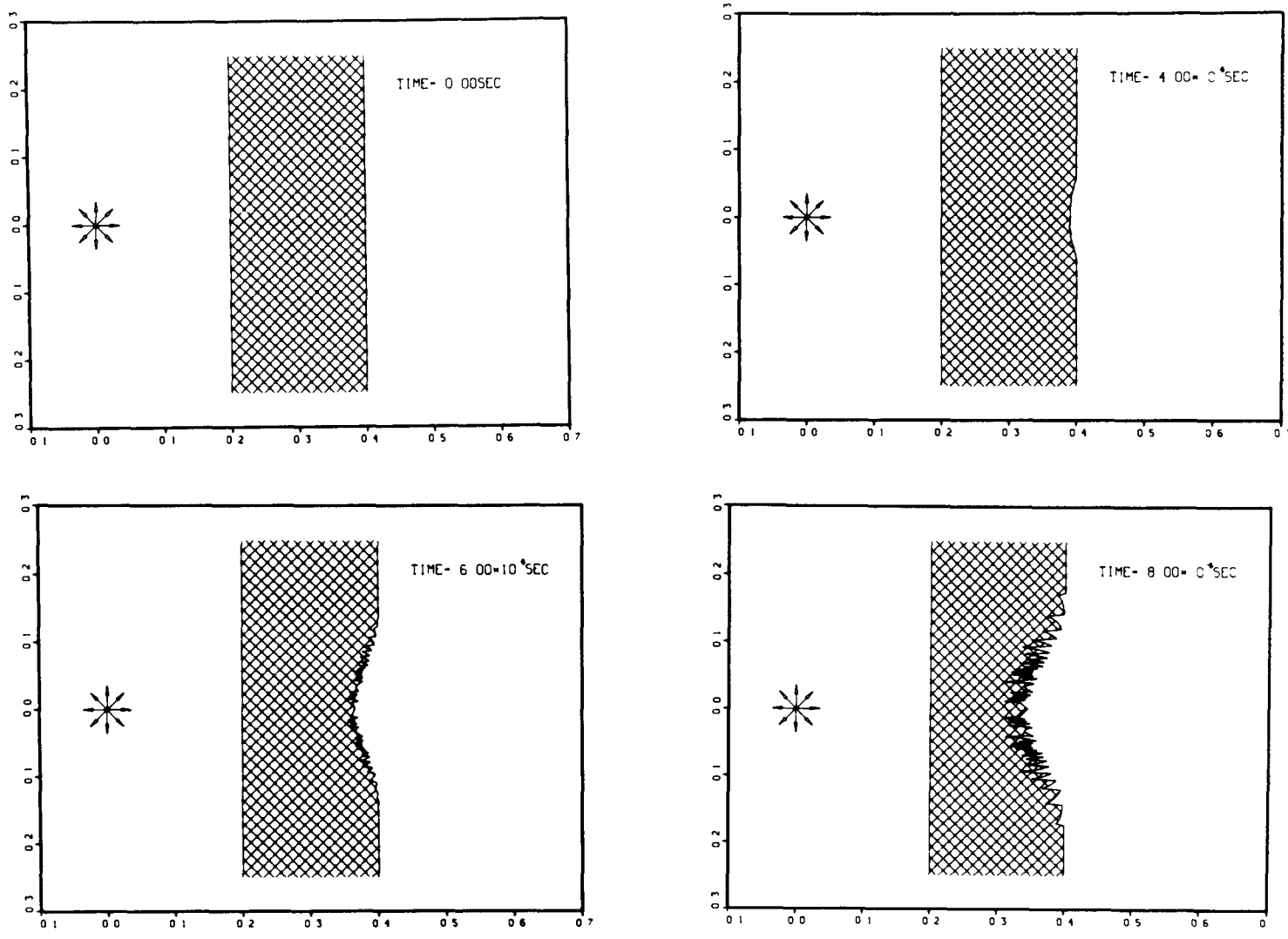

Fig. 23. Formation of a Typical Spall Crater

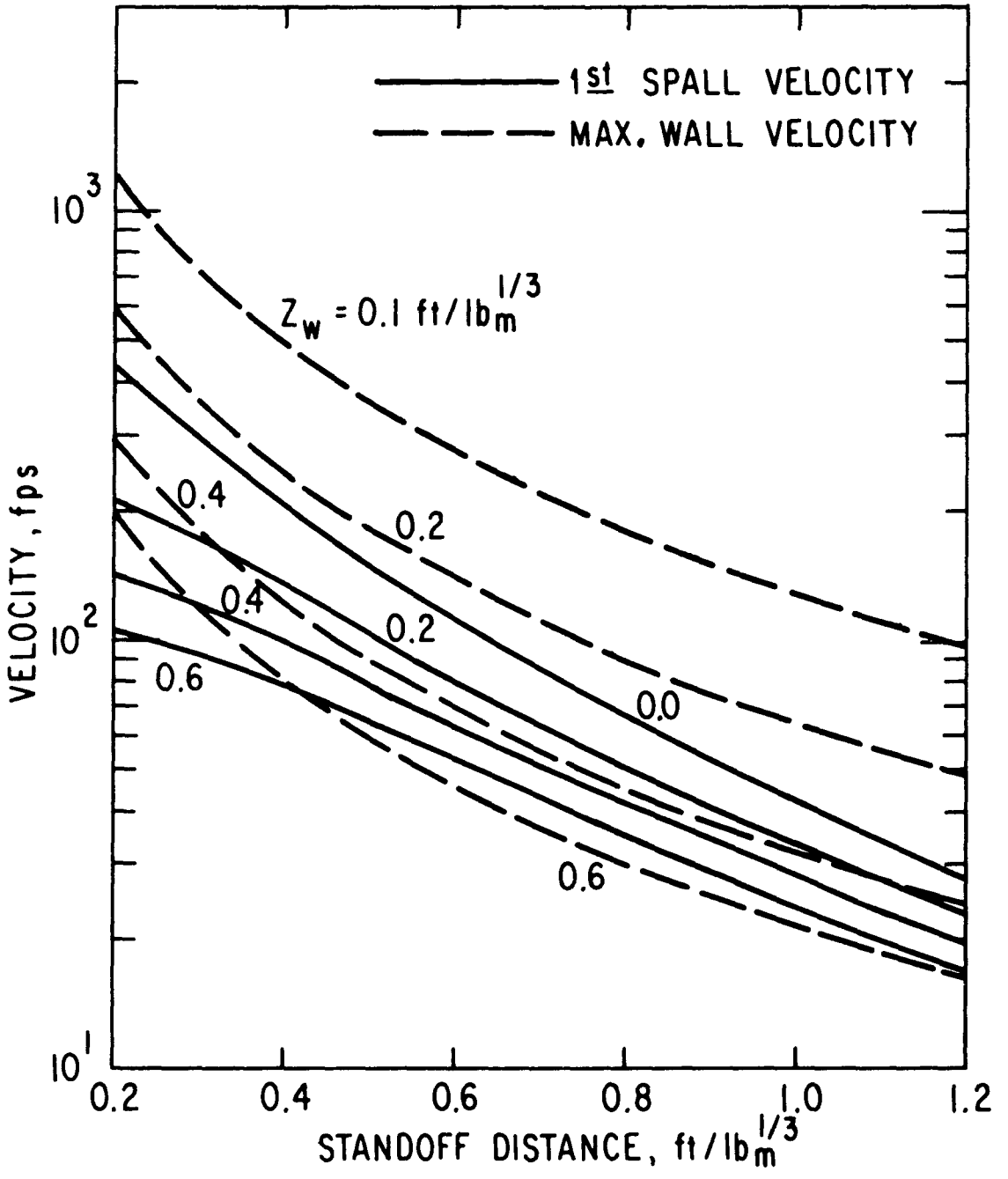

Fig. 24. Comparison of Maximum Spall and Wall Displacement Velocities

the velocities induced by impulse loading are substantially higher than those produced by direct spalling. A similar behavior is observed at other angular positions. Hence coupling between the two motions can be expected. The impulse motion is a late time effect and a number of stress wave reflections will occur before this motion commences. Therefore, the small high velocity spall debris is expected to be ejected from the wall before the gross motion takes effect. However, the heavier spall debris which has but little velocity is expected to stay in contact (or near contact) with the wall and will be later ejected by the wall motion at quite high velocities. The kinetic energies of this debris are at least one order of magnitude higher than the values produced by direct spall. It therefore appears that the severest effects of spallation may be due to coupling to the gross wall motion which arises from the total blast impulse loading.

Based on the foregoing analysis and computational results a number of important conclusions may be reached. First it appears that a cut-off for spalling of concrete may be expected at an angle of about 45 degrees because of the phase reversal in the reflection coefficient. The angle will be smaller for larger standoff distances because the tensile stresses will not exceed the rupture strength at large angles. In fact, if the tensile rupture strength is indeed 2000 psi no spalling can take place for scaled standoff distances larger than 1.8 $ft/lb^{1/3}$. The second important point is the above described coupling between spalling and the wall motion produced by impulse which leads to the high velocity ejection of most spall debris. Finally for explosions of interest, the total spall depth throughout the crater is greater than the thickness of the concrete cover on the backface reinforcement. Thus unless very severe wall deformations occur the concrete cover depth will be the limit on ejected debris. All these facts lead to a simple "first cut"

estimate of spall debris ejection, without performing any detailed spall calculation. The debris mass is simply limited by the spall cut-off (45° or smaller) and the depth of the concrete covering the reinforcement, while its velocity is obtained from the wall motion produced by impulse, as given in Fig. 7.

5. CONCRETE DEBRIS EFFECTS

The debris produced by concrete wall spalling or disintegration, when ejected at high velocity may upon impact produce severe damage to structures and equipment. Nuclear power plants have typically one of two arrangements: (1) a free standing steel containment surrounded by a concrete shield structure or (2) a concrete containment with an attached thin steel liner. Since the prime purpose of steel liners is to provide air leak tightness, they are shallowly anchored in the concrete and contribute little to the strength of the containment wall. However, unless complete wall disintegration occurs, the liners may be able to contain or retard the concrete debris.

The debris may separate from the concrete wall as individual concrete fragments or as a large coherent mass of concrete. For fragment impact, the loading on the steel is very local and the analysis of the phenomenon must be based on penetration mechanics. When large masses of concrete impact a steel structure, the load is more distributed and the phenomenon may be approximated as the impact of two plates or as the impulsive loading of a plate. Consistent with the assumptions made in the concrete wall analysis, the steel structures are approximated as flat plates with the boundaries sufficiently far removed from the impact region, so that their presence may be neglected.

5.1 IMPACT OF CONCRETE FRAGMENTS

All of the existing penetration mechanics analyses, including the most recent work, e.g., [2,3,15,16], concerns the impact of metal fragments (or projectiles) on concrete, steel, etc. Usually it is assumed that the missile is either rigid (nondeformable) [2,3] or that it deforms plastically [15].

Neither of these assumptions is obviously appropriate for concrete fragments impacting on steel. Due to the differences in compressive strength and the lack of ductility in concrete, either considerable crushing or rebound of the missile is to be expected depending on the impact velocity range. Assuming a rigid, noncrushable and nonrebounding concrete missile should therefore result in very conservative penetration estimates. Concrete fragments may be expected to have irregular shapes while the existing analyses assume a regular shaped missile. Because of all these discrepancies between concrete fragment impact and the existing penetration analyses and theories, estimates of the concrete on steel penetration were made using the simplest available empirical relationship [16], which is based on the most recent compilation of missile penetration data.

The missile is assumed to be of a standard cylindrical shape with the diameter d (in.) being equal to the length and with the nose curvature $r = d/2$ (see sketch in Table 1). The penetration x (in.) is then

$$x = K\, D\, d\, v^{\alpha} \tag{48}$$

where, $D = W/d^3$ is the caliber density, W is the weight of the projectile (lb), and v is the impact velocity (K ft/s). The exponent α depends on the target material and has a value $\alpha = 1.22$ for steel. The constant K depends on the hardness of the missile material; we use for concrete the same value as for armor piercing steel $K = 2.33$. These values together with a typical specific weight of concrete (0.0868 lb/in^3) lead to the following relationship

$$x = 0.128\, d\, v^{1.22} \tag{49}$$

TABLE 1

CONCRETE FRAGMENT IMPACT ON STEEL

STANDARD MISSILE SHAPE

r=d/2

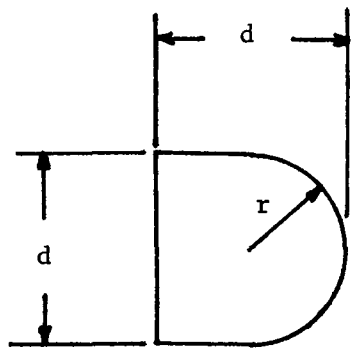

PENETRATION-x (in.)					
DIAMETER d(in.)	VELOCITY-v (ft/s)				
	50	100	200	300	400
1.0	.0033	.0077	.018	.030	.042
2.0	.0066	.0154	.036	.059	.084
3.0	.0099	.0231	.054	.086	.125
4.0	.0132	.0308	.072	.118	.167
6.0	.0198	.0462	.108	.177	.251
12.0	.0396	.0924	.216	.354	.502

Typical penetration results calculated with eq. (49) are given in Table 1. With all the conservativeness built into this expression, the penetrations are still very minimal. It therefore appears that the impact of individual concrete fragments on steel structures will have little or no detrimental effects. This is particularly true for steel containments which are relatively massive structures with wall thicknesses far in excess of penetrations one can realistically expect from concrete fragment impact. It appears from eq. (49) that penetrations are proportional to the missile diameter d and would further increase as the diameter increases. However, the underlying assumptions [16] of very localized loading make the application of this empirical expression unacceptable for fragments of larger size.

5.2 IMPACT OF LARGE DEBRIS MASSES

As pointed out earlier, the impact of large masses of concrete debris on a steel containment structure can be approximated as the impact of a concrete plate on a steel plate. The size and thickness of the concrete plate can be ascertained from the response analyses of the concrete shield wall. Depending on the severity of concrete wall deformation, the debris may be produced by spalling, scabbing or wall disintegration. The last two are late-time mechanisms occurring near the end of the deformation period when the wall velocity is diminishing and ultimately approaches zero. Thus the debris velocity will in general be small. On the other hand, the spalling debris separates before high wall deflection velocities are attained. Thus it is assumed that it is the spalling debris which may be ejected at high velocities. The mass of the spalling debris is assumed to be in the form of a circular plate with a depth equal to the concrete cover depth over the rear face reinforcement. The radius of the debris mass, a, is given by the spall cutoff, i.e., by an angle of incidence of 45° or smaller, and

is obtained from the following expression

$$a = (h + y)\tan \alpha_c \tag{50}$$

where y is the standoff distance, h is the wall thickness and α_c is the spall cut-off angle which in general may be taken as 45°. Since the debris radius, a, depends on the wall thickness, it is not a scalable quantity. This in turn implies that the steel plate response cannot be scaled since, as will be seen, it depends on the radius of the loaded area.

The relative timing between spalling and gross wall motion is not known, therefore it is not at all clear which velocity should be used as the debris velocity. We arbitrarily select as the debris velocity, the velocity of the wall produced by the blast impulse acting on an area with radius equal to that of the spall cutoff. As seen in Fig. 7, this velocity is in general higher than the velocity corresponding to the impulse which produces maximum wall deflection. The resulting impact should therefore be conservative.

For impact velocities in the range of 50-400 ft/s the impact pressures computed by impedance matching between steel and concrete (assuming elastic behavior for both materials) vary from 1.3×10^4 psi to over 10^5 psi. These pressures are many times larger than the compressive strength of concrete, thus crushing of the debris should be expected. At high impact velocities, the yield strength of steel, which is of the order of 3×10^4 psi, is also exceeded, while at low impact velocities the steel structure may be expected to respond elastically. It is therefore not at all obvious which type of impact analysis is appropriate. Because of the complexities of elastic analysis, the assumption is made that the steel structure can be treated as a rigid-perfectly plastic plate with a priori assumed deformation modes. Further the load is again assumed to be impulsive, permitting the

the decoupling of the loading and response phases.

Initial velocity estimates of the steel plate can be obtained by considering the impact to be either fully plastic or perfectly elastic. Again the true impact process is probably more complex. However, reasonable velocity bounds can be based on the plastic and elastic impact velocities. Assuming only inertial resistance during loading, the elastic velocity will be an upper bound. A true elastic impact analysis should consider the wave motion in the plates. However, due to all the other uncertainties we limit our estimate to an instantaneous perfectly elastic impact. Then the momentum and energy equations are respectively:

$$m_c v_c + m_s v_s = m_c v_{co} + m_s v_{so} \tag{51}$$

$$m_c \frac{v_c^2}{2} + m_s \frac{v_s^2}{2} = m_c \frac{v_{co}^2}{2} + m_s \frac{v_{so}^2}{2} \tag{52}$$

Here $m = \rho h$ is the mass per unit area, ρ is the density, h is the plate thickness, v is the velocity. Subscripts c and s refer respectively to the concrete and steel plate. Subscript o desigantes the state before impact while the nonsubscripted velocities occur after impact. For the current application $v_{so} = 0$. Solving equations (51) and (52) simultaneously yields:

$$v_{se} = \frac{2\, v_{co}}{1 + \frac{m_s}{m_c}} = \frac{2\, v_{co}}{1 + \frac{\rho_s h_s}{\rho_c h_c}} \tag{53}$$

where subscript e designates elastic impact.

When the impact is perfectly plastic the energy equation (52) is not applicable. The momentum equation together with the condition that after

impact the two velocities are equal, i.e., $v_{sp} = v_{cp}$ (subscript p refers to plastic impact) gives the following expression

$$v_{sp} = \frac{v_{co}}{1 + \frac{m_s}{m_c}} = \frac{v_{co}}{1 + \frac{\rho_s h_s}{\rho_c h_c}} \tag{54}$$

For any given situation the velocity imparted to the steel plate under elastic impact is twice as high as that resulting from plastic impact. It should also be noted that for fixed material properties the ratio of the steel plate velocity to the concrete debris velocity is in both cases only a function of the plate thickness ratio. For typical concrete and steel properties the ratio of the densities is $\rho_s/\rho_c = 3.37$. Thus equations (53) and (54) may be rewritten as follows:

$$v_{se}/v_{co} = \frac{2}{1 + 3.37\ h_s/h_c} \tag{55}$$

$$v_{sp}/v_{co} = \frac{1}{1 + 3.37\ h_s/h_c} \tag{56}$$

Much work has been done in recent years on the rigid-plastic response of plates under impulsive loading [17,18,19,20]. In most cases a finite size circular plate with either simple or clamped supports at the edges is considered. Taking into account plate bending, membrane stresses and strain rate effects it is only possible to obtain simple deflection relationships for the case of uniform impulse over the entire plate [17]. The only analysis directly applicable to our problem [20] considers an infinite thin plate with the load applied over a finite circular area of radius r = a. The plate is assumed to be rigid-ideally plastic with a deflection mechanism consisting of a hinge at the center r = 0 and a hinge circle at $r = r_o$. For impulsive loading the final deflection δ

at the center is predicted to be [20]:

$$\delta = \frac{m\, r_o^2\, v^2}{48\, M_o} = \frac{r_o^2\, I^2}{48\, m M_o} \tag{57}$$

Here m is the mass per unit area of plate, I is the impulse per unit area, v is the initial plate velocity, and M_o is ultimate (yield) moment. The latter quantity is given as

$$M_o = \frac{1}{4}\, h_s^2\, \sigma_o \tag{58}$$

where h_s is the plate thickness and σ_o the yield strength of the plate material. Estimates of the initial velocity v can be obtained from either eq. (55) or eq. (56) depending on the assumptions made regarding the impulse process. The size of the initial hinge radius r_o is not known. However, considering the case of a pulse of constant intensity, p, and short duration it can be shown [20], that the hinge radius is a constant which can be expressed in terms of the load radius, a, as follows:

$$r_o = \frac{4}{3}\, \frac{pa^2}{pa^2 - 4\, M_o}\, a \tag{59}$$

In the current application, load intensities of the order of 10^4 psi are expected, while typical radii of the impacting debris will be on the order of feet. With a steel plate thickness on the order of a couple inches and typical yield stresses for steel one finds that $pa^2 >> 4$ Mo. Therefore eq. (59) may be approximated as

$$r_o \overset{\sim}{=} \frac{4}{3}\, a \tag{60}$$

Using the above expression in eq. (57) one finds that central plate deflection can be calculated from

$$\delta = \frac{m\, a^2\, v^2}{27\, M_o} \tag{61}$$

Typical results are shown in Fig. 25, where the deflection is given as a function of scaled standoff distance for three different charge weights. Computations for both elastic and plastic impact velocities are given. As mentioned earlier, these should bracket the true results. The approach of the spall limit causes the rapid drop-off in the deflection curves at a scaled standoff distance of about 1.6 ft/lb$^{1/3}$. Due to the direct dependence of the load area radius, a, on the wall thickness the results are not scalable. However, the computations are so simple that deflection estimates are readily obtainable for any wall.

A comparison of deflections for two walls of different strength and thickness is shown in Fig. 26. It should be noted that the ultimate moments indicated both in Figs. 25 and 26 refer to the wall and not the impacted plate. For a charge weight of 10^3 lb the deflections are seen to be quite moderate, even for the 2.5 ft wall, except at the very close-in charge locations. When charge weight increases to 10^4 lb, severe damage can be expected since plate deflections in excess of 1 ft are predicted for much of the standoff range.

It is not possible to formulate precise failure criteria. Since a circular yield pattern was assumed, eq. (19) can be used to estimate the relationship between strain ε and hinge rotation θ where $\tan\theta = \delta/r_o$. Knowing the rupture strain limit for the material a failure criterion based on local deformation effects might be postulated. This however provides no information on what effect the local deformation might have on gross structural response, i.e., structural stability.

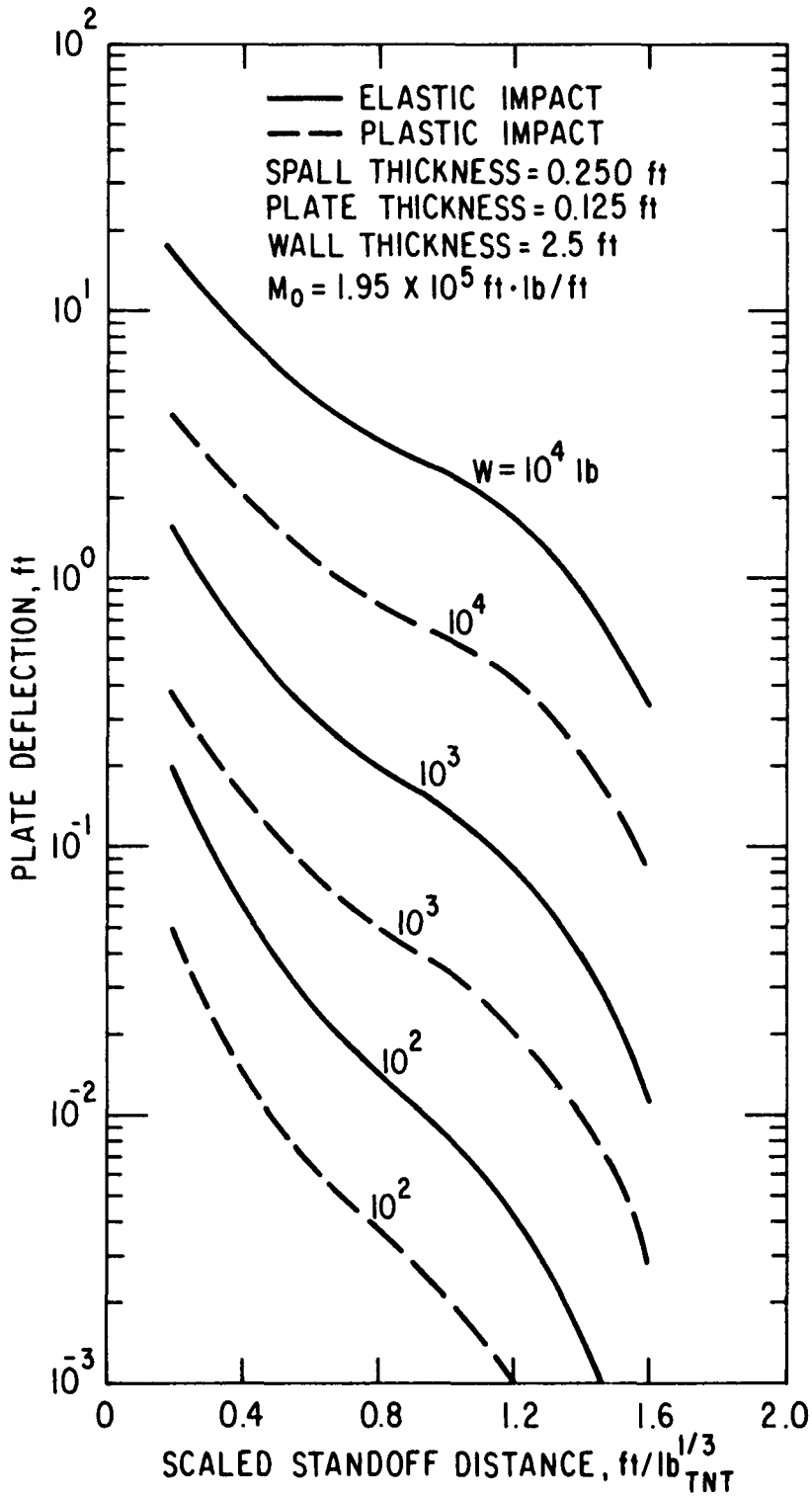

Fig. 25. Variation of Steel Plate Deflection due to Concrete Debris Impact

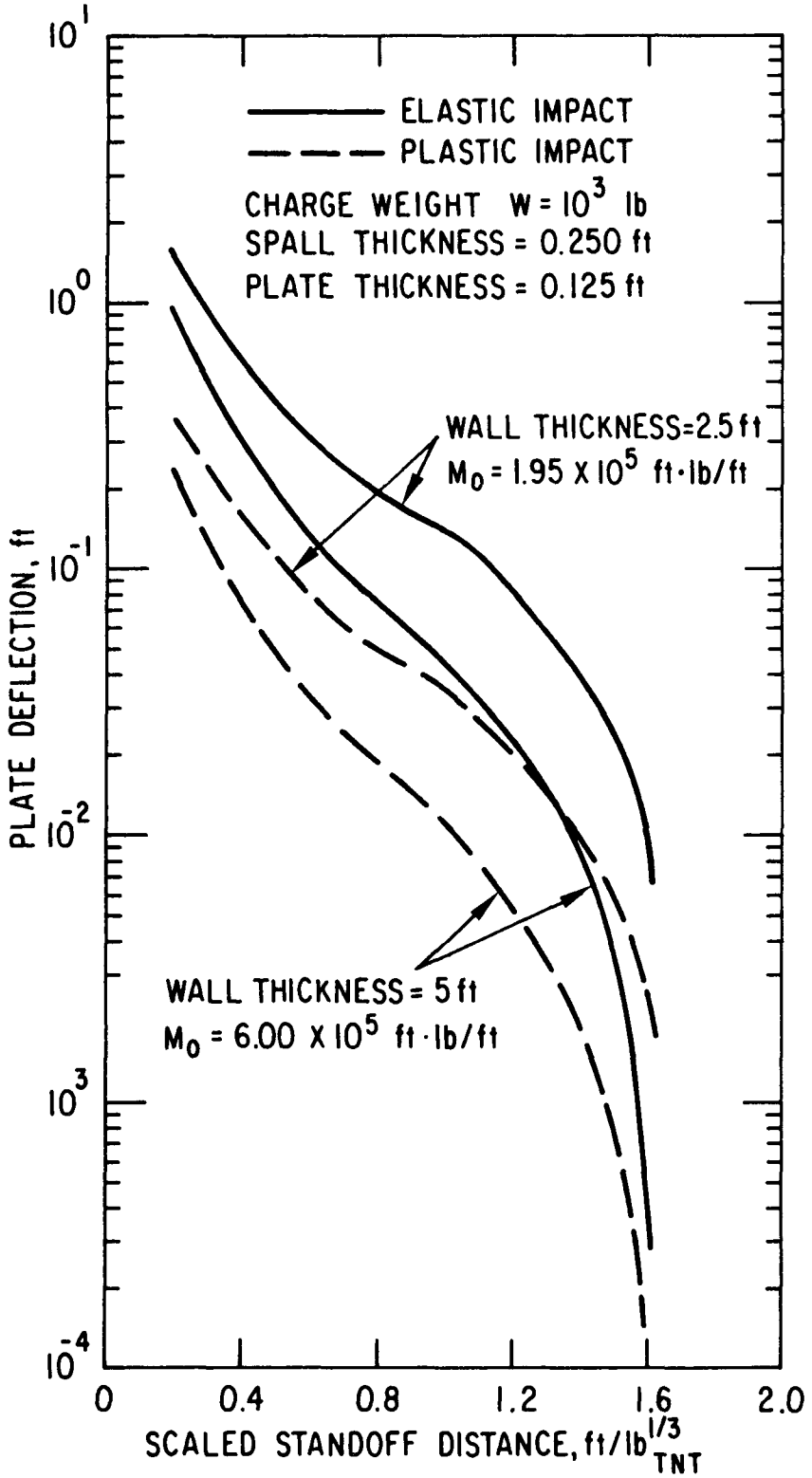

Fig. 26. Effect of Concrete Wall Parameters on Steel Plate Deflection (Charge Weight $W = 10^3$ lb)

5.3 EFFECT OF CONCRETE DEBRIS ON STEEL LINERS

The presence of a steel liner on the inside face of a concrete containment structure contributes little to the strength of the wall. Thus the liner is expected to deform together with the gross motion of the wall. However, in the region where spalling takes place, the liner becomes detached from the wall and additional liner deformation may occur due to the action of the loosened debris. At the same time the liner acting as a membrane may prove effective in containing the spall debris.

The process of liner detachment and subsequent deformation is very complex. Since liners attach to the concrete by means of structural steel members, a certain amount of bending resistance should be expected. Here, however, it will be assumed that only membrane stresses are important in describing liner deformation. Since the liner also moves with the wall it is not at all obvious what velocity should be used to obtain the relative motion between liner and wall. It will be conservative to assume that the wall velocity at spall cut-off (see Fig. 7) can be used as an estimate of the liner velocity relative to the wall. In effect this implies that the wall comes to rest at that time while in reality its motion continues past that point.

Assuming the liner to deform into a spherical membrane the deflection normal to the wall ξ at any radial position r is given in terms of the central deflection δ as

$$\xi = \delta\left(1 - \frac{r^2}{r_o^2}\right) \tag{62}$$

where r_o is the radius of the membrane (radius of liner attachment). The value of r_o is taken as the spall cut-off radius, i.e., the radial distance

at the backface of the wall at 45° angle of incidence. The problem of a plastically deforming membrane under impulsive loading has been treated by many investigators. Following the analysis presented by Cole [21] it is found that the plastic work WP in deforming a spherical membrane is

$$WP = \pi \sigma_o h_s \delta^2 = 4 \pi M_o \delta^2 / h_s \tag{63}$$

where σ_o is the liner yield stress, M_o the liner ultimate moment and h_s the liner thickness. At the final state this work must equal the kinetic energy KE imparted to the membrane by the impulse

$$KE = \frac{1}{2} M v^2 = \frac{1}{2} m \pi r_o^2 v^2 \tag{64}$$

Here M is the total mass moving at the initial velocity v , i.e., M is the sum of the detached liner mass and of the spalled concrete debris mass. Similarly m is the combined mass per unit area of liner and concrete, $m = m_s + m_c$. Equating the two energies given by eqs. (63) and (64) one obtains the final central deflection of the liner.

$$\delta = r_o v \left(\frac{m}{2 \sigma_o h_s}\right)^{1/2} = r_o v \left(\frac{m h_s}{8 M_o}\right)^{1/2} \tag{65}$$

It should be noted that while m is the combined mass per unit area the thickness h_s is only that of the liner. Again since r_o depends on the concrete wall thickness the deflections cannot be scaled. However, with v known (from Fig. 7) the deflection is readily computable. Results for a typical 2.5 ft thick wall and a 0.25 in. thick liner are shown in Fig. 27. Deflections in excess of 1 ft. are obtained for the entire range of standoffs when the charge is 10^4 lb and for close-in distances at a charge weight of

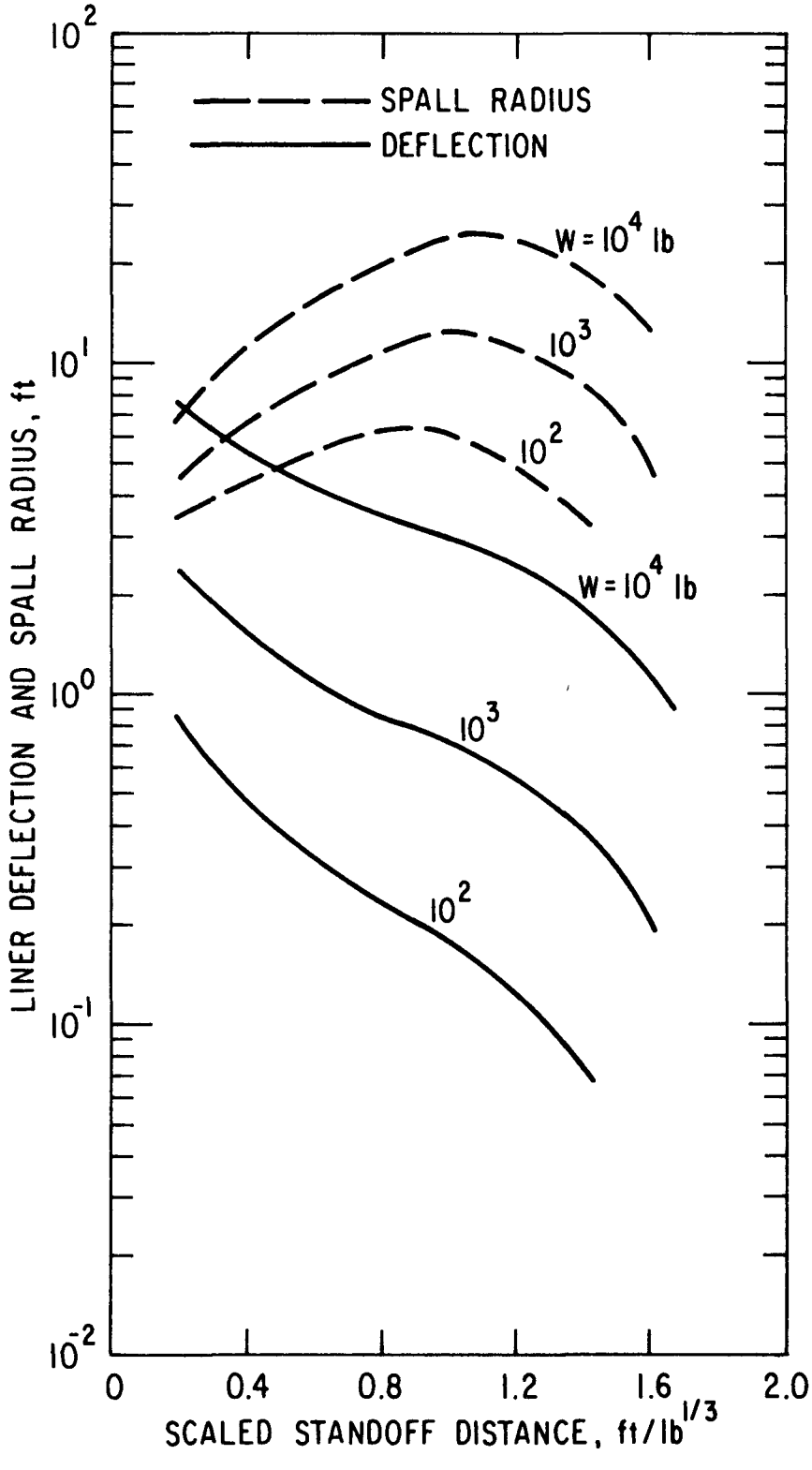

Fig. 27. Variation of Liner Deformation and Spall Radius with Standoff and Charge Weight

10^3 lb. Also shown in the figure are the spall radii r_o for the three charge weights. The decrease in radius at larger standoffs occurs because the actual spall cut-off limit is shifted to angles of incidence smaller than 45 degrees, i.e., the reflected pressure at angles beyond the cut-off is insufficient to produce spalling.

It should be kept in mind that the computed deflections are a rough estimate of liner deformation relative to the concrete wall. Thus, when actual wall displacements are large there will be additional liner deformations. However, in these cases, membrane liner response may be of little interest because other failure modes such as buckling and local tearing, which are associated with substantial wall disintegration, will predominate.

The only membrane failure criterion which may be readily formulated is again based on the strain at rupture. Since the increase in area of a spherical membrane may be approximated by [21] $\Delta A = \pi\delta^2$ and the original plate area is $A = \pi r_o^2$ the ratio of $\Delta A/A$ may be used as a measure of the plastic membrane strain, i.e.,

$$\varepsilon = \left(\frac{\delta}{r_o}\right)^2 \tag{66}$$

When this ratio exceeds the value of the rupture strain of the liner material failure may be expected.

6. AIR BLAST EFFECTS ON PIPES

Severe damage to piping, such as the main feedwater or steam lines, located outside of containment in nuclear power plants may pose a grave safety hazard. It is therefore necessary to obtain estimates of the deformation which may result when such piping is subjected to air blast loading from high explosives detonation. No satisfactory analysis method of this problem exists currently and no empirical data from controlled experiments is available. A method of obtaining pipe deformation estimates which utilizes recent results in dynamic plasticity is therefore developed. Details of this analysis are presented in the Appendix. It should be noted that the method outlined provides only a rough approximation. Also when the loading of the pipe is from close-in detonations many assumptions of the analysis are open to question.

It is again assumed that the loading is impulsive and that deformations are related to the total transverse impulse I_T experienced by the pipe. As indicated earlier (Section 2) the blast impulse acting on a pipe must be obtained by numerical integration of the local reflected impulses over the pipe surface. The results so obtained cannot be scaled with charge weight because of the finite pipe diameters. Figures 28 to 32 present the total transverse air blast impulse, each for a pipe of different diameter (1 ft to 5 ft) as a function of scaled standoff distance. In each case results are given for three different charge weights (10^2, 10^3 and 10^4 lb) and four different pipe length (20, 30, 40 and 50 ft). For fixed charge weight and pipe length, the impulses differ by more than a factor of three over the range of pipe diameters from 1 ft to 5 ft. It is also readily apparent that the impulses are not directly proportional to the charge weight as is the case for a flat wall (see Fig. 6).

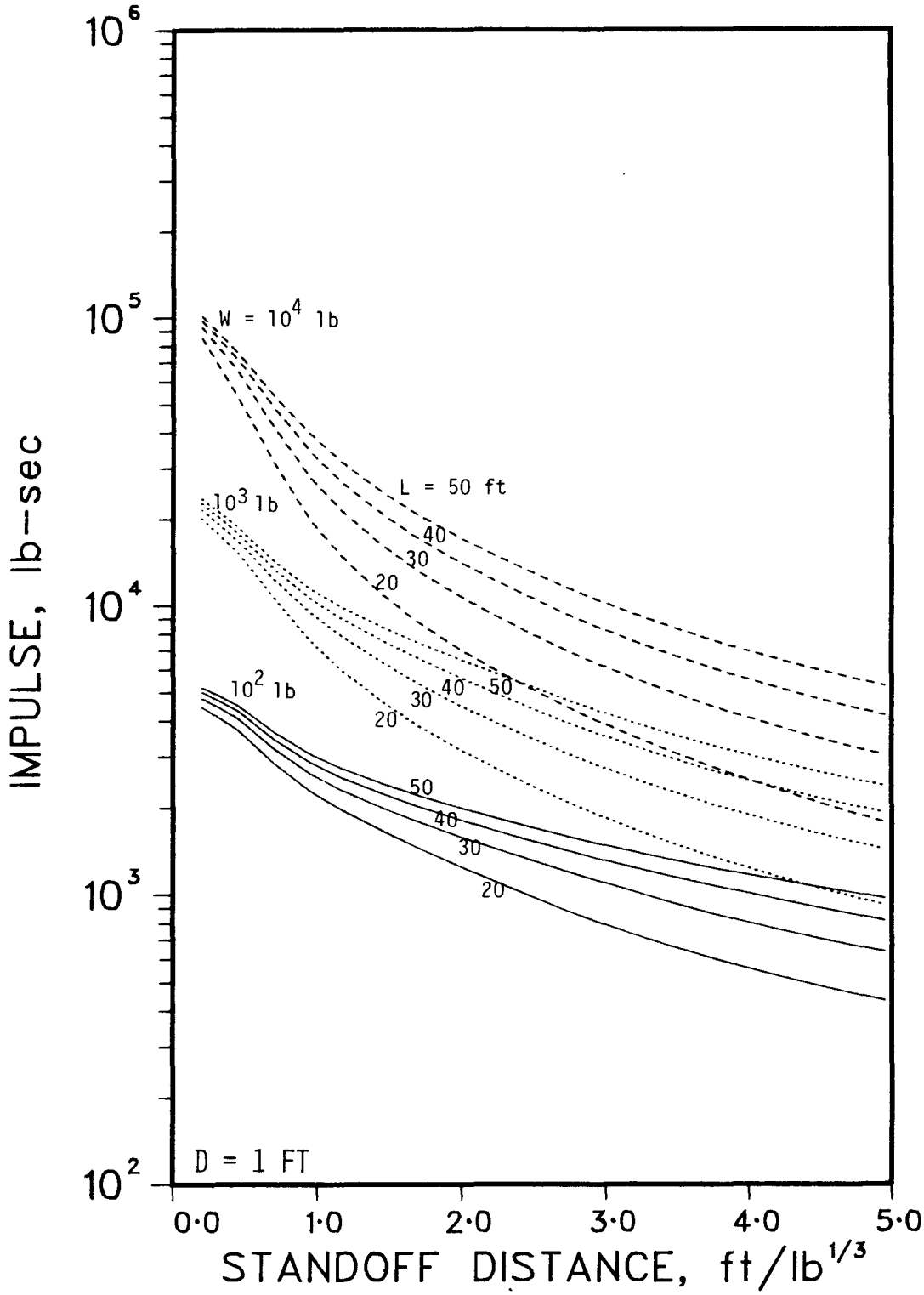

Fig. 28. Air Blast Impulse on Pipes - Pipe Diameter D = 1 ft

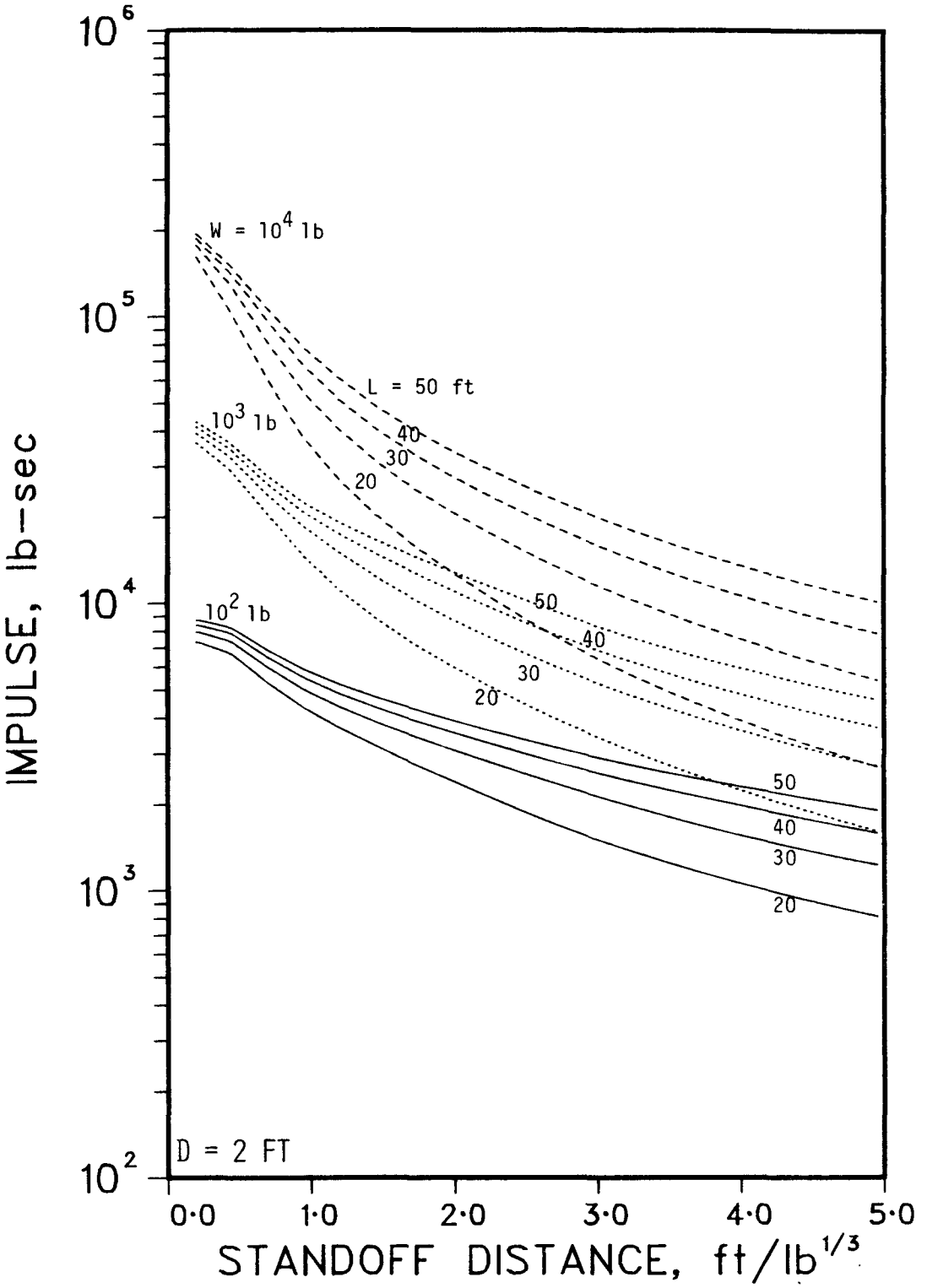

Fig. 29. Air Blast Impulse on Pipes - Pipe Diameter D = 2 ft

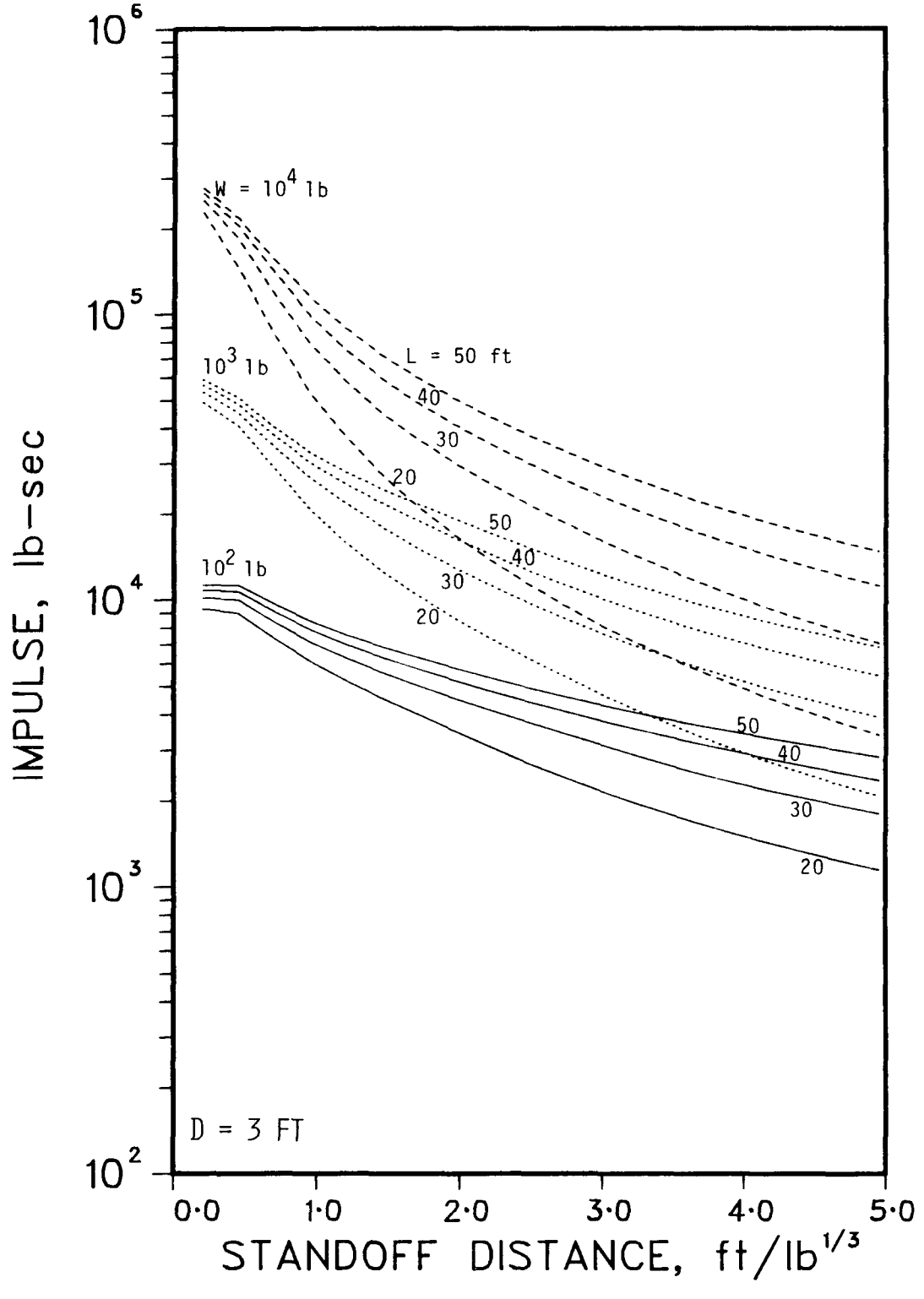

Fig. 30. Air Blast Impulse on Pipes - Pipe Diameter D = 3 ft

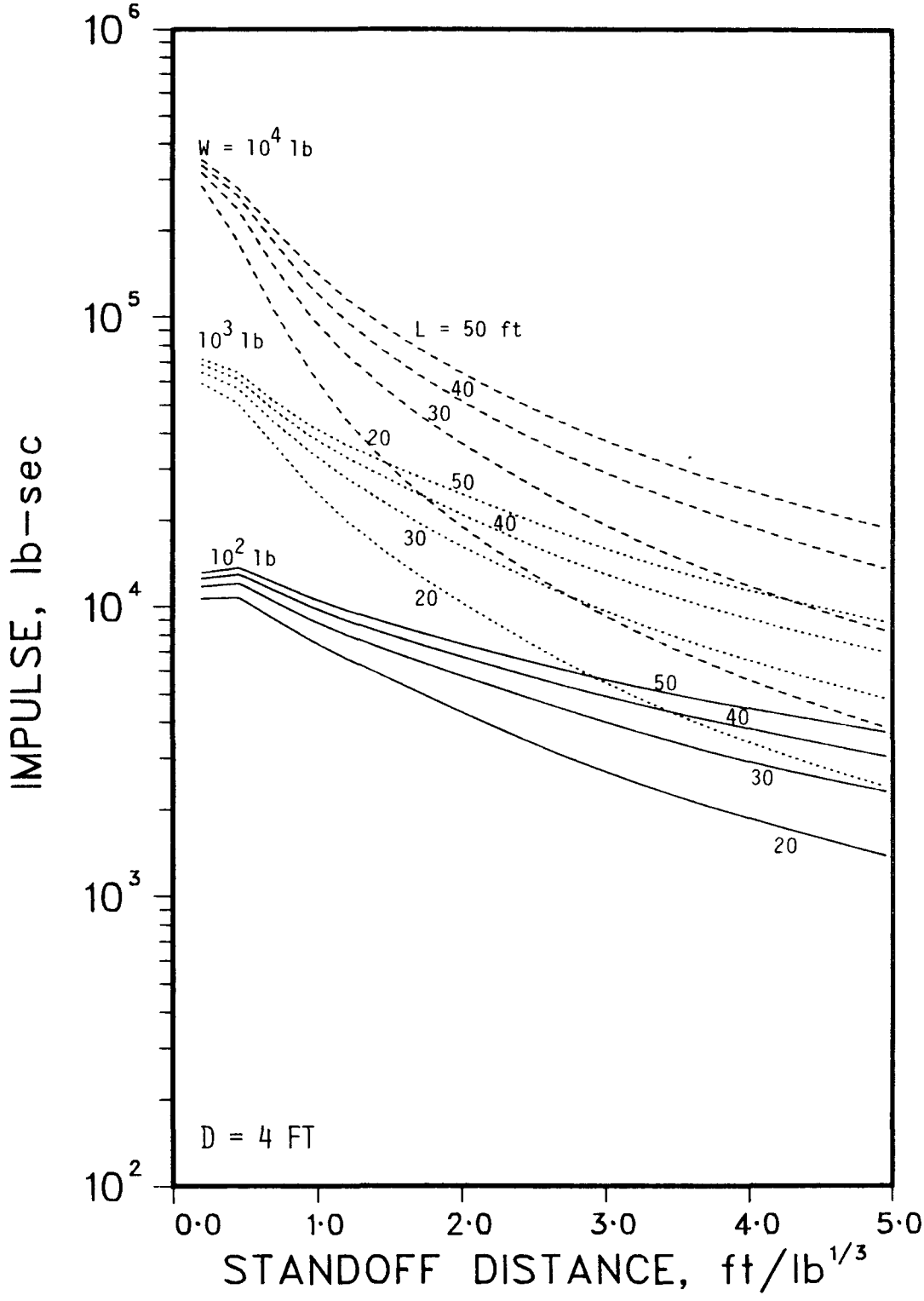

Fig. 31. Air Blast Impulse on Pipes - Pipe Diameter D = 4 ft

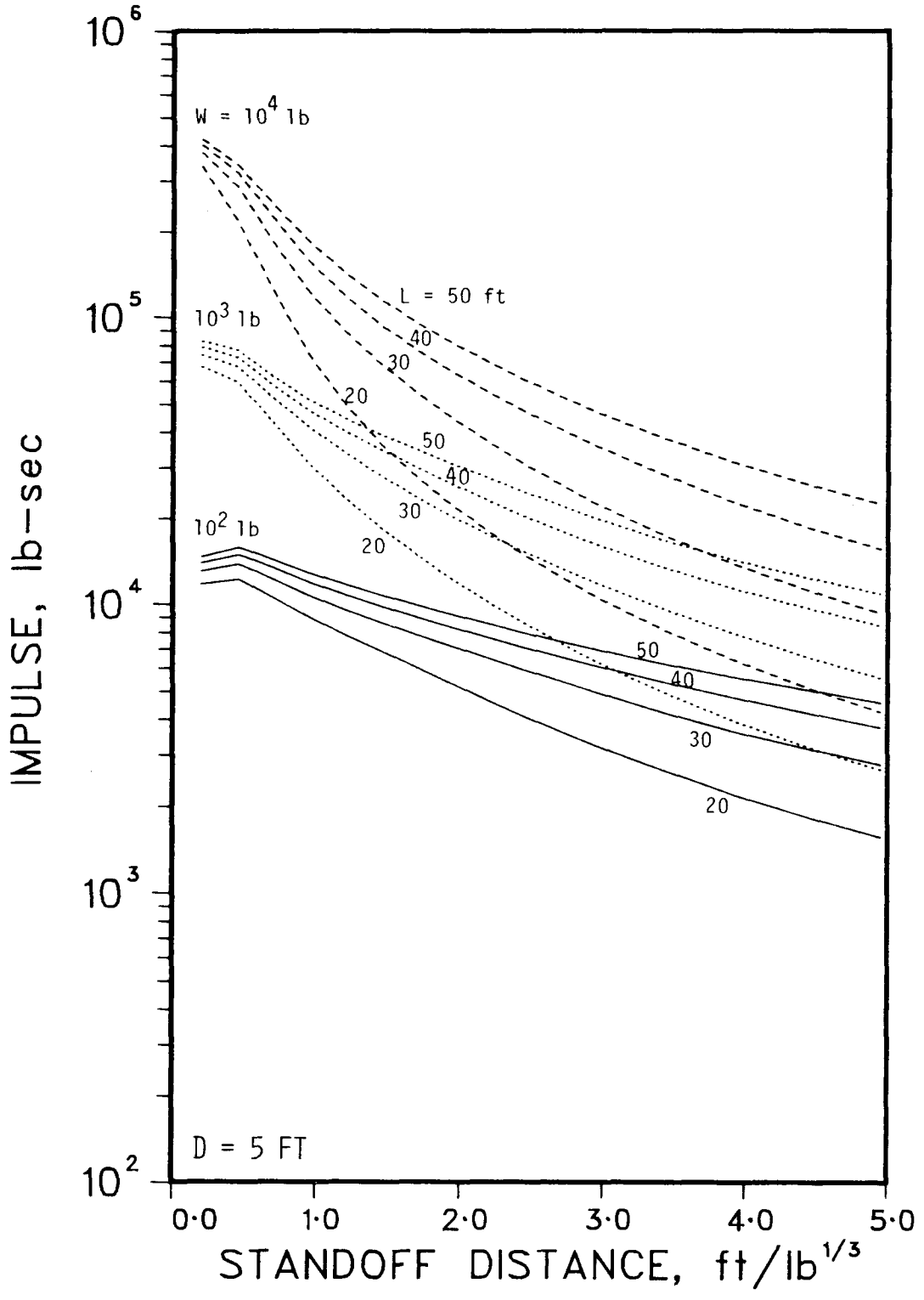

Fig. 32. Air Blast Impulse on Pipes - Pipe Diameter D = 5 ft

The analysis method outlined in Appendix A assumes two major forms of deformation for pipes under air blast loading. These are a beam like bending with no cross-sectional distortion and a local "ring" deformation of the pipe. For the latter no interaction between adjacent pipe sections is assumed. Similarly interactions between the two forms of deformation are neglected. For each type of deformation both a plastic mode and a bound or limit analysis method are employed to estimate the deflections and response times. To make the analysis simple a sine distribution of the transverse impulse is assumed. This leads in the case of the mode analysis method, which is expected to yield more realistic results, to the following maximum (central) deflection formulas:

Beam Deflection

$$\delta_b = w_*^f = \frac{3}{4\pi^2} \frac{I_T}{M_o \bar{\rho}} \tag{67}$$

Ring Deformation

$$\delta_r = u_*^f = 0.0286 \frac{(I_T/2)^2}{\sigma_y \rho_s h^3 \ell^2} \tag{68}$$

Here eq. (67) is identical to eq. (A12a) of Appendix A and eq. (68) corresponds to eq. (A26a). For the latter $I_T/2$ was substituted for the I_T of Appendix A so that the symbol I_T always has the unique meaning of total transverse impulse. σ_y is the yield stress of the pipe material, ρ_s the pipe material density, h the pipe wall thickness and ℓ the half length of the pipe. The fully plastic moment M_o and mass per unit length of pipe $\bar{\rho}$, which includes both the steel pipe and water, are given by the following expressions:

$$M_o = \frac{4}{3}(R_o^3 - R_i^3)\,\sigma_y \tag{69}$$

and

$$\bar{\rho} = \pi\,(R_o^2 - R_i^2)\rho_s + \pi R_i^2 \rho_w \tag{70}$$

where ρ_w is the liquid (water) density and R_o and R_i are respectively the outer and inner radius of the pipe.

Once the total transverse impulse I_T on a pipe is determined, it becomes a simple matter to calculate both the beam and ring deformation using eqs. (67) and (68). Deflection results for a fixed charge weight of $W = 10^3$ lb and five different pipe diameters (1, 2, 3, 4 and 5 ft) are presented in Figs. 33 to 37. In each figure both the beam and ring mode deformations are given each for four different pipe length (20, 30, 40 and 50 ft.). The pipes approximate Schedule 80 piping with the wall thickness assumed to be h = D/20, where D is the pipe diameter. A yield stress for steel at 600°F was used; its value is $\sigma_y = 2 \times 10^4$ psi.

The calculations clearly indicate that the ring deformation is only weakly dependent on the pipe length. Based on physical considerations, this is an expected result. In fact, if the proper local impulse rather than the total impulse were used in the computations, then the dependence of the ring deformation on pipe length should be negligible. The crossover observed in ring deformation curves can be explained by the variation of the term $(I_T/2\ell)^2$. At close-in standoffs where the impulse depends only weakly on pipe length (see Figs. 28-32), the ℓ^2 term dominates and ring deformations obtained from eq. (68) are smallest for the longest pipe. At far distances where I_T is strongly affected by pipe length, there is little difference in the deformations or they increase with pipe length.

As expected, beam deflections at a fixed pipe diameter increase with increasing pipe length. If the pipe length is held constant, both ring deformations and beam deflections decrease with increasing pipe diameter.

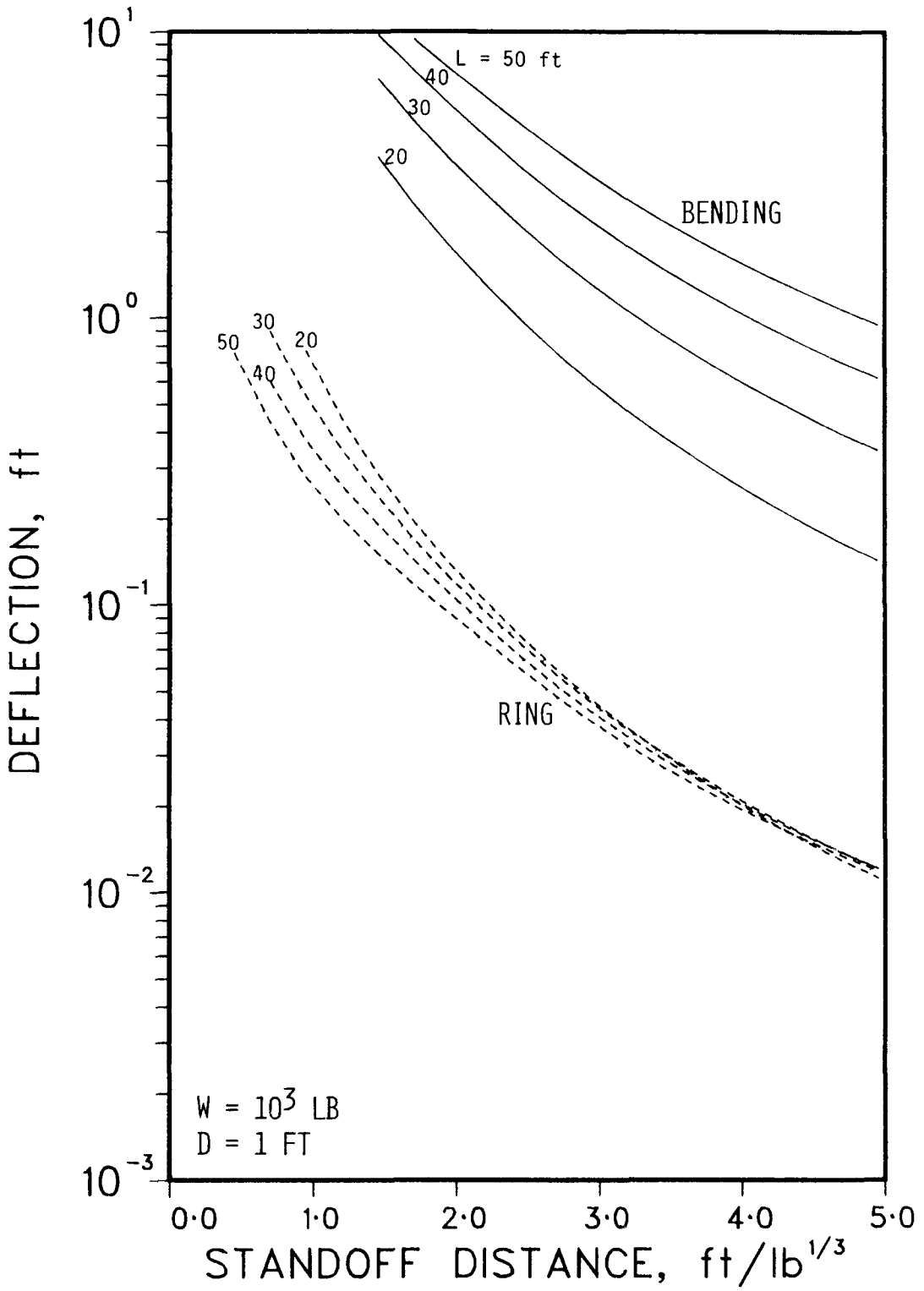

Fig. 33. Pipe Deformations - Pipe Diameter D = 1 ft

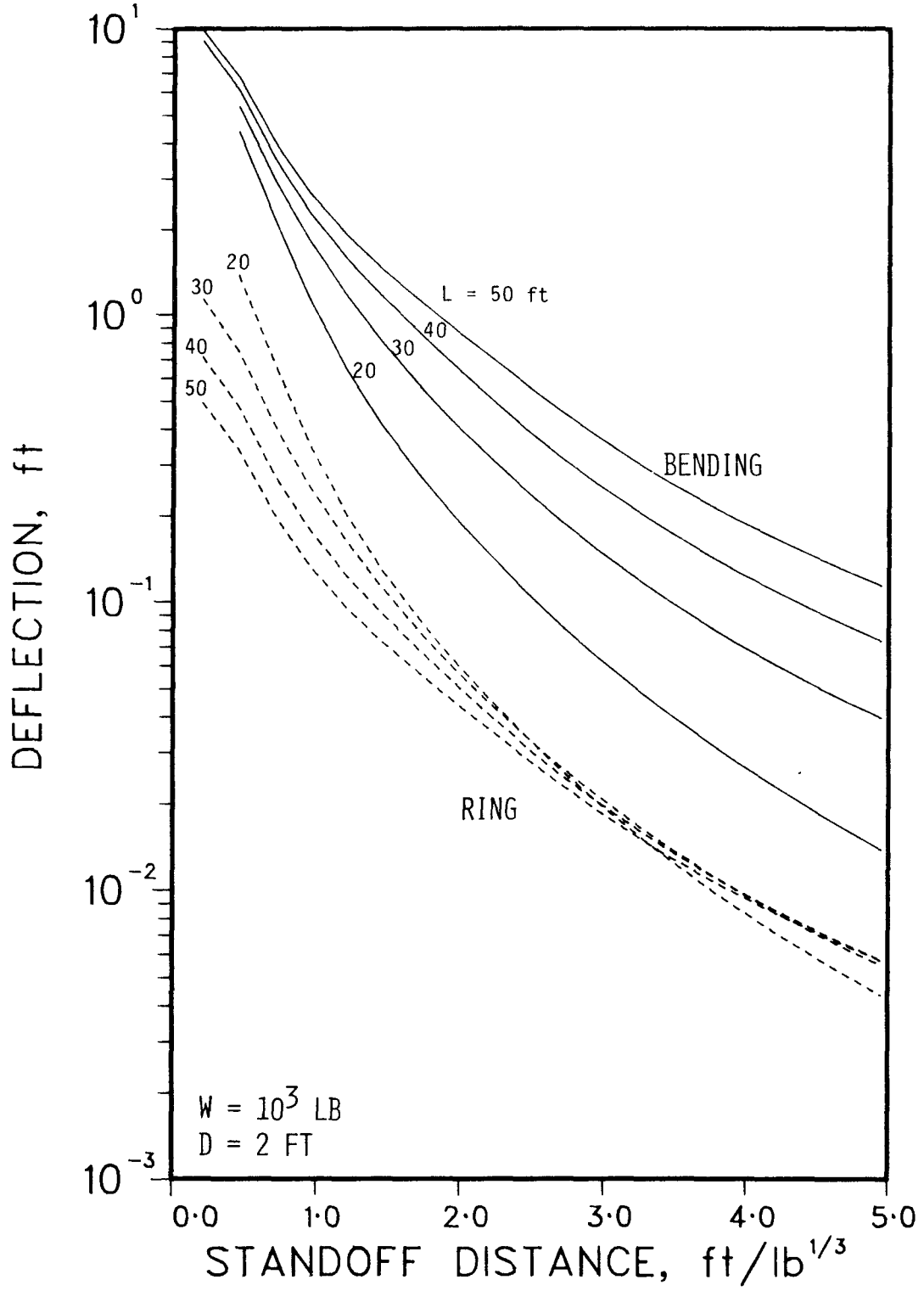

Fig. 34. Pipe Deformations - Pipe Diameter D = 2 ft

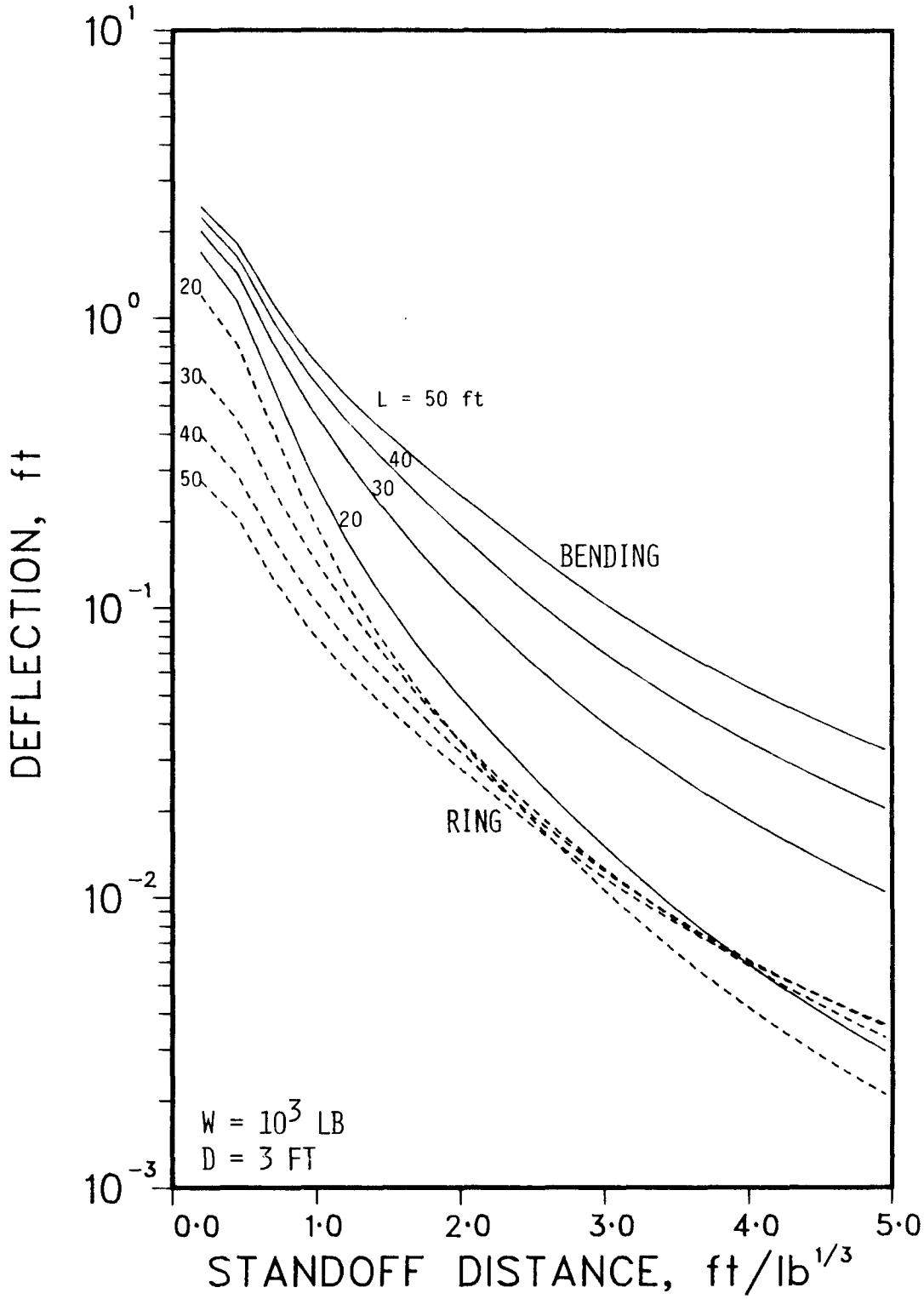

Fig. 35. Pipe Deformations - Pipe Diameter D = 3 ft

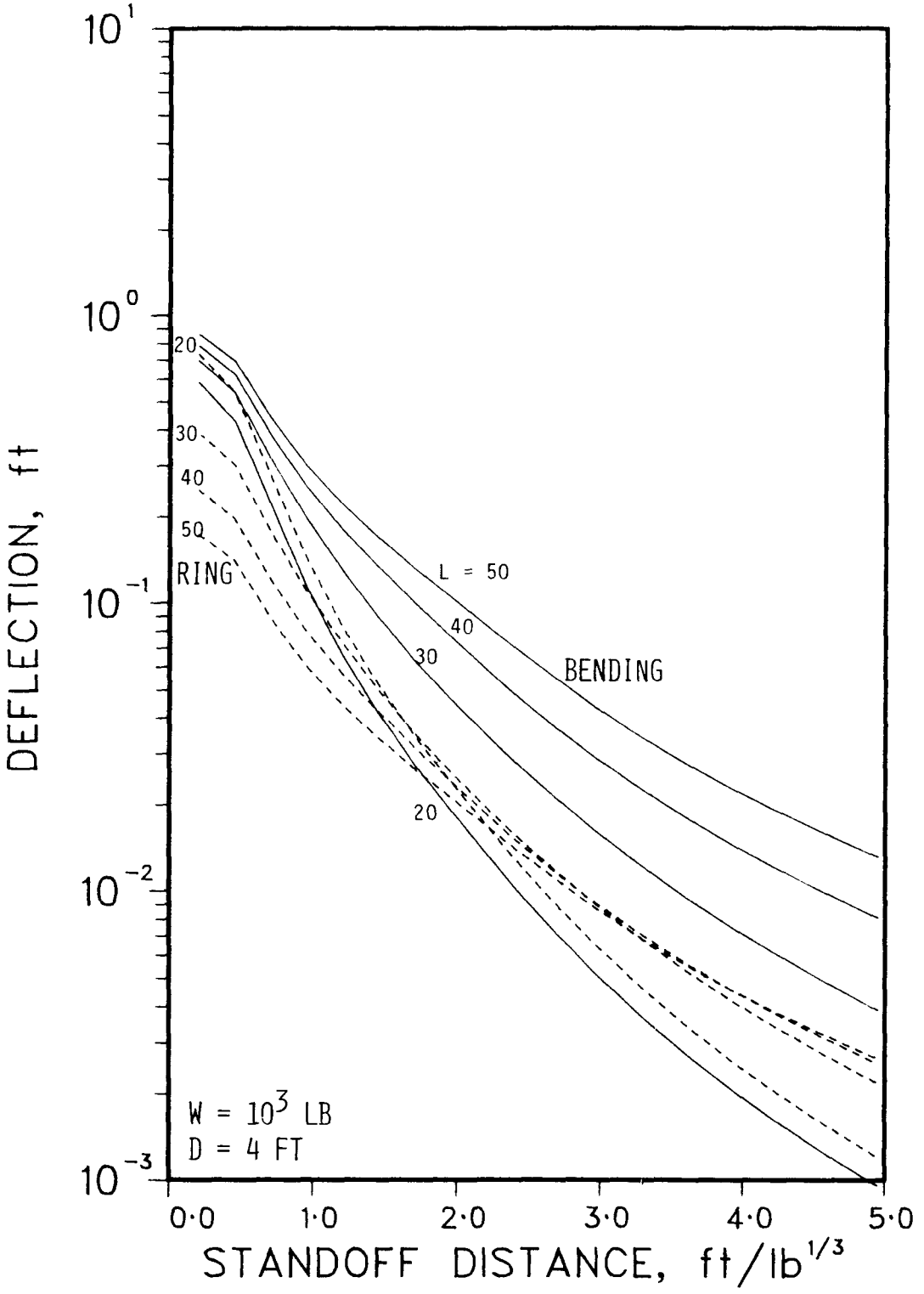

Fig. 36. Pipe Deformations - Pipe Diameter D = 4 ft

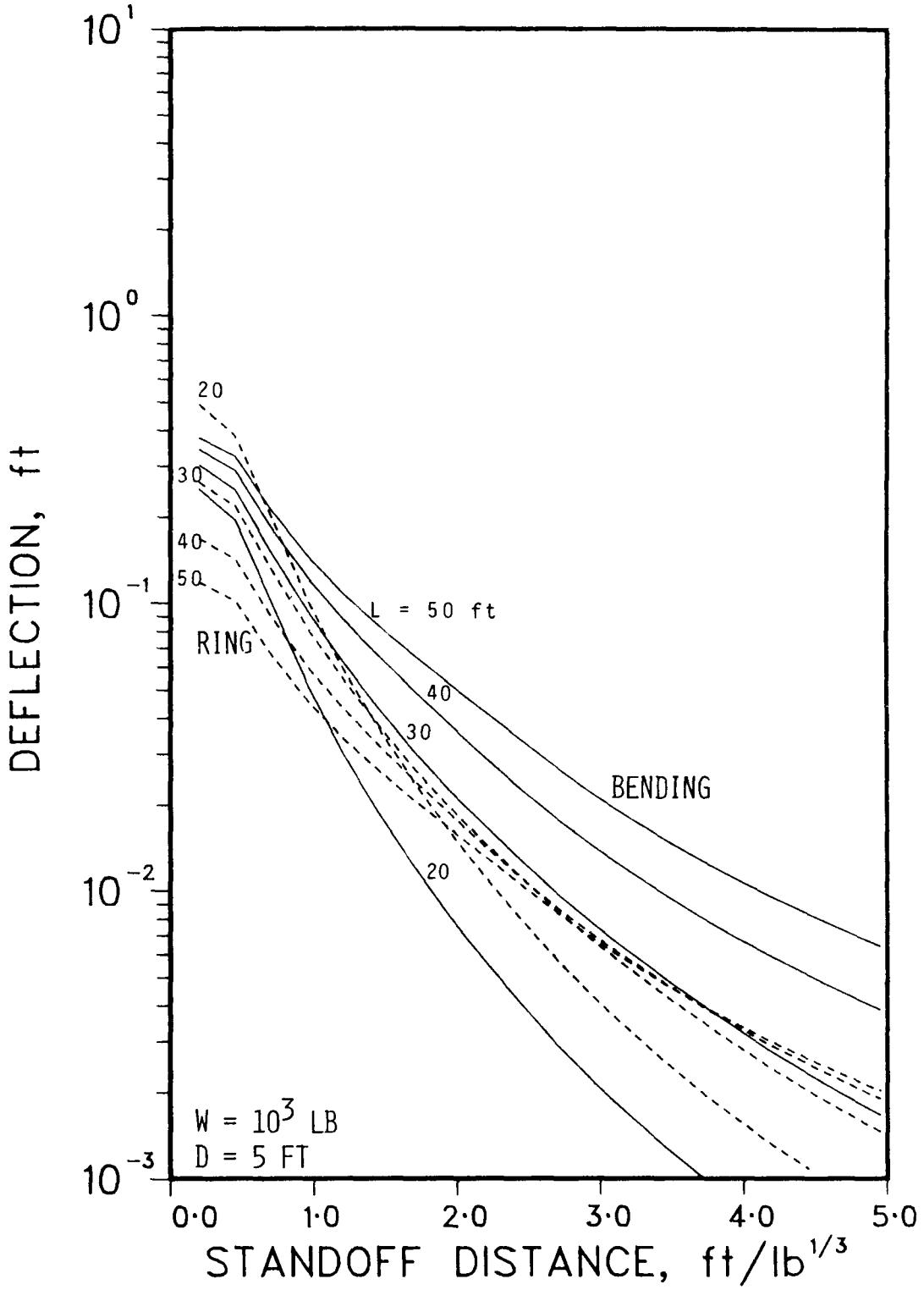

Fig. 37. Pipe Deformations - Pipe Diameter D = 5 ft

It is the strong (cubic) inverse dependence of the deformations on the pipe diameter (or wall thickness) that leads to this result. The effect is more clearly illustrated in Fig. 38 which gives the deflections for a 30 ft. pipe at five different pipe diameters.

In the graphical presentation of the results, maximum ring deformations were limited to one pipe diameter and beam deflections were restricted to the smaller of $\ell/2$ or 10 feet. Since both types of analysis are based on the assumption of small deflections (see Appendix A), the true range of applicability is probably much more restrictive. In general, the results are much more uncertain for small standoff distances. Here the deformations are large and are strongly influenced by local impulse intensity rather than the total impulse on the pipe. Based on the magnitude of the deflections it appears that the results for large pipe diameters may be more reliable than those for smaller pipes.

At the current stage of analysis development it is not possible to arrive at any precise failure criteria. Some intuitive notion on the severity of damage may be arrived at based on the physical appearance of the pipe. Thus at a ring deformation of one half the pipe diameter, one would expect severe pipe damage. For beam deflections a damage criterion must consider both the deflection itself and the pipe length. The ratio δ_b/ℓ which is a measure of the hing rotations both at the supports and the pipe center may therefore provide an appropriate criterion. However, no information on allowable magnitudes of hinge rotations exist and arbitrary limits must be selected. Since both in the analysis and in reality the pipe is not restrained longitudinally at the supports, no failure criterion based on pipe elongation can be formulated.

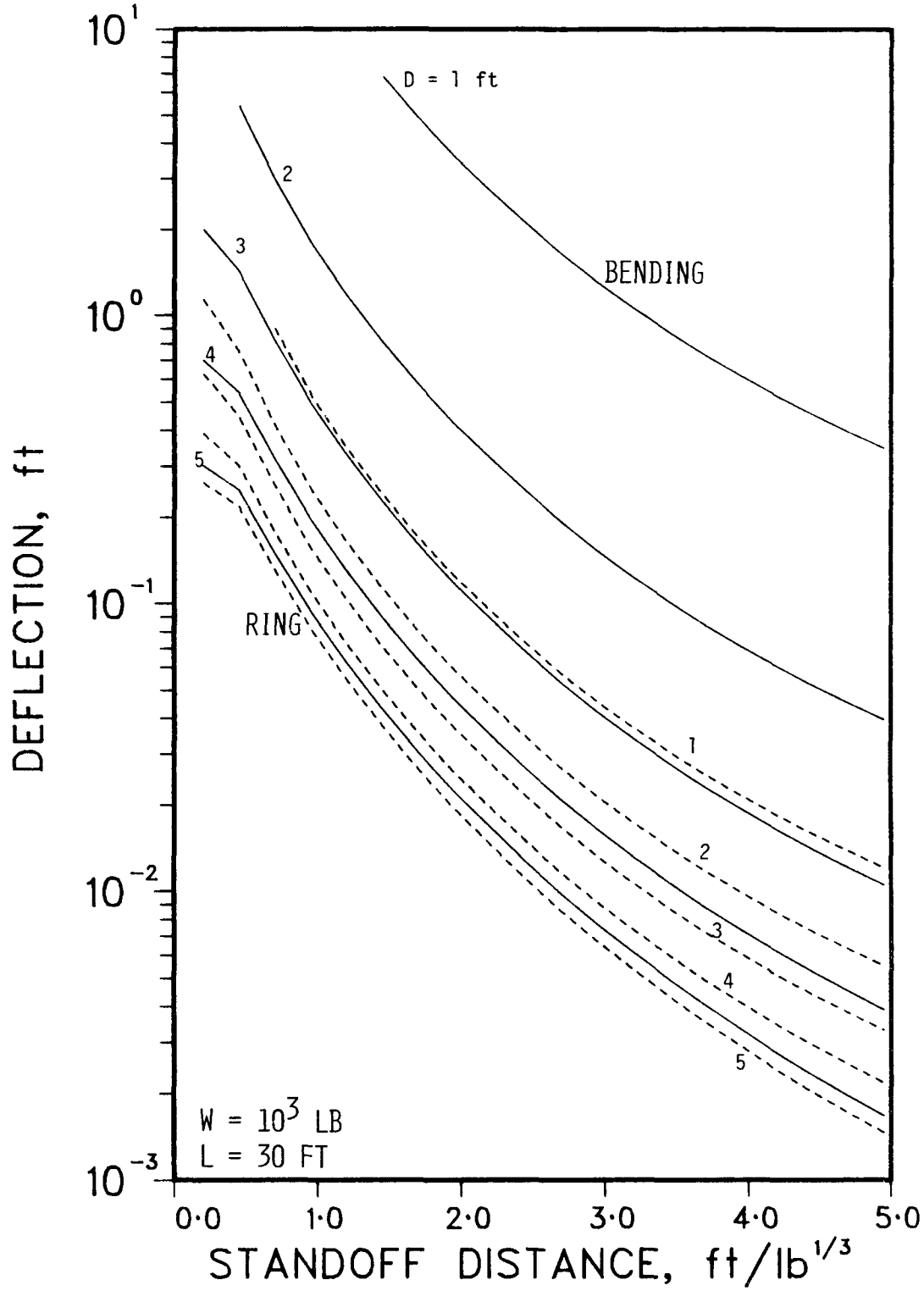

Fig. 38. Pipe Deformations - Pipe Length L = 30 ft

7. DISCUSSION AND CONCLUSION

The analysis methods and results presented in the foregoing sections provide a means for estimating the susceptibility of nuclear power plant structures and equipment to air blast loading generated by high explosives detonations. As indicated before, the effort was limited to investigating the response of only a few critical items such as containment and shield structures and important piping located outside of containment.

No developmental effort was undertaken during the course of this study, and the results are based on a synthesis of state of the art methods. In many cases extreme simplifying assumptions were made to permit the derivation of simple structural response relationships. In the presentation of results no attempt was made to cover the complete range of values which may be of interest in analyzing nuclear power plant susceptibility. However, sufficient blast loading data is presented so that response estimates for specific cases may be calculated using the simple equations given in the report.

It should be obvious that if more precise structural response data are required then additional effort must be expended to improve the analysis methods. Both the blast load determination and the response calculations can be improved. Concerning the first, the inconsistencies in impulse loading arising from the assumption of a one to one correspondence between reflected pressure and impulse should be eliminated. The structural response analysis for flat walls and plates can be improved by considering not only perfectly plastic bending and hinge formation but also the membrane and strain rate effects. An analysis which takes into account wall curvature would further improve the response predictions. An area that merits particular attention is the response of piping under blast loading. Neglecting the interaction between bending and local ring deformation makes

the validity of the results in certain cases very questionable. An analysis procedure which takes into account the coupling between these deformation modes should therefore be developed.

A significant limitation on the applicability of the analysis procedures is the lack of appropriate failure and damage criteria. Some attempts were made to establish approximate relationships between the computed deformations and allowable (rupture) strains. However, much more effort is required to determine the damage levels which are unacceptable for a particular structure. In establishing such limits both the local structural deformations and the functional aspects of the structure should be considered.

Finally it is again pointed out that only air blast loading from explosive detonation was taken into account in the current study. For large charges placed close to the structure ground shock and cratering effects may prove as damaging as the air blast. Regardless of charge weight the contact placement of explosives may produce the severest local damage. Thus in an overall analysis of nuclear power plant vulnerability these loading mechanisms should also be considered.

APPENDIX

Methods for Estimating Pipe Deformation Due to Explosive Loading

The basic problem is to obtain engineering estimates of the total plastic deformation which results when a segment of piping is subjected to explosive loading from a known charge weight located a fixed distance from the pipe. The methods outlined below utilize recent results in dynamic plasticity to obtain such deformation estimates. It should be noted, however, that no entirely satisfactory method is currently available for analysis of this problem. The methods outlined provide only rough approximations in many cases of importance. In particular, when the loading is the result of a nearby charge, many of the assumptions used in this analysis are open to question. Further, since no controlled experiments on explosive loading of piping are available, validation of this analysis is not currently possible.

It is assumed that the total transverse impulse, I_T, is known and that this is a pure impulse. That is, it produces instantaneous velocities proportional to the local impulse (per unit length or per unit area, depending on the formulation). The analysis is further simplified by splitting the impulsive loading into two parts, "symmetric" and "antisymmetric" as shown in Fig. A1. The symmetric impulsive loading causes no translation of the transverse diameter pp' of the cylinder, hence it produces shape changes of the type sketched in Fig. A2(a). The antisymmetric loading produces a rigid-body translation of each ring section, together with some deformations out of the initial circular shape. If the latter deformations are neglected, the antisymmetric impulsive loading produces mainly bending of the pipe as a beam constrained

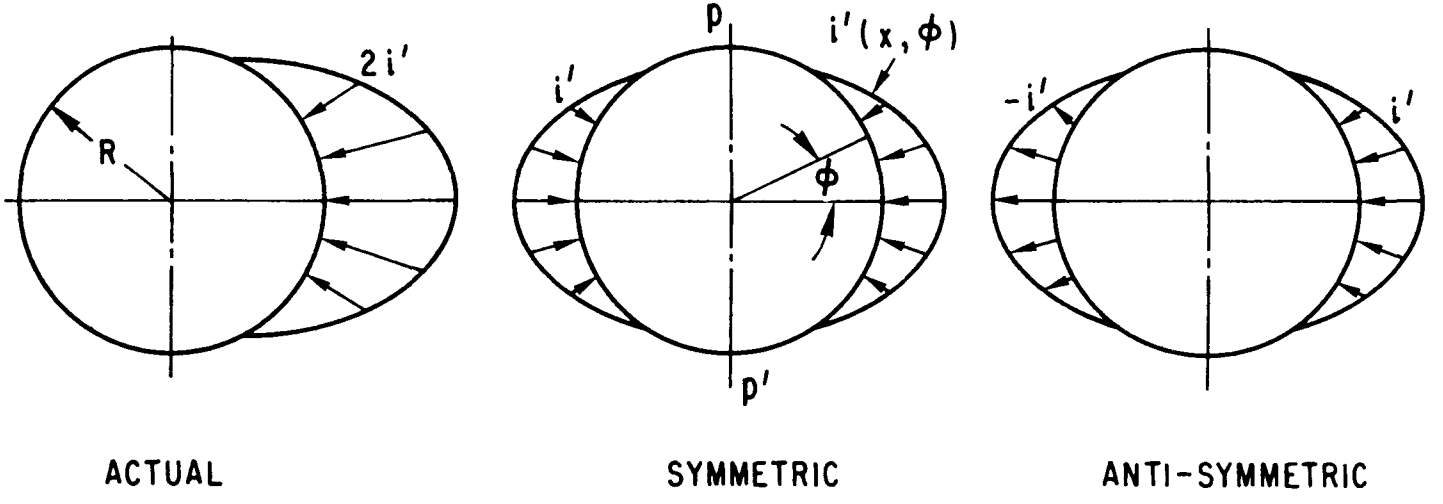

Fig. A1. Splitting of Impulsive Pipe Loading

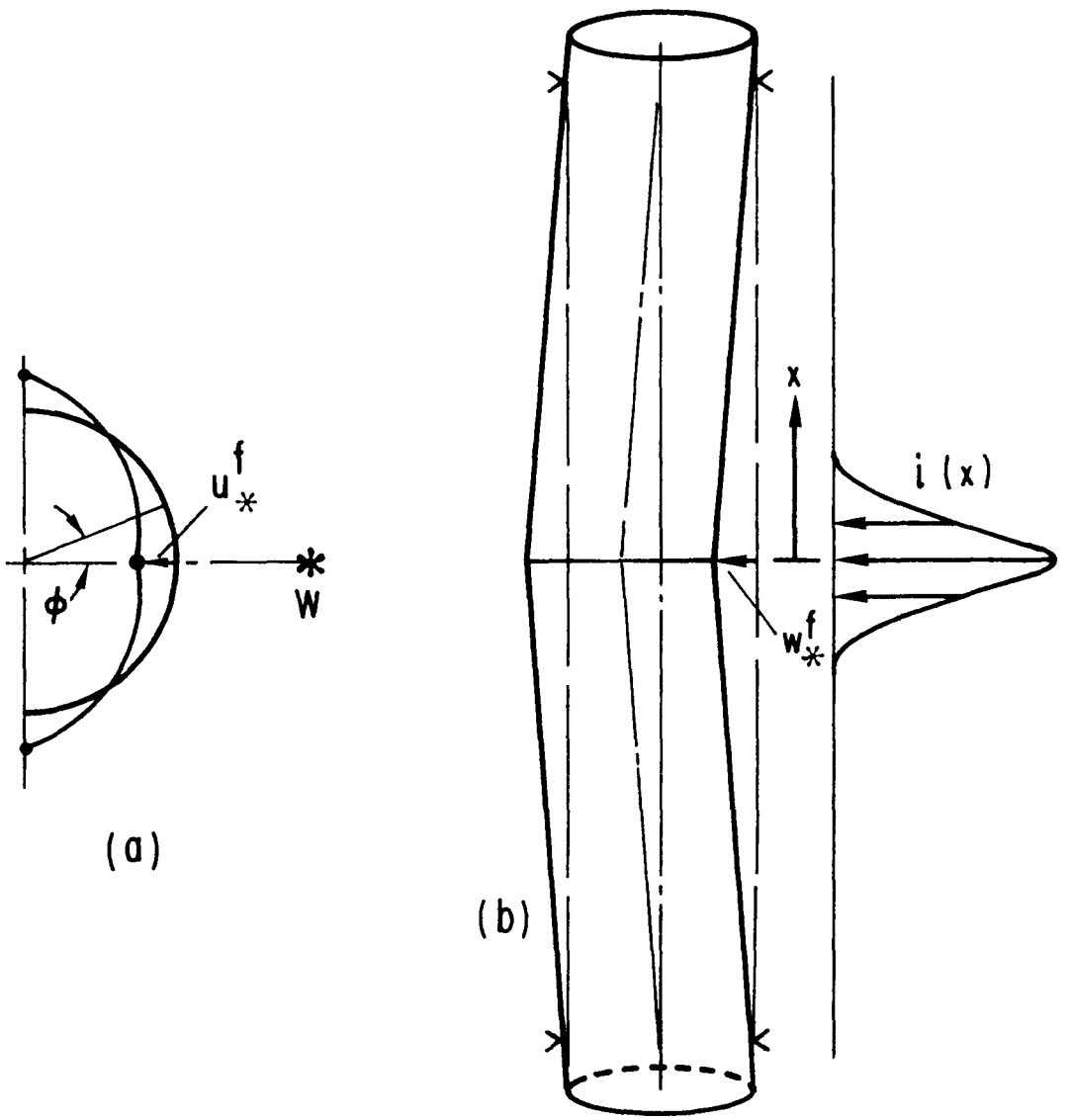

Fig. A2. Local Ring Deformation and Bending Deflection of Pipe

at its supports, as in Fig. A2(b).

A method of damage calculation that is crude, but should be adequate in certain circumstances, is to treat the two loadings and responses as independent of each other, and to obtain the total displacement of the point of the cylinder nearest the charge point W as the sum of the "ring deformation" due to the symmetric loading and the "beam bending" deformation due to deflection of the pipe as a beam between supported sections. The interactions being neglected are (1) the effect of the compressive beam-bending stresses in augmenting the local ring deformations in the area closest to the charge location; and (2) the effect of the inward deflection of the ring in decreasing the effective plastic section modulus. These interactions would be important in a thin-walled cylinder.

The first type of interaction is compensated for qualitatively by treating the deformation of the central ring section as independent of those of the adjacent ring sections. These deform less and hence constrain the deformations of the section closest to the charge point. In the "isolated ring" calculation these constraints are neglected. In the region of maximum deformation this can be regarded as roughly equivalent to the weakening effect of the compressive stresses involved in the bending of the cylinder as a beam. It should also be noted that this discussion presupposes that the two types of deformation - local damage at the central ring section and bending as a beam between supports - are of approximately equal importance. This may not be the case when the impulse distribution is localized near the center of the pipe span or when the charge is very near the pipe.

The known transverse impulse I_T produces instantaneous velocities proportional to impulse per unit distance along the pipe axis in the treat-

ment as a "beam", and per unit area in the treatment as a "ring". This isn't entirely satisfactory since I_T depends on the dimensions of the pipe (radius R, length 2ℓ between supports) as well as on the stand-off distance; however, without more detailed information on actual impulse distributions as a function of dimensions and charge weight, no more exact treatment can be justified.

The mode and the bound approximation methods are employed to estimate deflections and response times. In both cases these have been used in their simplest forms - first for the pipe treated as an ordinary beam, hinged at the supports and at midsection, and then treated as a ring deforming as shown in Fig. A2(a).

The distribution of total impulse is needed in order to apply the mode technique, while the total initial kinetic energy is needed to calculate the deflection bound. Lacking better information, a simple sine distribution of transverse impulse per unit length $i_T(x)$ along the beam axis is assumed:

$$i_T(x) = i_m \sin \frac{\pi}{2} \frac{x}{\ell} . \tag{A1}$$

Since $$I_T = 2 \int_0^{\ell} i_m \sin \frac{\pi}{2} \frac{x}{\ell} \, dx = \frac{4\ell}{\pi} i_m ,$$

$$i_m = \frac{\pi}{4} \frac{I_T}{\ell} . \tag{A2}$$

This gives initial transverse velocities at the beam axis of

$$\dot{w}^o(x) = \frac{i_T}{\bar{\rho}} = \dot{w}_o \sin \frac{\pi}{2} \frac{x}{\ell} ; \quad \dot{w}_o = \frac{\pi}{4} \frac{I_T}{\ell \bar{\rho}} \tag{A3}$$

where $\bar{\rho}$ is mass per unit length, including steel pipe and water, with mass densities ρ_s and ρ_w, respectively:

$$\bar{\rho} = A_s\rho_s + A_w\rho_w = \pi(R_o^2 - R_i^2)\ \rho_s + \pi\ R_i^2\ \rho_w \tag{A4}$$

The total initial kinetic energy K_o of transverse motion then can be estimated as

$$K_o = 2\int_o^{\ell} \frac{1}{2}\ \bar{\rho}\ (\dot{w}^o(x))^2\ dx = \frac{\pi^2}{32}\ \frac{I_T^2}{\ell\bar{\rho}} \tag{A5}$$

1. "Beam" Deflections: The pipe is treated as an ordinary beam and estimates must be developed for maximum central deflection.

a. Mode Approximation

With the initial transverse velocity of the beam axis given by (A5), the mode velocity field is:

$$\dot{w}^*(x,t) = \dot{w}_*\ (t)\ \frac{x}{\ell},\ 0 \le x \le \ell. \tag{A6}$$

The initial velocity magnitude, $\dot{w}_*^o$, is obtained by the mode matching technique as

$$\dot{w}_*^o = \frac{\int_o^{\ell} \dot{w}^o(x)\ \frac{x}{\ell}\ dx}{\int_o^{\ell} (\frac{x}{\ell})^2\ dx} = \frac{3}{\pi}\ \frac{I_T}{\ell\bar{\rho}}\ . \tag{A7}$$

The acceleration $\ddot{w}_*$ is obtained from the energy-dissipation rate equation

$$-2 \int_o^{\ell} \bar{\rho} (\ddot{w}_* \frac{x}{\ell}) (\dot{w}_* \frac{x}{\ell}) \, dx = 4M_o \frac{\dot{w}_*}{\ell} , \tag{A8}$$

and hence,

$$\ddot{w}_* = - \frac{6M_o}{\ell^2 \bar{\rho}} , \tag{A9}$$

where M_o is the fully plastic moment of the pipe section

$$M_o = 2 \left(\frac{\pi R_o^2}{2} \frac{4R_o}{3\pi} - \frac{\pi R_i^2}{2} \frac{4R_i}{3\pi} \right) \sigma_y = \frac{4}{3} (R_o^3 - R_i^3) \sigma_y . \tag{A10}$$

Integrating (A9) yields

$$\dot{w}_* = \dot{w}_*^o - \frac{6M_o}{\ell^2 \bar{\rho}} t \tag{A11}$$

The final midpoint displacement, w_*^f , and stopping time, t_f, are

$$w_*^f = \frac{\ell^2 \bar{\rho}}{12 M_o} (\dot{w}_*^o)^2 = \frac{3}{4\pi^2} \frac{I_T^2}{M_o \bar{\rho}} , \tag{A12a}$$

$$t_f = \frac{\ell^2 \bar{\rho}}{6M_o} \dot{w}_*^o = \frac{1}{2\pi} \frac{\ell I_T}{M_o} . \tag{A12b}$$

b. Upper Bound Estimate

An upper bound on the midpoint deflection is given by

$$w_m^f \leq w_m^{fu} = \frac{K_o}{P_L} \tag{A13}$$

where K_o is the kinetic energy due to the impulse and P_L is the limit load magnitude of a force applied at the midsection. Assuming small deflections this is

$$P_L = \frac{4M_o}{\ell} \tag{A14}$$

Taking K_o from Eq. (A5),

$$w_m^{fu} = \frac{\pi^2}{32} \frac{I_T^2}{\ell\bar{\rho}} \frac{\ell}{4M_o} = \frac{\pi^2}{128} \frac{I_T^2}{M_o\bar{\rho}} \tag{A15}$$

A comparison of (A15) with (A12a) shows that the two estimates are quite close. The upper bound is probably quite close to the mode technique since the latter is itself an overestimate when compared to a complete rigid-plastic solution. The overstimate compared to such a solution is probably about 15%. Strain rate sensitivity could reduce the deflection by as much as 50% in the case of a mild steel.

The defect of taking the load magnitude as specified by the total impulse I_T is indicated by the form of the expressions for final deflection. Both methods give this as proportional to $I_T^2/M_o\bar{\rho}$, with no dependence on ℓ. The result would be more useful if the dependence on pipe dimensions, explosive charge weight, and stand-off could be shown explicitly.

2. "Ring" Deflection Estimate:

To estimate deformations of the central ring section from its initial circular shape, there is need for a distribution of impulse per unit area around the circumference. For lack of better information, the radial impulse is taken as a cosine function of central angle

$$i'(\phi) = i_o' \cos\phi. \tag{A16}$$

At the midsection of the span the impulse per unit length is i_m, so

$$i_m = 2\int_0^{\pi/2} i' \cos\phi \; Rd\phi = 2i_o'\int_0^{\pi/2} \cos^2\phi \; Rd\phi = \frac{\pi}{2} Ri_o' \tag{A17}$$

where R is the mean radius. Thus

$$i_o' = \frac{2}{\pi R}\,\frac{\pi}{4}\,\frac{I_T}{\ell} = \frac{I_T}{2R\ell}. \tag{A18}$$

The total impulsive loading on the middle ring section can be split into "anti-symmetric" and "symmetric" parts as in Fig. A1, each with half the intensity magnitude of the supposed distribution $i'(\phi)$. Intuitively, the antisymmetric loading produces mainly translation of the section without large changes of the circular shape, while the symmetric loading produces the shape changes of the ring we are interested in, the transverse diameter remaining stationary. This is not rigorous since no superposition principle can be claimed; however, it seems to be a reasonable assumption if the impulse isn't too localized.

The initial velocity field due to the impulse can be expressed in terms of components $\dot{u}_1^o$, $\dot{u}_2^o$ shown in Fig. A3(a). The equations relating these velocity components to the total impulse are:

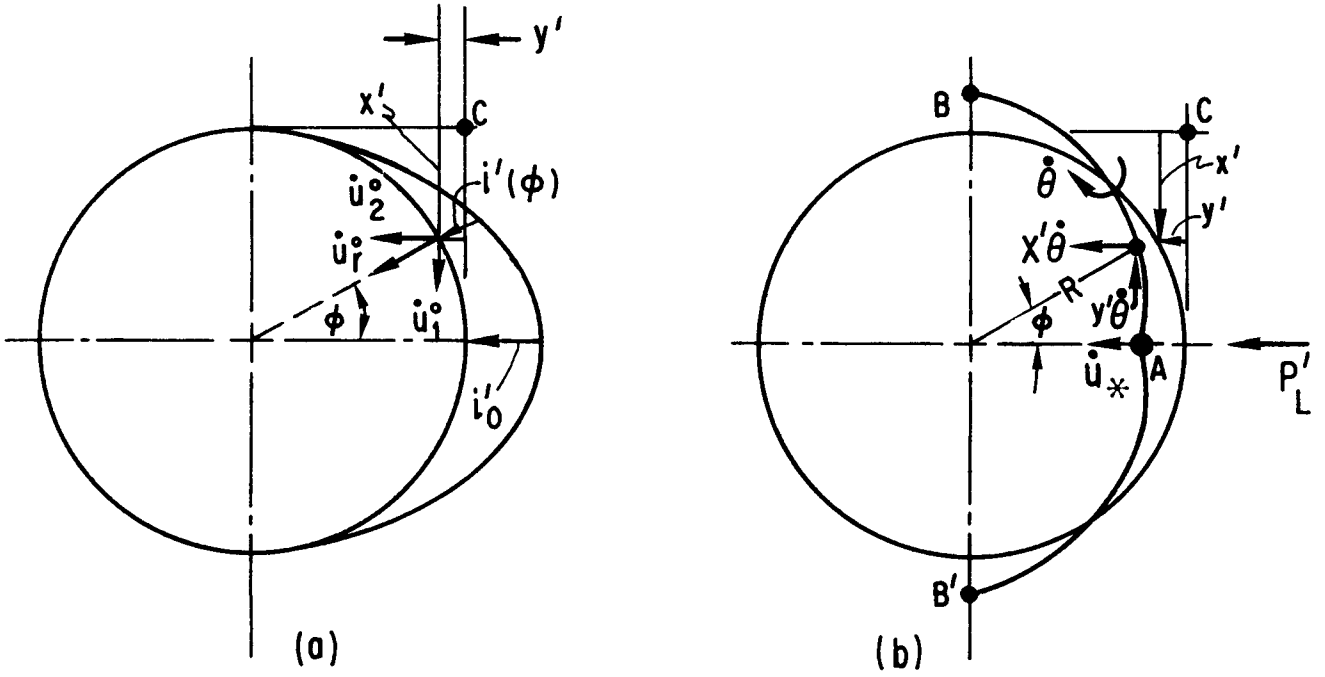

Fig. A3. Velocity Components of Local Ring Deformation

$$\dot{u}_1^o = \dot{u}_r \sin\phi = \frac{i'(\phi)}{\rho'} \sin\phi = \dot{u}_o \cos\phi \sin\phi \tag{A19a}$$

$$\dot{u}_2^o = \dot{u}_r \cos\phi = \frac{i'(\phi)}{\rho'} \cos\phi = \dot{u}_o \cos^2\phi \tag{A19b}$$

where $$\dot{u}_o = \frac{i'_o}{\rho'} = \frac{i'_o}{\rho_s h} = \frac{I_T}{2\rho_s hR\ell} \tag{A20}$$

where $\rho' = \rho_s h$ is the mass density per unit area of the pipe wall, thickness h.

a. Mode Approximation

The mode form deformation is taken to be symmetric in each half of the ring, as shown in Fig. A3(b). This has plastic hinges at A, B, B', with rigid-body rotation rate $\dot{\theta}$ about the instantaneous center at C. Thus the velocity field has components

$$\dot{u}_1^* = -y'\dot{\theta} = \dot{u}_* (-\frac{y'}{R}) = \dot{u}_* (-1 + \cos\phi) \tag{A21a}$$

$$\dot{u}_2^* = x'\dot{\theta} = \dot{u}_* \frac{x'}{R} = \dot{u}_* (1 - \sin\phi) \tag{A21b}$$

Here $\dot{u}_*(t)$ is the mode form velocity amplitude, whose initial value $\dot{u}_*^o$ is found by the standard technique from the assumed initial field, as

$$\dot{u}_*^o = \dot{u}_o \frac{\pi/4 - 1/2}{3\pi/2 - 4} \simeq 0.201 \frac{I_T}{\rho_s hR\ell} . \tag{A22}$$

The acceleration magnitude $\ddot{u}_*$ of the mode deformation is obtained from the energy rate equation

$$-2 \int_o^{\pi/2} \rho' (\ddot{u}_1^* \dot{u}_1^* + \ddot{u}_2^* \dot{u}_2^*) \, Rd\phi = 4M'_o \frac{\dot{u}_*}{R} \tag{A23}$$

where $\rho' = \rho h$ is mass per unit area of wall and M_o' is fully plastic bending moment per unit length along the pipe axis,

$$M_o' = \frac{h^2}{4}\sigma_y \ . \tag{A24}$$

Using eqs. (A21) we obtain

$$\ddot{u}_* = -\frac{h\sigma_y}{(3\pi-8)R^2\rho_s} \simeq -\frac{h\sigma_y}{1.425R^2\rho_s} \ . \tag{A25}$$

Integrating gives the following results for the final deformation and stopping time:

$$u_*^f = 0.0286\,\frac{I_T^2}{\sigma_y\rho_s h^3\ell^2} \ , \tag{A26a}$$

$$t_f = 0.285\,\frac{RI_T}{\sigma_y h^2\ell} \ . \tag{A26b}$$

The intuitive argument illustrated in Fig. A1 suggests that the deformation out of the circular shape is due to the symmetric loading with amplitude $\frac{1}{2}i'$. This corresponds to replacing I_T by $\frac{1}{2}I_T$ in Eqs. (A26).

b. Upper Bound Estimate

Alternatively the deflection bound method can be applied. This requires the initial kinetic energy K_o' per unit length at the span mid-section and the plastic collapse load P_L' of the half ring subjected to a pair of forces at the middle diameter of the ring. These are

$$K_o' = \frac{\pi}{4}\rho' R\dot{u}_o^2 = \frac{\pi}{4}\rho_s hR\left(\frac{I_T}{2\rho_s hR\ell}\right)^2 \tag{A27}$$

$$P'_L = \frac{4M'_o}{R} = \frac{h^2\sigma_y}{R} \tag{A28}$$

The upper bound is given by

$$u_o^f \leq u_o^{fu} = \frac{K'_o}{P'_L} = \frac{\pi}{16}\,\frac{I_T^2}{\sigma_y \rho_s h^3 \ell^2} \tag{A29}$$

where again one replaces I_T with $\frac{1}{2}I_T$ to account for only the symmetric impulsive loading producing ring deformation.

The upper bound is much larger than the final displacement predicted by the mode method. This may be traced to the small value, 0.401, of the ratio $\dot{u}_*^o/\dot{u}_o$, which implies that the mode method underestimates the final deflection. In the bound method, the distribution of kinetic energy is never specified. Thus the bound must allow for cases where the maximum deflection is sensitive to the distribution of kinetic energy.

The deformation estimates developed above may be summarized as follows:

Beam:

$$w_*^f = \frac{3}{4\pi^2}\,\frac{I_T^2}{M_o \bar{\rho}} \quad \text{, (mode)} \tag{A12a}$$

$$w_m^{fu} = \frac{\pi^2}{128}\,\frac{I_T^2}{M_o \bar{\rho}} \quad \text{, (bound)} \tag{A15}$$

Ring:

$$u_*^f = 0.0286\,\frac{I_T^2}{\sigma_y \rho_s h^3 \ell^2} \quad \text{, (mode)} \tag{A26a}$$

$$u_o^{fu} = \frac{\pi}{16}\,\frac{I_T^2}{\sigma_y \rho_s h^3 \ell^2} \quad \text{, (bound)} \tag{A29}$$

In summary, the two deflection estimates, (a) treating the structure as a beam, and (b) treating the mid-section as an isolated ring, are here

assumed independent of each other, based on a conjectural splitting of the impulsive load into an anti-symmetric and a symmetric part, with the former causing mainly translational motion of the whole ring, and the latter producing deformations of the initial circular shape. The two types of response are obviously not independent; energy used in local deformation is not available for producing translational (beam type) deformations. A mode approximation could be developed which couples the bending and ring deformations; however, such a development effort is not consistant with the overall objectives of the current study.

The deformation estimates contained in the body of this report are based on eqs. (A12a), (A15), (A26a), (A29) above - suitably modified to include charge weight and standoff distance by proper substitution for I_T.

3. Sample Calculations

To compare the various deformation estimates, the following sample problem is considered:

$$I_T = 14.72 \times 10^3 \text{ lb-sec}$$

$$\ell = 120 \text{ inches}$$

$$R_i = 10 \text{ in.}, \; R_o = 12 \text{ in.}, \; h = 2 \text{ in.}$$

$$\sigma_y = 40 \times 10^3 \text{ psi}$$

$$\rho_s = 0.73 \times 10^{-3} \text{ lb. in.}^{-4} \text{ sec}^2$$

$$\rho_w = 0.094 \times 10^{-3} \text{ lb. in.}^{-4} \text{ sec}^2$$

$$M_o = 38.8 \times 10^6 \text{ in. lb.}$$

$$\bar{p} = 0.131 \text{ lb. in.}^{-2} \text{ sec}^2$$

This corresponds approximately to a 20 ft. span of 2 ft. outside dia., sch 140,

water-filled pipe subjected to a 1000 lb. charge detonated 10 ft. from the pipe center. The various estimates are as follows:

Beam: $w_*^f = 3.24$ in. (mode)

$w_m^{fu} = 3.29$ in. (bound)

Ring: $u_*^f = 0.46$ in. (mode)

$u_o^{fu} = 3.16$ in. (bound)

For this particular case, the beam response would appear to dominate (using the mode approximation) and the predicted deformation are small enough that the small strain response limitation of the theory is probably a good approximation. The previously mentioned differences in the ring approximations can also be seen.

4. Possible Modification due to Impulse Distribution

All of the above computations were based on simple sine and cosine distributions of impulse. Clearly the distribution of impulse can deviate from such distributions by wide margins - particularly in the case of close-in detonations. To illustrate this point consider a larger diameter pipe subjected to a close-in detonation. Using a pipe of 24 in. radius, 2 in. wall thickness and a stand-off distance of 2 ft. produces a more concentrated impulse pressure. Local damage becomes more pronounced than beam bending deformation and calculations based on an isolated ring appear unsatisfactory - probably leading to gross overestimation of local deformation.

To illustrate this, consider the following impulsive loading distribution:

		$x =$	0	1	2	4	10 ft
Case 1:	2 ft stand-off	$i'(x,0) =$	33	24	10.2	3.0	1.0 psi-sec

$I_T = 14.7 \times 10^3$ lb-sec

Case 2: 10 ft stand-off

	x =	0	5	10	15	ft
$I_T = 6.7 \times 10^3$ lb-sec	$i'(x,0)$ =	3.5	3.0	1.5	0.8	psi-sec

where $i'(x,\theta)$ is the impulsive pressure (psi-sec) at a point x from the central section and at angle θ from the "horizontal" diameter. The ring deformations are predicted to be:

Case 1: 2 ft stand-off

$$\dot{u}_*^o = \frac{13.7}{2\rho_s h} = 4690 \text{ in.-sec}^{-1}$$

$$u_*^f = 3.74 \times 10^{-6} (\dot{u}_*^o)^2 = 82.4 \text{ in.}$$

Case 2: 10 ft stand-off

$$\dot{u}_*^o = \frac{1.53}{2\rho_s h} = 524 \text{ in.-sec}^{-1}$$

$$u_*^f = 3.74 \times 10^{-6} (\dot{u}_*^o)^2 = 1.03 \text{ in.}$$

The very large value of displacement in Case 1 (2 ft stand-off) is meaningless quantitatively, since the analysis is valid for small deflections. Qualitatively it indicates only that in this mode of deformation the local (out-of-circular) displacement is of the order of the pipe radius, and would probably lead to failure by rupture.

A similar calculation can be performed for the beam mode. To account for the localized nature of the impulse, a bell shaped distribution of impulse is used. Tabulated impulse per unit area data at x = 0 is computed to give i_m where

$$i_m = 2 \int_o^{\pi/2} i_o' (0,\theta) \cos\theta \, R d\theta$$

and the axial distribution is assumed to be

$$i(x) = i_m \exp (-x^2/2\sigma^2).$$

Knowing the total impulse

$$I_T = \int_{-\infty}^{\infty} i_m \exp (-x^2/2\sigma^2) \, dx = \sqrt{2\pi} \; \sigma \, i_m$$

allows computation of the parameter σ as

$$\sigma = \frac{1}{\sqrt{2\pi}} \frac{I_T}{i_m} .$$

Applying the mode technique gives the following results:

Case 1 (2 ft stand-off):

$$i_m = 806 \text{ lb-sec-in}^{-1}$$

$$I_T = 14.7 \times 10^3 \text{ lb-sec}$$

$$\sigma = 7.3 \text{ in.}$$

$$\dot{w}_*^o = 493 \text{ in-sec}^{-1}$$

$$w_*^f = 0.61 \text{ in.}$$

Case 2 (10 ft stand-off):

$$i_m = 118 \text{ lb sec in}^{-1}$$

$$I_T = 6.7 \text{ lb-sec}$$

$$\sigma = 22.7 \text{ in.}$$

$$\dot{w}_*^o = 201 \text{ in-sec}^{-1}$$

$$w_*^f = 0.10 \text{ in}$$

Evidently for these examples the local (out-of-circular) deformation of the central ring section greatly exceeds that of the beam bending mode. The present estimated deflections are smaller than those of the previous section in part because of the change of dimensions of the pipe (R = 24 in. instead of R = 11 in.) and because of the change of the initial mode amplitude; the latter is due both to the change of dimensions and to the use of more detailed data on impulse distribution.

Clearly, to obtain definitive estimates of final plastic deformation requires development of more exact impulse data and development of refined analysis methods.

REFERENCES

1. Glasstone, S. (editor), The Effects of Nuclear Weapons, U.S. Government Printing Office, Washington, D.C., 1962.
2. Department of the Army, "Structures to Resist the Effects of Accidental Explosions," TM5-1300, U.S. Government Printing Office, Washington, D. C., June 1969.
3. National Defense Research Committee, "Effects of Impact and Explosions," Summary Technical Report, Vol. 1, AD221586, Washington, D.C., 1946.
4. Department of the Army, "Fundamentals of Protective Design (Non-Nuclear)," TM5-855-1, Washington, D.C., July 1965.
5. Kot, C. A. and Turula, P., "Air Blast Effects on Concrete Walls," ANL-CT-76-50, July 1976.
6. Carpenter, H. J. and Brode, H. L., "Height of Burst Blast at High Overpressure," R&D Associates, Santa Monica, California, 1975.
7. Brode, H. L., "A Review of Nuclear Explosion Phenomena Pertinent to Protective Construction," R-425-PR, The Rand Corp., Santa Monica, California, May 1964.
8. Brode, H. L., "A Calculation of the Blast Wave from a Spherical Charge of TNT," RM-1965, The Rand Corp., Santa Monica, California, August 1957.
9. Fergusen, P. M., Reinforced Concrete Fundamentals, 2nd Edition, John Wiley and Sons, Inc., New York 1965.
10. Oscarson, Y. H. and Graff, K. F., "Spall Fracture and Dynamic Response of Materials," Battelle Memorial Institute, Report No. BAT-197A-4-3, Columbus, Ohio, March 1968.
11. Rolsten, R. F., "A Study of the Shock Loading of Materials," Transactions of the New York Academy of Sciences, Series II, Volume 36, No. 5, pp. 416-480, May 1974.

12. Rinehart, J. S., "On Fractures Caused by Explosions and Impacts," Quarterly of the Colorado School of Mines, Vol. 55, No. 4, October 1960.

13. Kolsky, H., Stress Waves in Solids, Dover Publications, New York, 1963.

14. Gupta, Y. M. and Seaman, L., "Local Response of Reinforced Concrete to Missile Impacts," 4th International Conference on Structural Mechanics in Reactor Technology, Paper J 10/4, San Francisco, California, August 15-19, 1977.

15. Backman, M. E. and Goldsmith, W., "The Mechanics of Penetration of Projectiles into Targets," International Journal of Engineering Science, Vol. 16, pp. 1-99, 1978.

16. Healey, J. et. al., "Primary Fragment Characteristics and Impact Effects on Protective Barriers," Technical Report, Picatinney Arsenal, Dover, New York, December 1975.

17. Wierzbicki, T. and Florence, A. L., "A Theoretical and Experimental Investigation of Impulsively Loaded Clamped Circular Viscoplastic Plates," International Journal of Solids and Structures, Vol. 6, pp. 553-568, 1970.

18. Jones, N., "Impulsive Loading of Simple Supported Circular Rigid-Plastic Plate," ASME Transactions, Journal of Applied Mechanics, Vol. 35, pp. 59-65, March 1968.

19. Chou, Ch. T. and Symonds, P. S., "Large Dynamic Plastic Deflection of Plates by Mode Method," Journal of the Engineering Mechanics Division, ASCE, Vol. 103, No. EM1, pp. 169-187, February 1977.

20. Krajcinovic, D., "Dynamic Response of Infinitely Extended Plastic Plates," ASME Transactions, Journal of Applied Mechanics, Vol. 44, pp. 175-177, March 1977.

21. Cole, R. H., Underwater Explosions, Princeton University Press, Princeton, New Jersey, 1948.